Summer 7-2011

Computational Microstructure Modeling of Asphalt Mixtures Subjected to Rate-Dependent Fracture

Francisco Aragao
University of Nebraska-Lincoln, fthiago@huskers.unl.edu

COMPUTATIONAL MICROSTRUCTURE MODELING OF ASPHALT MIXTURES SUBJECTED TO RATE-DEPENDENT FRACTURE

By

Francisco Thiago Sacramento Aragão

A DISSERTATION

Presented to the Faculty of

The Graduate College at the University of Nebraska

In Partial Fulfillment of Requirements

For the Degree of Doctor of Philosophy

Major: Engineering

(Civil Engineering)

Under the Supervision of Professor Yong-Rak Kim

Lincoln, Nebraska

June, 2011

COMPUTATIONAL MICROSTRUCTURE MODELING OF ASPHALT MIXTURES SUBJECTED TO RATE-DEPENDENT FRACTURE

Francisco Thiago Sacramento Aragão, Ph.D.

University of Nebraska, 2011

Adviser: Yong-Rak Kim

Computational microstructure models have been actively pursued by the pavement mechanics community as a promising and advantageous alternative to limited analytical and semi-empirical modeling approaches. The primary goal of this research is to develop a computational microstructure modeling framework that will eventually allow researchers and practitioners of the pavement mechanics community to evaluate the effects of constituents and mix design characteristics (some of the key factors directly affecting the quality of the pavement structures) on the mechanical responses of asphalt mixtures. To that end, the mixtures are modeled as heterogeneous materials with inelastic mechanical behavior. To account for the complex geometric characteristics of the heterogeneous mixtures, an image treatment process is used to generate finite element meshes that closely reproduce the geometric characteristics of aggregate particles (size, shape, and volume fraction) that are distributed within a fine aggregate asphaltic matrix (FAM). These two mixture components, *i.e.*, aggregate particles and FAM, are modeled, respectively, as isotropic linear elastic and isotropic linear viscoelastic materials and the material properties required as inputs for the computational model are obtained from simple and expedited laboratory tests.

In addition to the consideration of the complex geometric characteristics and inelastic behavior of the mixtures, this study uses the cohesive zone model to simulate fracture as a

gradual and rate-dependent phenomenon in which the initiation and propagation of discrete cracks take place in different locations of the mixture microstructure. Rate-dependent cohesive zone fracture properties are obtained using a procedure that combines laboratory tests of semi-circular bending specimens of the FAM and their numerical simulations. To address the rate-dependent fracture characteristics of the FAM phase, a rate-dependent cohesive zone model is developed and incorporated into the mainframe of ABAQUS in the form of a customized user element (UEL) subroutine. The applicability of the rate-dependent microstructure fracture model is demonstrated and a parametric analysis is performed to evaluate the effects of different mixture parameters on the mechanical behavior of virtually generated hot-mix asphalt (HMA) microstructures. The results presented in this research demonstrate that computational microstructure models, such as the one developed in this study, have a great potential to become efficient design tools for asphalt mixtures and pavement structures.

For the glory of Jesus Christ

DEDICATION

I dedicate this dissertation to the lord of my life, Jesus Christ, to my life partner and beloved wife, Gabriella Moreira, to my beautiful and beloved daughter, Giovanna Aragão, to my beloved mother, friend, and example to be followed here on Earth, Fátima Sacramento, to my beloved father, Demountiez Aragão, to my awesome brother and great beloved friend, Thiciano Aragão, and to my biggest fan and beloved grandmother, Francisca Pernambuco, for their love during easy and hard times and for always believing that I would be able to finish this arduous and challenging Ph.D. program.

ACKNOWLEDGMENTS

My first and most special thanks are dedicated to my source of strength and example to be followed, my lord Jesus Christ. Thanks are to Thee for truly being with me every time life and its circumstances tried to push me down.

I would like to express a deep gratitude to my extraordinary adviser, Dr. Yong-Rak Kim, for all his support, encouragement, trust, and investment in my career. I would never be able to publish the number of papers I had the opportunity to publish and give presentations in important scientific meetings without Dr. Kim's advice, guidance, and investment in my career. If I could go back in time and have the opportunity to choose an adviser for my graduate studies, I would without any doubt choose Dr. Kim again. I also want to publicly thank him for caring about my family and for being there for me during the hardest time of my life a few months ago. I owe him more than I will ever be able to pay and hope we can continue our research partnership for long years.

I thank Dr. Jorge Barbosa Soares for opening the doors of the fascinating world of pavement research to me and for always being part of my education. He is definitely one of the icons of my academic life. I also thank our former dean, Dr. David H. Allen, for giving me the opportunity to come abroad to complete my graduate studies.

I thank Dr. Libby Jones for everything she did for me during my life in Nebraska as a graduate student and for her friendship. My family and I greatly enjoyed the moments we had with her. I also thank Dr. Mehrdad Negahban and Dr. Raymond Moore for supervising my doctoral research work and for kindly providing me with important and valuable suggestions for the improvement of this work.

I thank my co-workers, Dr. Junghun Lee, Dr. Hoki Ban, Dr. Roberto Soares, Dr. Flávio Souza, Mrs. Jamilla Lutif, Mr. Pravat Karki, Mr. Soohyok Im, Mr. Mohammad Javaherian, Mr. Jun Zhang, Mr. Leonardo de Souza, Mrs. Ingryd Pinto, Mr. Minki Hong, Mrs. Emmeline Watson, and Mr. Ian Plummer for their support and productive conversations about our research topics. Special thanks go to my dear friend, Dr. Roberto Soares, for his friendship and support since I arrived in Nebraska and to my friends Pravat and Mohammad, who devoted a lot of their time to provide me with important material used in this dissertation. I also thank my friend Matt Kohrell for kindly revising this dissertation and for providing suggestions to improve the text.

Thanks are also due to the staff of the College of Engineering, of the Civil Engineering department and of the Nebraska Transportation Center (NTC). Special thanks go to Mr. James Nau, Mrs. Rebecca Barnes, Mrs. Jennifer Dush, Mrs. Pam Wiese, Mrs. Charise Alexander, and Mrs. April Didier for always being ready to assist me with smiles in their faces. Special thanks also go to NTC's director and coordinator, Dr. Larry Rilett and Mrs. Valerie Lefler, respectively, for all the doors they kindly opened for my family and I during my studies.

I also acknowledge the importance of the partnership and instructions received from the amazing staff of the Nebraska Department of Roads. Special thanks go to Mr. Larry Koves, Mr. Dale Byre, and Mr. James Beason.

Finally, I express my sincere gratitude to my family, especially my wife, mother, father, brother, grandmother, parents-, brother-, and sister-in-law for always believing that I would be able to finish this work. Your love and support were tremendously important to give me strength to conclude this dissertation.

FINANCIAL SUPPORT

I am deeply thankful for the financial support received from the Federal Highway Admnistration/ Western Research Institute/ Texas A&M Research Foundation.

Contents

List of Figures

List of Tables

Chapter 1

Introduction

Asphalt concrete mixtures are particulate composite materials comprising randomly-oriented and distributed aggregates, asphalt binder, mineral fillers, air voids, and additives. They are commonly used materials in the construction of roadways, airports, and parking lots with the main objective to sustain the loads applied by moving or stationary vehicles.

As for any other composite, the characteristics of each individual constituent of the asphalt mixtures directly affect the overall behavior of the mixtures. This is actually the main benefit offered by engineered composite materials, *i.e.*, they can be better designed via the optimization of the properties of each constituent. In the case of asphalt materials, two main components play a major role in the definition of the characteristics of the composite - the mineral aggregate particles and the cementitious phase of asphalt cement, fine aggregates, and air voids.

The unique and complex characteristics of the cementitious asphaltic phase appear to be of major importance because they introduce a rate and temperature dependence to the mechanical properties of the whole composite. Thus, the accurate determination of material properties of the cementitious phase is necessary for the proper characterization of the mechanical responses of asphalt concrete mixtures subjected to different loading and environmental conditions. On the other hand, the skeleton of mineral aggregates also greatly influences the properties of the asphaltic composite because of its high volume fraction in the mixtures as well as its elevated stiffness properties.

Several standards have been proposed to obtain material properties of asphalt mixtures from laboratory testing. However, the determination of such properties in a representative and wide range of temperature and loading conditions may become an expensive and time-consuming process that involves the fabrication and testing of multiple replicates in laboratory for days and sometimes weeks. To reduce costs and the time required to obtain material properties of asphalt mixtures, several predictive approaches have been proposed and shown different levels of success. Semi-empirical and analytical models generally present a certain agreement with experimentally-obtained properties, but the complex characteristics of the mixtures greatly limit the predictive efficiency of such methodologies.

To overcome the generic limitations of analytical and semi-empirical approaches, computational microstructure modeling based on well-established numerical methods (*e.g.*, finite and discrete element methods) has been actively pursued as a promising alternative. Among the main advantages of the computational microstructure models over other predictive methodologies, one can mention that the computational approach uses microstructural characterization to account for numerous damage modes separately by considering individual mixture constituents and mixture heterogeneity. Moreover, this approach does not require a large number of expensive and time-consuming laboratory experiments because it typically relies on numerical techniques and merely requires individual mixture constituent properties as model inputs.

Among many challenges that still limit the predictive capabilities of computational models, the understanding of the cracking phenomenon is probably one of the most cumbersome to overcome. This is because of several factors, such as: the heterogeneity and the inelastic constitutive responses of the mixtures; the relatively large deformations in the fracture process

zone of the mixtures; the rate-dependent characteristics of that fracture process zone; the difficulties associated with the proper characterization of rate-dependent fracture properties and with the development of fracture models that consider the rate-dependence of those properties, among others.

The primary goal of this research is to develop a computational microstructure modeling framework that will eventually allow researchers and practitioners of the pavement mechanics community to evaluate the effects of constituents and mix design properties (some of the key factors directly affecting the quality of the pavement structures) on the mechanical responses of asphalt mixtures. To that end, the complex microstuctural characteristics of the mixtures are reproduced in the model, which allows model users to easily evaluate effects of individual constituent properties and volumetric characteristics of the mixtures. Additionally, the model accounts for the rate-dependence of the fracture process zone of the mixtures via the development of a rate-dependent cohesive zone fracture model.

The results shown throughout the dissertation demonstrate that computational microstructure models, such as the one presented herein, can become efficient design and analysis tools for the prediction of damage-dependent behavior of asphaltic composites when geometric characteristics of mixture microstructure and properties of individual mixture constituents are known and properly considered.

1.1 Research Objective

The objective of this research is to develop a computational microstructure modeling framework to predict mechanical properties and performance of heterogeneous and inelastic asphalt

mixtures that exhibit rate-dependent fracture characteristics at intermediate temperature conditions.

Specific objectives of this research are:

- To propose simple experimental testing protocols for the characterization of fracture properties of asphalt mixtures;
- To develop a computational microstructure model for predicting:
    - Undamaged properties of heterogeneous and inelastic HMA mixtures;
    - Fracture-related damage behavior of heterogeneous and inelastic HMA mixtures;
- To improve the accuracy of the model through the incorporation of customized user-subroutines into the mainframe of the commercial finite element (FE) code used in the research (ABAQUS).

1.2 Dissertation Layout

Following this introductory chapter, ***Chapter 2*** presents a comprehensive literature review on several approaches attempting to characterize the mechanical behavior of asphalt mixtures, as well as advantages, limitations, and shortcomings of these approaches. Experimental testing protocols available in the literature to characterize fracture properties of asphalt mixtures are also reviewed. In ***Chapter 3***, a description of the initial boundary value problem (IBVP) for a general elastic-viscoelastic composite containing cracks is presented. Then, a short discussion on the formulation of the intrinsic bilinear cohesive zone model chosen for the fracture simulations in this study is also provided. ***Chapter 4*** first describes the incorporation of a rate-independent CZ model into an ABAQUS user-element (UEL) subroutine. Then, to account for the rate-

dependence of the fracture process zones of the mixtures, a rate-dependent cohesive zone fracture model is presented. ***Chapter 5*** describes the experimental testing program designed in this research to obtain material properties of the different mixture phases. It also shows experimental testing results of dynamic modulus of asphalt mixtures that are used in a later chapter (***Chapter*** 7) for the validation of the computational microstructure model. ***Chapter 6*** presents numerical simulations performed to determine cohesive zone fracture parameters for a wide range of applied loading rates. Extra simulations are also performed to calibrate the rate-dependent functions for cohesive strength and fracture energy. In ***Chapter*** 7, simulations of tests with HMA mixtures are conducted to demonstrate the ability of the computational microstructure model to predict the dynamic modulus and simulate the fracture behavior of the mixtures and to account for the effects of important variables on the mechanical behavior of the mixtures. ***Chapter 8*** presents the conclusions of the research and recommendations for future work required to improve the model predictions.

Chapter 2

Background

The proper understanding of the responses of pavement structures to load and environmental conditions is a fundamental step towards the construction of more comfortable and durable highways, which will eventually lead to savings of the taxpayers' money reserved for the roadway networks around the globe. This understanding is generally facilitated by the development of simple and efficient testing protocols that can reproduce the behavior of the pavement structures in the laboratory. Nowadays, the pavement community is equipped with modern equipment and devices and has the ability to perform tests with a multitude of loading and temperature conditions. Using such powerful equipment, a lot of effort has been devoted for the development of testing procedures and protocols that can provide researchers and practitioners with reliable material properties and that are able to reproduce the damage responses of the pavement structures to applied loads and environmental effects.

Based on properties of individual mixture constituents and volumetric characteristics (mix design) of asphalt mixtures using laboratory-fabricated specimens, several empirically based models have been developed and used in the last decades. A classical example of such models is the predictive model that has been developed by Witczak and his colleagues to estimate the dynamic modulus of asphalt mixtures from mix design inputs and component properties. The first version of Witczak's predictive equation (Andrei *et al*., 1999) that was used in the first development of the Mechanistic-Empirical Pavement Design Guide (MEPDG) considered mixture volumetric properties and gradation, binder viscosity, and loading frequency

as input variables to predict the stiffness of asphalt concrete mixtures. Multivariate regression analysis of 2,750 experimental data was used to construct the 1999 version of the predictive $|E^*|$ expression. In 2006, Bari and Witczak revised the 1999 version, using 7,400 $|E^*|$ values (2,750 from the original version and 4,650 new data points) from 346 mixtures. Another improvement was the use of the dynamic shear modulus and the phase angle of binders as inputs to the model. The 1999 equation used viscosity and loading frequency to characterize the mechanical behavior of the binder phase. The 2006 version of Witczak's predictive equation (Bari and Witczak, 2006) is shown in Equation 1.

$$\log_{10}\left|E^*\right| = -0.349 + 0.754\left|G_b^*\right|^{-0.0052} \cdot \left(\begin{array}{l} 6.65 - 0.032\rho_{200} + 0.0027\rho_{200}^2 + 0.011\rho_4 - 0.0001\rho_4^2 \\ + 0.006\rho_{38} - 0.00014\rho_{38}^2 - 0.08V_a - 1.06\left(\dfrac{V_{beff}}{V_a + V_{beff}}\right) \end{array} \right)$$
$$+ \frac{2.56 + 0.03V_a + 0.71\left(\dfrac{V_{beff}}{V_a + V_{beff}}\right) + 0.012\rho_{38} - 0.0001\rho_{38}^2 - 0.01\rho_{34}}{1 + e^{\left(-0.7814 - 0.5785\log\left|G_b^*\right| + 0.8834\log\delta_b\right)}} \quad (1)$$

where $|E^*|$, $|G_b^*|$, ρ_{200}, ρ_4, ρ_{38}, ρ_{34}, V_a, V_{beff}, and δ_b = dynamic modulus of mixture (psi), dynamic modulus of binder (psi), aggregates passing through No. 200 sieve (%), cumulative aggregates retained on no. 4 sieve (%), cumulative aggregates retained on the 3/8" sieve (%), cumulative aggregates retained on the 3/4" sieve (%), air voids (by volume of the mix) (%), effective binder content (by volume of the mix) (%), and phase angle of binder (degree).

Clearly, the 2006 version of Witczak's predictive equation represents a better prediction than the 1999 version due to more data involved, although it has been reported in the literature

that the model exhibits increased error magnitudes at extremely high- and low-temperature conditions (Bari and Witczak, 2006; Ceylan *et al*., 2009).

Christensen *et al*. (2003) proposed another semi-empirical has been used by many researchers and practitioners. The model is based on the rule of mixtures which results in a simple predictive expression that includes: volumetric parameters such as voids in the mineral aggregate (*VMA*) and voids filled with asphalt (*VFA*), the stiffness of binder ($|G_b^*|$), and the aggregate contact volume (P_c). The authors compared this simplified version of the model with another version that accounted for the stiffening effects of mastic. They concluded that the simplified equation (which treated the asphalt concrete mixtures as a simple three-phase system consisting of aggregate, asphalt binder, and air voids) is accurate in many applications. The final expression for the simplified version of the model is shown in Equations 2 and 3.

$$\left|E^*\right| = P_c\left[4{,}200{,}000\left(1-\frac{VMA}{100}\right)+3\left|G_b^*\right|\left(\frac{VFA\cdot VMA}{10{,}000}\right)\right]+\left(1-P_c\right)\left[\frac{1-\frac{VMA}{100}}{4{,}200{,}000}+\frac{VMA}{3\cdot VFA\cdot\left|G_b^*\right|}\right]^{-1} \tag{2}$$

$$P_c = \frac{\left(20+\frac{VFA\cdot 3\left|G_b^*\right|}{VMA}\right)^{0.58}}{650+\left(\frac{VFA\cdot 3\left|G_b^*\right|}{VMA}\right)^{0.58}} \tag{3}$$

where P_c, VMA, and VFA = aggregate contact volume, voids in mineral aggregates (%), and voids filled with asphalt (%).

Empirical methodologies basically intend to predict the behavior of the heterogeneous structures based on the statistical analysis of databases containing large amounts of data accumulated from expensive and time-consuming experiments. In many cases, the databases are created based on regional materials and weather conditions and this limits the predictive power of such predictive methodologies.

In the attempt to formulate more universal relations between the variables (*i.e.*, individual constituent properties and volumetric/geometric characteristics) and the overall responses of heterogeneous composites to external loads, analytical micromechanics formulations have also been proposed in the open literature. Micromechanics is a theoretical method used to determine the effective properties of mixtures from known properties and phase geometry of the constituents of the mixtures. Constitutive response at the macro-scale level of the mixtures can be calculated in terms of small-scale parameters (*e.g.*, the shape and volume fraction of heterogeneities) and their own constitutive properties. Starting with the fundamental work of Einstein (Einstein, 1906), many different micromechanical analyses have been developed to understand the behavior of heterogeneous mixtures. Among numerous analytical micromechanics models, Hashin (1962) proposed an approximate model for isotropic heterogeneous media containing spherically shaped particles based on the variational theorems of linear elasticity.

Effective elastic material properties can be directly converted to viscoelastic properties using the correspondence principle on the basis of the Laplace transform. Therefore, the elastic solution can be reinterpreted as a viscoelastic solution in the transformed domain by replacing the elastic material properties by the Carson transformed properties. Corresponding time-dependent viscoelastic properties, such as relaxation modulus can be determined by inverse

Laplace transformation simply by using Schapery's direct method (Schapery, 1962). By assuming that the shear modulus of the rigid aggregates and Poisson's ratios of each phase are constants (*i.e.*, not a function of time), the linear viscoelastic shear relaxation modulus of asphalt concrete mixtures can be expressed by using Hashin's analytical micromechanics model as follows:

$$G(t) = \left[\widetilde{G}_m(s) + \frac{15\widetilde{G}_m(s)(1-\nu_m)\left(\frac{G_p}{\widetilde{G}_m(s)} - 1\right)V_p}{7 - 5\nu_m + 2(4-5\nu_m)\left[\frac{G_p}{\widetilde{G}_m(s)} - \left(\frac{G_p}{\widetilde{G}_m(s)} - 1\right)V_p\right]} \right]_{s \to \frac{0.56}{t}} \tag{4}$$

where $G(t)$, $\widetilde{G}_m(s)$, G_p, ν_m, V_p, and s = shear relaxation modulus of asphalt concrete mixture (in time domain), Carson-transformed shear modulus of matrix phase, elastic shear modulus of aggregate particles, Poisson's ratio of matrix phase, volume fraction of aggregate particles, and Laplace variable.

Using Equation 4, the shear relaxation modulus can be plotted as a function of time. Data plots between relaxation modulus and time require a curve-fitting function to be used in the calculation of the linear viscoelastic response in a constitutive equation. Among many curve-fitting functions, the Prony series based on the generalized Maxwell model fits the data more mathematically efficiently than the other functions. The Prony series expression of the relaxation modulus is given as:

$$G(t) = G_\infty + \sum_{i=1}^{n} G_i \exp\left(-\frac{t}{\rho_i}\right) \tag{5}$$

where G_∞, G_i, ρ_i, and n = long-time equilibrium modulus, spring constants in the generalized Maxwell model, relaxation time, and number of Maxwell units in the generalized Maxwell model.

The parameters from the Prony series representation shown in Equation 5 are used to calculate the storage and loss moduli (Equations 6 and 7), which are used to obtain the corresponding dynamic shear modulus as a function of loading frequency (Equation 8).

$$G'(\omega) = G_\infty + \sum_{i=1}^{n} \frac{G_i \omega^2 \rho_i^2}{\omega^2 \rho_i^2 + 1} \tag{6}$$

$$G''(\omega) = \sum_{i=1}^{n} \frac{G_i \omega \rho_i}{\omega^2 \rho_i^2 + 1} \tag{7}$$

$$\left|G^*(\omega)\right| = \sqrt{\left[G'(\omega)\right]^2 + \left[G''(\omega)\right]^2} \tag{8}$$

where $|G^*(\omega)|$, $G^*(\omega)$, $G'(\omega)$, $G''(\omega)$, and ω = dynamic shear modulus, complex shear modulus, storage shear modulus, loss shear modulus, and angular frequency.

Assuming that Poisson's ratio of asphalt concrete mixtures is a constant, dynamic modulus based on Hashin's analytical micromechanics approach can be finally expressed as follows:

$$\left|E^*(\omega)\right| = 2\left|G^*(\omega)\right| \cdot (1+\nu) \tag{9}$$

where $|E^*(\omega)|$ and ν = dynamic modulus of mixture and Poisson's ratio of mixture.

Kim and Little (2004) found that Hashin's model can accurately predict the stiffening effect of fillers in the asphalt mastic when the volume fraction of fillers in the mastic is low.

However, model predictions diverged from the testing data at high-volume fractions. This indicates the presence of significant particle interactions and potential physico-chemical reinforcement between binder and filler. Irregular particle shape and rough texture might be other variables that introduce variance between model predictions and test data, because Hashin's model was developed for composites containing perfectly spherical particles without particle-matrix interaction.

The analytical models represent a huge scientific advancement of the 20th century in the prediction of the behavior of composite materials. However, the complicated characteristics of highly heterogeneous particulate composites such as asphalt mixtures limit the predictive capabilities of these analytical models because their derivation is often accompanied by several inevitable geometrical assumptions.

Computational models based on well-known numerical methods (*e.g.,* finite element and discrete element methods - FEM and DEM, respectively) have been actively pursued by the pavement mechanics community as an alternative to empirical and analytical formulations. To better understand the effects of individual mixture components and their interactions on asphalt mixtures, many researchers (Buttlar and You, 2001; Masad *et al*., 2002; Papagiannakis *et al*., 2002; Sadd *et al*., 2003; Soares *et al*., 2003; You and Buttlar, 2004, 2005, 2006; Abbas *et al*., 2005; Dai *et al*., 2005; Kim and Buttlar, 2005; Dai and You, 2007; Aragão *et al*., 2009a, 2009b, 2010; You *et al*., 2009; Aragão and Kim, 2010; Kim *et al*., 2010) have recently attempted microstructure-based computational approaches.

The computational microstructure modeling also appears to be more attractive than the continuum damage mechanics approach because the latter considers the damaged body as a homogeneous continuum on a scale that is much larger than that of the size of the cracks. The

heterogeneity of the asphalt samples is not considered and damage in the samples is typically represented by phenomenological internal state variables (ISVs). ISVs are determined by matching damage evolution characteristics from laboratory testing results through regression analyses. On the other hand, the computational microstructure approach accounts for the different properties of various mixture constituents, the heterogeneity of the mixtures, and the appropriate damage evolution characteristics to describe the fracture process in a more realistic scale.

Among the main features that should be included in the microstructure-based approaches, the most important are probably the consideration of: mixture heterogeneity, spatial distribution of particles, contact among ingredients, air voids within the mixtures, and three-dimensional geometric characteristics of the samples. It is also very important to obtain the undamaged and damage-related material properties of the different mixture constituents with reliable and preferably fast laboratory testing procedures.

To account for the mixture heterogeneity, researchers have proposed digital image techniques that accurately reproduce the inner microstructure, *i.e.*, spatial distribution of aggregates within a fine aggregate asphalt matrix (FAM) phase (fine aggregates + asphalt mastic + entrained air voids) of the asphalt mixture specimens. One example of such techniques has been heavily pursued by Masad *et al*. (1999a, 1999b) is illustrated in Figure 1. Several researchers, *e.g.*, Papagiannakis *et al*. (2002); Aragão *et al*. (2009a, 2009b, 2010), have used the two-dimensional digital image techniques (presented in Figure 1) similar to the method proposed by Masad and his colleagues. Another approach that has recently been attempted by several researchers is the use of three-dimensional X-ray computed tomography (CT) image technique (see Figure 2), as presented in several studies (Wang *et al*., 2001; Tashman *et al*., 2004; Masad *et*

al., 2005; You *et al*., 2009).

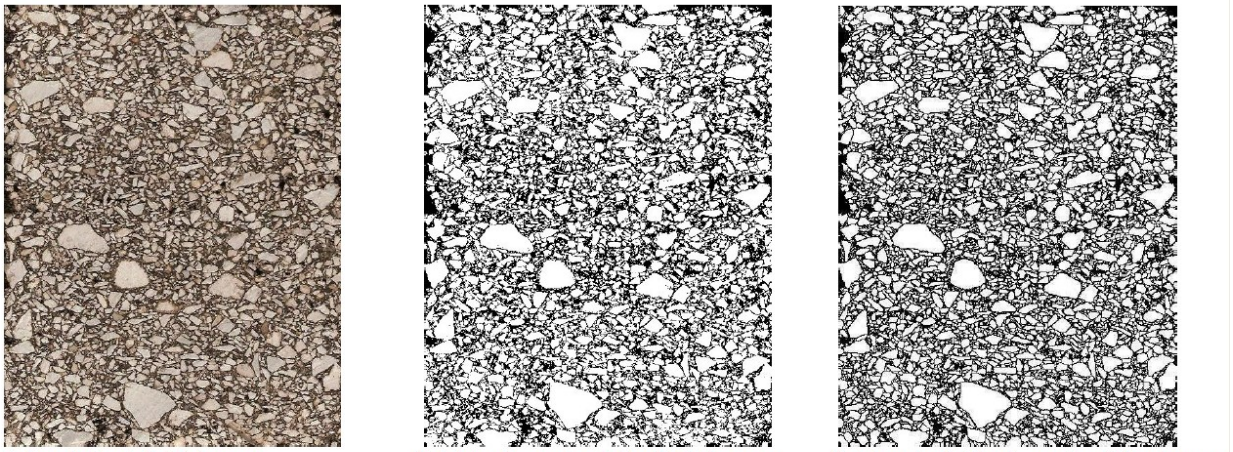

Figure 1. Digital image technique to generate 2-D microstructure of asphalt mixtures.

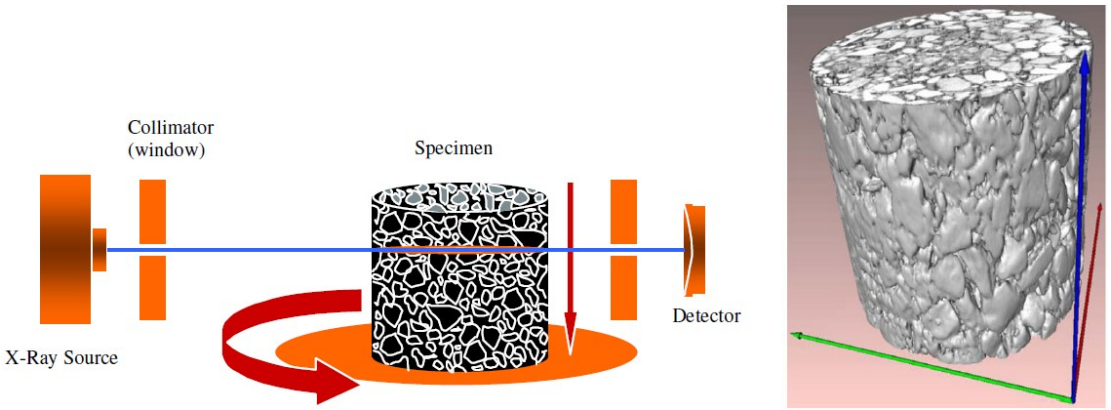

Figure 2. Three-dimensional CT image analysis technique (Masad *et al*., 2005 and You *et al*., 2009).

Another important ingredient that has been considered by researchers is the component-to-component contact. Many studies by You and his colleagues (You and Buttlar, 2004 and 2005; Dai and You, 2007) and others (Papagiannakis *et al*., 2002; Abbas *et al*., 2005) included the contact mechanisms in the prediction of stiffness characteristics of asphalt materials. As illustrated in Figure 3, two spherical particles are in contact through a thin film of softer material,

which was assumed to be elastic and to transfer normal and shear stresses in linear fashion through two elastic springs. It was observed that the contact stiffness decreases with the increasing film thickness. Abbas *et al*. (2005) proposed a simple linear contact model to be activated whenever the distance between the centroids of two adjacent particles becomes less than or equal to the sum of their radii. The idea of damage is also introduced with the use of two material strength parameters (You and Buttlar, 2004). When stress levels at a contact exceed the bond strength, that bond breaks and separation occurs. You and Buttlar (2004) also defined a friction force between the contacting bodies.

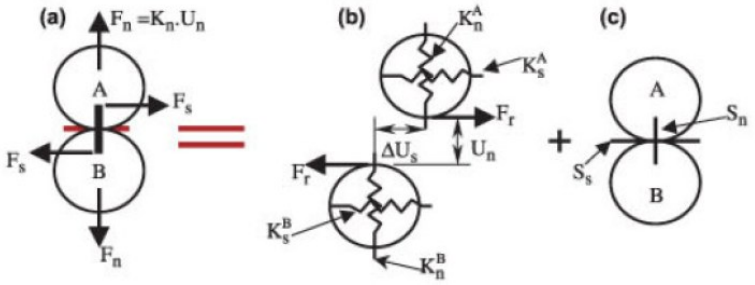

Figure 3. Contact model: (a) Two bonded particles; (b) Linear contact model; and (c) Normal and shear bond strength (You and Buttlar, 2004 and Dai and You, 2007).

In addition to the geometric complexities and materials contact, one of the most significant challenges that the computational microstructure modeling has faced so far is the proper characterization of damage such as cracking. Modeling the initiation and coalescence of micro-cracks into macro-cracks and the propagation of those macro-cracks is a very complicated task. The level of difficulty significantly increases if the model includes challenges, such as rate-dependent inelastic behavior and interactions among the constituents in the mixtures. Recognizing the importance of these factors for better predictions, researchers have been adopting the microstructural approach (Guddati *et al*. 2002; Soares *et al*. 2003; Paulino *et al*.

2004; Dai *et al*. 2005, 2006; Kim *et al*. 2005, 2006a, 2007; Song *et al*. 2006a, 2006b) to model the discrete cracking phenomenon in asphalt concrete mixtures.

One option to model cracking within the microstructure of asphalt mixtures is through the use of the cohesive zone (CZ) modeling concept. CZ modeling is a well-established way to model crack development in monolithic and composite materials, not only because it removes the stress singularity at the crack tip but also because it provides a powerful and efficient tool which can be implemented in various computational methods, such as FEM and DEM. Moreover, the CZ approach can model cracks along bi-material interfaces (such as aggregate-binder interfaces) which are often considered weak zones susceptible to cracking.

As shown in Figure 4, CZ models regard fracture as a gradual phenomenon in which separation (δ_n in Figure 4) takes place across an extended crack tip, or cohesive zone (fracture process zone) and where fracture is resisted by cohesive tractions (T_n in Figure 4) that vary from T_{max} (cohesive strength) to 0, when a critical displacement, δ_c, is reached and the faces of the cohesive element are fully separated. CZ elements are placed between continuum elements (in either homogeneous or heterogeneous objects) to represent progressive separation of a material. The CZ effectively describes the material resistance when material elements are being displaced. Since the crack path follows specified CZ elements, the direction of crack propagation depends on the presence of cohesive zones, implying that the crack path is mesh-dependent. However, refining the mesh could resolve this problem.

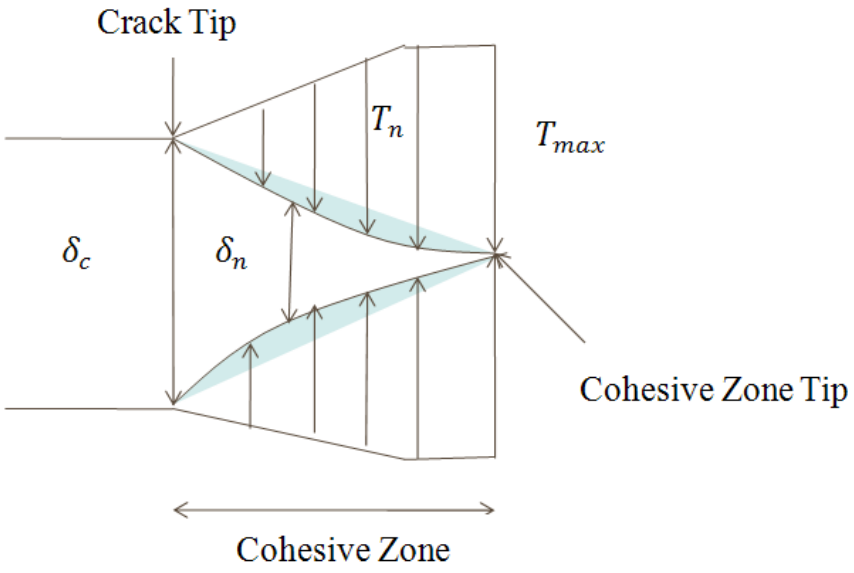

Figure 4. Illustration of cohesive zone concept for mode I fracture.

Equations relating normal and tangential displacement jumps across the cohesive surfaces with the proper tractions define a CZ model. An examination of the open literature reveals the existence of numerous CZ models (Dugdale, 1960; Barenblatt, 1959, 1962; Needleman, 1987, 1990a, 1990b; Rice and Wang, 1989; Tvergaard, 1990; Tvergaard and Hutchinson, 1992; Allen *et al*., 1994; Camacho and Ortiz, 1996; Geubelle and Baylor, 1998; Ortiz and Pandolfi, 1999; Yoon and Allen, 1999; Allen and Searcy, 2001; Espinosa and Zavattieri, 2003; Park *et al.*, 2010).

The different CZMs proposed in the literature can be distinguished by two main characteristics: (1) the shape of the traction-separation curve and (2) the existence of an initial cohesive stiffness. The influence of the shape of the traction-separation laws on the overall responses of bodies subjected to damage has been assumed to have no significant effect (Rahulkumar *et al*., 2000; Hutchinson and Evans, 2000; Mohammed and Liechti, 2000). However, more careful analyses revealed that cohesive strength and work of separation should not be considered as the only two important parameters defining the CZ model. The shape of the

traction-separation curve directly affects the numerical simulation of the fracture process (Chandra *et al*., 2002; Volokh, 2004; Song *et al*., 2008).

The second distinctive characteristic is the existence of an artificial initial stiffness in the cohesive zone model. Models where the artificial initial stiffness is considered are called intrinsic models, whereas models assuming initial rigidity for the cohesive zones are called extrinsic models. In the intrinsic models, the traction-separation relation is such that with increasing separation, the traction across the cohesive zone reaches a maximum, then decreases and eventually vanishes, indicating a complete decohesion (separation). The material constants are cohesive zone parameters, which characterize the fracture behavior of the material. In general, cohesive zone models are described by three parameters: work of separation, cohesive strength, and critical displacement. In contrast, the extrinsic cohesive zone model does not display the initial ascending trend in the traction-separation curve. It is assumed that separation occurs when cohesive zone traction reaches the cohesive strength of the material, and once the separation occurs, the cohesive zone traction decreases as separation continues.

Intrinsic formulations are easier to implement, but may become very computationally expensive because many cohesive elements need to be inserted *a priori* within the FE meshes. Thus, the possible cracked configurations of the bodies are limited by the topology of the FE discretization. The crack path is constrained by the inter-element boundaries. This mesh-dependence has been reported by several researchers (Miller *et al*., 1999; Xu and Needleman, 1994; Scheider and Brocks, 2003). This problem can evidently be contoured by the generation of very highly refined meshes. Several researchers have also reported problems associated with the artificial compliance in the response of the bodies of interest to externally applied loads due to the assumption of the initial artificial stiffness in the traction-separation relations of intrinsic CZ

models. This phenomenon is related to the assumption made in intrinsic CZ models where discontinuities in the displacement fields happen in the uncracked body. As a result, an artificial compliance rises at the inter-element boundaries and the corresponding stiffness of that imaginary spring introduced between bulk elements depends on the initial stiffness of the intrinsic CZ model. This problem may be effectively controlled if a cohesive zone law with linear pre-peak traction-separation relation is used (Geubelle and Baylor, 1998; Espinosa *et al*., 2000; Zavattieri and Espinosa, 2001; Espinosa and Zavattieri, 2003; Song *et al*., 2006a; Shukla *et al*., 2009). This is done by assuming very high values of the initial stiffness in the model (Alfano and Crisfield, 2001; Klein *et al*., 2001). However, the use of "too stiff" initial cohesive stiffness can generate problems with stability and restrict severely the simulation time steps. Espinosa and Zavattieri (2003) suggested a scheme in which two time steps, the standard time step related to the properties of the bulk material and the second time step named by the authors as the cohesive time step, are calculated and the smallest between the two is taken as the overall time step.

Contrary to the intrinsic cases, extrinsic models are more realistic because they do not assume the pre-existence of cohesive zones within the FE meshes. This characteristic is generally referred to as "initial rigidity". Cohesive elements are inserted as needed by node duplication (process generally referred to as dynamic or adaptive insertion) in the mesh whenever a damage initiation criterion is reached. This initial rigid response makes adjacent continuum elements remain concurrent before the initiation of the fracture process, eliminating the problem of artificial compliance prior to fracture. The node duplication process is followed by the gradual reduction in the load bearing capacity of the cohesive element and by the eventual complete failure of that element after the characteristic interfacial separation is reached. However, this

automatic insertion scheme needs extra implementation efforts because it requires the continuous update of the node numbering within the mesh as edges of continuum elements are duplicated to simulate the propagation of cracks. This topic has been recently investigated by several researchers (Pandolfi and Ortiz, 1998 and 2002; Mota *et al*., 2008). Challenges associated with the use of extrinsic CZ models include the difficulties related to the continuous update of the node numbering as cohesive elements are inserted in the meshes and mesh dependency (Ruiz *et al*., 2001; Zhou and Molinari, 2004; Papoulia *et al*., 2003).

Table 1 (Shet and Chandra, 2002) summarizes some of the popular cohesive zone models developed by researchers with specific purposes regarding the shape of the cohesive zone traction-separation curve and the model parameters involved. Representative problems attempted and solved by using each cohesive zone model are also presented in the table. As shown in the table, the work of separation, cohesive strength, and the critical displacement are typically key parameters that can be obtained from fracture tests. The cohesive zone model has been used in various applications and materials (ductile to quasi-brittle), because it can provide an ideal framework to model strength, stiffness, and failure in an integrated manner.

Table 1. Various cohesive zone models and their parameters (Shet and Chandra, 2002).

Year and author	Proposed Model	Model parameters	Problem solved	Model constants	Comments
(1) 1959, 1962 Barenblatt [4,5]	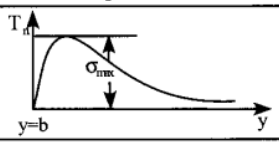	$K = \int_0^{4a} \frac{G_1(t)dt}{\sqrt{t}} = \sqrt{\frac{\pi E T}{1-\nu^2}}$ (ductile) $= \sqrt{\frac{\pi E T_0}{1-\nu^2}}$ (brittle) $T = T_0 + T_1$ T_0 = work of separation for britt. mater. T_1 = work of plastic deformation	Perfectly brittle materials.		The first to propose the cohesive zone concept.
(2) 1960 Dugdale [6]	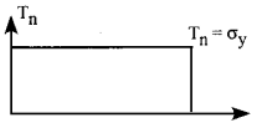	$\frac{s}{a} = 2 \sin^2\left(\frac{\pi}{4}\frac{T}{\sigma_y}\right)$ For small value of T/σ_y $\frac{s}{l} = 1.23\left(\frac{T}{\sigma_y}\right)^2$	Yielding of thin ideal elastic-plastic steel sheets containing slits.	Plastic zone ranges from 0.042 to 0.448 (in.)	Cohesive stress equated to yield stress of material.
(3) 1987 Needleman [16]	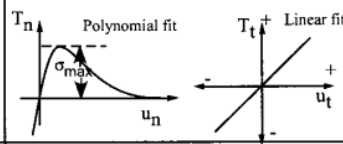	ϕ_{sep} = work of separation δ = normalizing parameters σ_{max} = cohesive strength	Particle-matrix decohesion.	$\delta = 10^{-9}$ to 10^{-8}m Cohesive Energy 1 to 10 J/m 2 $\sigma_{max} = 1000 - 1400$MPa $\sigma_y = 350 - 450$MPa	Phenomenological model. predicts normal separation
(4) 1989 Rice & Wang [17]	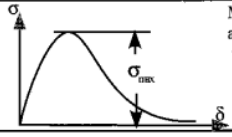 Model based on atomic fit of the type $(1+x)e^{-x}$	E_0 = initial Young's modulus h = normalizing parameter σ_{max} = max imum stress α = constant $(\frac{E_0 h}{\alpha^2} = 2\gamma)$	Solute segregation.		Ascending part is equated to E_0 considers normal separation and ignores shear separation.
(5) 1990 Needleman [13]	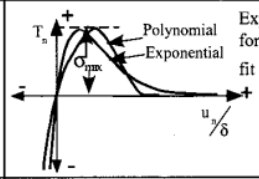 Exponential fit for T_n. Linear fit for T_t	ϕ_{sep} = work of Separation δ = normalizing parameters σ_{max} = cohesive strength	Particle-matrix decohesion.	$\delta = 10^{-9}$ to 10^{-8}m	Predicts normal separation.
(6) 1990 Needleman [18]	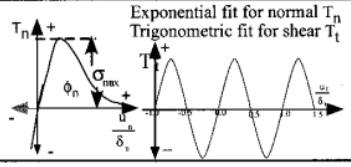 Exponential fit for normal T_n Trigonometric fit for shear T_t	ϕ_n, ϕ_t = work of normal and shear separation δ_n, δ_t = critical displacements σ_{max} = cohesive strength	Decohesion of interface under hydrostatic tension.	$\delta_n = \delta_t = 2 \times 10^{-10}$ to 2×10^{-9} m $J_{IC}/\phi_n = 0.57 \sim 2.59$ $\sigma_{max}/\sigma_0 = 2,3$	Periodic shear traction to model Pieriels shear stress due to slip.

Year and author	Proposed Model	Model parameters	Problem solved	model constants	Comments
(7) 1990 Tvergaard [20]	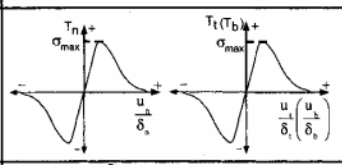	δ_n, δ_t = critical displacements σ_{max} = cohesive strength	Interfaces of whisker reinforced metal matrix composites	$\delta_n = \delta_t = 1\times10^{-9}$m. E = 60GPa (Young's mod) $\sigma_y/E = 0.005$ $\sigma_{max}/\sigma_y = 5\sim9$	Quadratic Model.
(8) 1992 Tvergaard & Hutchinson [19]	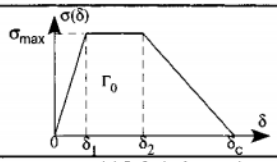	Γ_0 = work of separation. δ_c = critical displacement σ_{max} = peak normal traction/interface strength δ_1, δ_2 = factors governing shape	Crack growth in elasto-plastic material, peeling of adhesive joints	$\Gamma_{ss}/\Gamma_0 = 0\sim10$. ($\Gamma_{ss}$ = Pl wk.), $\delta_s^c/\delta_t^c = 1$ $\sigma_{max}/\sigma_y = 0\sim14$ $\delta_1, \delta_2 = 0.15,\ 0.5$ $\sigma_y/E = 1/300$	Claims shape of separation law are relatively unimportant.
(9) 1993 Xu & Needleman [14]	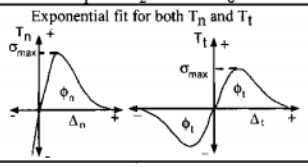	ϕ_n = work of normal separation ϕ_t = work of shear separation δ_n, δ_t = critical displacements σ_{max} = cohesive strength	Particle-matrix decohesion	$\delta_n = \delta_t = 2\times10^{-10}$ to 2×10^{-9} m	Predicts shear and normal separation.
(10) 1996 Camacho and Ortiz [9]	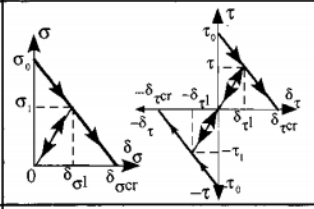	σ_0, τ_0 = normal and shear stress at fracture initiation $\delta_{\sigma cr}, \delta_{\tau cr}$ = critical normal and shrear opening displacement G_c = fracture energy	Impact	Alumina: σ_0 = 400 MPa $\delta_{\sigma r} = 1.7\times10^{-7}$m Steel: $\sigma_0 = 1500$MPa $\delta_{\sigma cr} = 5.43\times10^{-6}$m	Uses additional fracture criterion. Predicts failure by both shear and normal separation in tension and by shear separation in compression.
(11) 1997 Geubelle & Bayler [21]	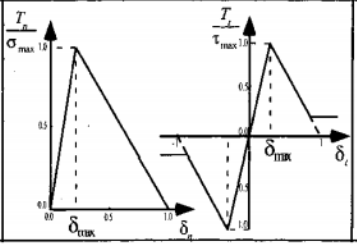	ϕ_n, ϕ_t = work of normal and tangential separation Δ_n, Δ_t = normal and tangential displacement jump δ_n, δ_t = normal and tangential interface characteristic length	Delamination by low-velocity impact	σ_{max} = E/100 to E/10 critical normal displacement jump $\Delta_n^c = 10^{-3}\sim10^{-4}$m	Bilinear model. Ascending curve can be matched to initial stiffness of the material.

The cohesive zone modeling approach has received increasing attention from the asphalt mechanics community. This is because it is useful and powerful for modeling both brittle and ductile failure, which are frequently observed in asphalt mixtures due to the wide range of service temperatures and loading rates to which it is subjected.

The cohesive zone modeling approach in asphalt materials and flexible pavements was first employed by Jeng and his colleagues (Jeng and Perng, 1991; Jeng *et al*., 1993) to model crack resistance and propagation in asphalt pavement overlays. Recently, the cohesive zone modeling concept has been actively implemented in the modeling of asphalt concrete, particularly to simulate fracture with the consideration of the bulk material inelasticity. It has been well known that the asphaltic materials are rate-dependent and temperature sensitive due to

the asphalt binder phase in the mixture. Thus, the assumption of linear elasticity for the bulk material is not appropriate to produce accurate results. Examples of research efforts considering the inelasticity of the bulk material in asphalt mixtures are presented in various studies including Souza *et al*. (2004), Kim *et al*. (2005, 2006, 2007); Song *et al*. (2006a, 2008); Aragão *et al*. (2009b); Kim and Buttlar (2009); Aragão and Kim (2010); and Kim *et al*. (2010).

Another important aspect of the current computational models based on the cohesive zone concept is the experimental procedures to characterize the cohesive zone fracture properties. The most common geometry used for the fracture testing of asphalt concrete has probably been the single-edge notched beam specimen (SE(B)) (Mobasher *et al*., 1997; Marasteanu *et al*., 2002). To obtain cohesive fracture energy, Wagoner *et al*. (2005a) proposed a testing protocol that used the SE(B) geometry. Song *et al*. (2006b) and Kim *et al*. (2009) used the methodology proposed by Wagoner *et al*. (2005a) to calibrate cohesive fracture parameters used in their microstructural FEM and DEM simulations, respectively. The main problems with the use of SE(B) geometry to routinely obtain fracture properties of asphalt mixtures are that the fabrication of specimens in the laboratory becomes impractical and that it is not often viable to extract beam specimens from mixtures in the field.

With the limitations of the SE(B) geometry, Wagoner *et al*. (2005b, 2005c) proposed a testing protocol using a disk-shaped compact tension test (DC(T)), which is similar to the DC(T) geometry proposed in ASTM E399 (2008) but with a longer pre-crack to avoid premature fracture at the loading holes (see Figure 5). Researchers at the University of Illinois at Urbana-Champaign (UIUC) have combined the fracture energy from the DC(T) tests conducted as proposed by Wagoner *et al*. (2005b and 2005c) (especially at low temperatures) with the strength

of the asphalt mixtures obtained from indirect tension (IDT) specimens (AASHTO T322-03) to perform their fracture simulations (Song *et al*., 2006a).

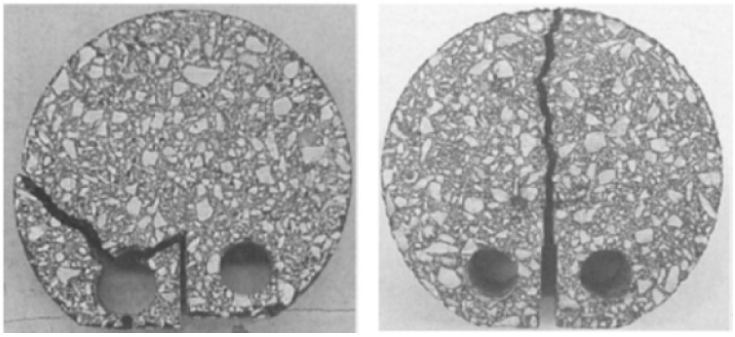

Figure 5. Crack growth in the initial and modified DC(T) specimen geometry (Wagoner *et al*., 2005b).

The researchers at the University of Nebraska - Lincoln (UNL) have also been involved in the experimental characterization of cohesive zone fracture properties of asphalt materials. Two different specimen geometries have been attempted by the researchers: an in-house developed small-scale tensile fracture test geometry (Freitas, 2007; Freitas *et al.*, 2007, Aragão *et al*., 2011) and the semi-circular bend (SCB) geometry as presented in Figure 6. Aragão *et al*. (2009b) has used the small-scale tensile fracture testing methodology to obtain cohesive fracture properties of FAM samples. Even if promising results were found from the study by Aragão *et al*. (2009b), the researchers at the University of Nebraska have further attempted to develop a simpler testing protocol that uses equipment and devices available to many researchers and department of transportation (DOT) engineers. The new geometry considered was the SCB. The semi-circular bend specimen has been used by many researchers (Basham *et al*., 1990; Khalid and Artamendi, 2008; Mohammad and Kabir, 2008; van Rooijen and de Bondt, 2008, Li and Marasteanu, 2004 and 2010, and many more) to obtain fracture toughness, fracture energy, and stress-softening curves of various types of brittle and semi-brittle materials. SCB testing is more

advantageous than other types of fracture tests, due to its relatively simple testing configuration, more economical aspects in specimen fabrication (two testing specimens are produced from one cylinder sample which can easily be obtained from a Superpave gyratory compactor and field cores), and its repeatable testing results. The testing set-up currently used by the UNL researchers is shown in Figure 6b.

Using the testing set-up shown in Figure 6b, the present research combines experimental tests and computational modeling to characterize the rate-dependent distribution of cohesive fracture properties (*i.e.*, cohesive strength and fracture energy) as a function of separation rates. As also shown in Figure 6b, high speed cameras of a digital image correlation (DIC) system are used to monitor the local fracture behaviors at the initial notch tip of the SCB specimens. DIC is an easy-to-use, non-contact technique that makes use of high-resolution video cameras to capture time-varying deformations of a specimen. Using image analyses, it compares full-field deformation, including crack tip behavior at a certain loading time, with the initial configuration.

The combination of experimental testing with numerical simulations of simple tests such as the SCB test may provide more realistic results of cohesive fracture properties than traditional approaches because those traditional approaches generally rely on globally averaged material deformations or displacements (*e.g.*, crack-mouth opening displacements - CMOD) obtained far from the actual fracture process zone to estimate the local fracture energy (*i.e.*, at the fracture process zone) of the testing specimens. That fracture energy is generally obtained by calculating an area under the load-CMOD curve that is normalized by the area of the fractured surface, *i.e.*, initial ligament length multiplied by the specimen thickness. This approach may lead to an overestimation of the true fracture energy of the materials because several sources of energy dissipation such as material viscoelasticity are involved in the energy calculations. Additionally,

these traditional testing protocols also require supplementary experimental testing (*e.g.*, IDT tests) for the characterization of the cohesive strength of the mixtures. The approach proposed in this dissertation only requires one type of experimental testing to characterize both cohesive fracture properties locally at the fracture process zone of the cracked specimens.

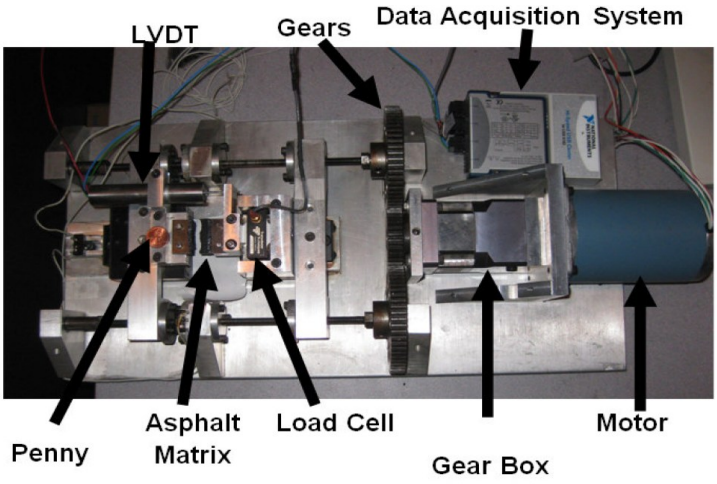

(a)

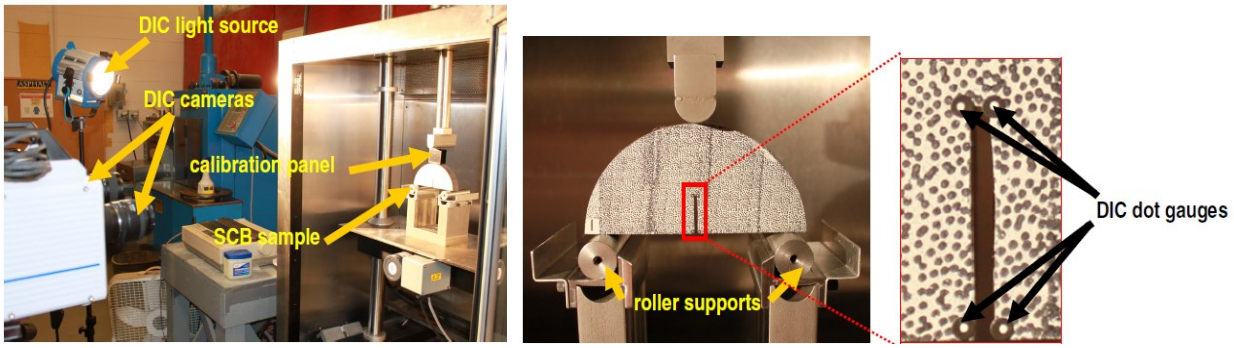

(b)

Figure 6. (a) Small-scale Tensile Fracture Testing; and (b) SCB testing to obtain CZ fracture properties of FAM specimens.

Another very important feature that has been neglected in the current computational microstructure models available in the literature is the rate-dependent fracture behavior of asphalt mixtures. It is a common sense in the pavement mechanics community that asphalt

mixtures present a global mechanical behavior that is a function of local rates of deformation within the mixture microstructure. That rate-dependence is related to several factors such as the viscoelasticity of the bulk matrix and the fracture characteristics throughout the fracture process zone (Souza *et al.*, 2004; Kim *et al.*, 2007). Thus, the mere consideration of the rate-dependence associated to the viscoelastic behavior of the bulk material is not enough to fully model the rate-dependent responses of the mixtures when those are subjected to damaging loads. Models that account for the local rate-dependent fracture behavior at the fracture process zone (*e.g.*, Yoon and Allen, 1999; Rahulkumar *et al.*, 2000; Allen and Searcy, 2001) of asphalt mixtures must be sought and implemented.

Chapter 3

Model Formulation

In this chapter, an introduction to the initial boundary value problem (IBVP) for a general elastic-viscoelastic composite containing cracks is first presented. Then, a short discussion on the formulation of the intrinsic bilinear cohesive zone model chosen for the fracture simulations in this study is provided.

3.1. IBVP Formulation

Figure 7 shows a general body containing discrete cracks with cohesive zones. The body has an interior volume V and a boundary ∂V that is composed of two parts: ∂V_e (external boundary) and ∂V_c (internal boundary normally with cohesive zones). The state variables to be predicted by the model are the displacement vector $u_i(x_m,t)$, the stress tensor $\sigma_{ij}(x_m,t)$, and the strain tensor $\varepsilon_{ij}(x_m,t)$, where x_m are the spatial coordinates and t is time. In the absence of body forces and inertial effects, the conservation of linear momentum can be expressed by:

$$\sigma_{ji,j} = 0 \text{ in volume } V \tag{10}$$

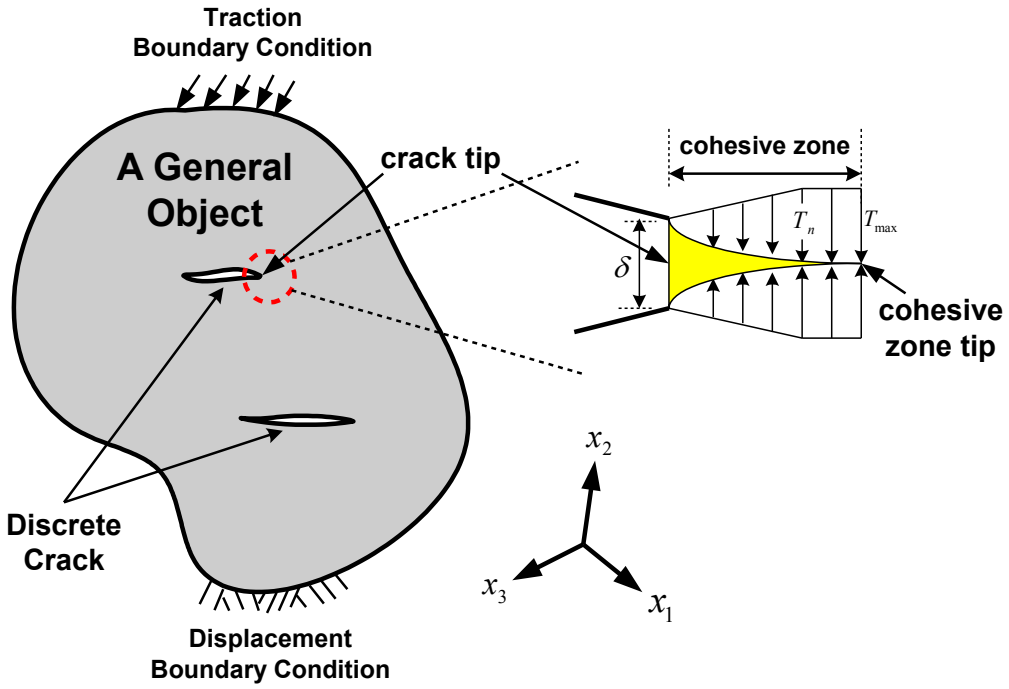

Figure 7. Schematic representation of the cohesive zone concept for a pure mode I fracture.

By neglecting body moments, the conservation of angular momentum implies that the stress tensor must be symmetric. The linearized form of the strain-displacement relationship for small strains is given by:

$$\varepsilon_{ij} = \frac{1}{2}(u_{i,j} + u_{j,i}) \text{ in volume } V \tag{11}$$

The linear elastic constitutive relationship can be expressed as:

$$\sigma_{ij}(x_m, t) = C^E_{ijkl}\varepsilon_{kl}(x_m, t) \text{ in volume } V \tag{12}$$

where C^E_{ijkl} = elastic modulus tensor, which is not time-dependent.

If the material is linear viscoelastic, the constitutive equation may be represented by a convolution integral of the form:

$$\sigma_{ij}(x_m,t)=\int_0^t C_{ijkl}(t-\tau)\frac{\partial\varepsilon_{kl}(x_m,\tau)}{\partial\tau}d\tau \text{ in volume } V \tag{13}$$

where C_{ijkl}, t, and τ = stress relaxation modulus tensor (which is time-dependent), time of interest, and integration variable.

The linear viscoelastic relaxation modulus is determined by performing laboratory constitutive tests, such as static creep/relaxation tests or dynamic frequency sweep tests, where testing is performed within the limits of linear viscoelasticity. Testing results can be represented by a mathematical form such as a Prony series based on the generalized Maxwell model. The linear viscoelastic stress relaxation modulus can be expressed as:

$$C_{ijkl}(t)=\left[C_{ijkl}\right]_{,\infty}+\sum_{p=1}^{M}\left[C_{ijkl}\right]_{,p}\exp\left(-\frac{\left[C_{ijkl}\right]_{,p}}{\left[\eta_{ijkl}\right]_{,p}}t\right) \tag{14}$$

where $\left[C_{ijkl}\right]_{,\infty}$ and $\left[C_{ijkl}\right]_{,p}$, $\eta_{ijkl,p}$, and M = spring constants in the generalized Maxwell model, dashpot constants in the generalized Maxwell model, and the number of Maxwell units.

At the crack tips the cohesive zones have constitutive behavior that reflects the change in the cohesive zone material properties due to microscopic damage accumulation ahead of crack tips. This behavior may be expressed by the relationship between the cohesive zone traction and separation displacement as follows:

$$T_i(x_m,t)=T_i\left\{\Delta_i(x_m,t)\right\} \text{ on } \partial V_c \tag{15}$$

where T_i and Δ_i = cohesive zone traction vector and cohesive zone displacement, and the symbol { } is used to imply time- and history- dependence for damaged zones, since the cohesive zone internal boundary (*i.e.*, crack) typically varies with time.

The initial condition for all state variables are known and assumed to be zero, *i.e.*:

$$\sigma_{ij}(x_m, t=0) = 0 \text{ in the volume } V \text{ and on the boundary } \partial V$$

$$\varepsilon_{ij}(x_m, t=0) = 0 \text{ in the volume } V \text{ and on the boundary } \partial V \tag{16}$$

$$u_i(x_m, t=0) = 0 \text{ in the volume } V \text{ and on the boundary } \partial V$$

In addition, either tractions or displacements are specified along sub-sets of the boundary of the body. These general mixed boundary conditions are:

$$T_i(x_m, t) = \hat{T}_i \text{ on } \partial V_{e1}, \tag{17}$$

$$u_i(x_m, t) = \hat{u}_i \text{ on } \partial V_{e2}. \tag{18}$$

where $\hat{T}_i$ and $\hat{u}_i$ = known boundary tractions and known boundary displacements.

With Equations 10 through 18, the above IBVP is well-posed. A solution to this problem generally exists and is obtainable analytically and/or numerically.

3.2. Cohesive Zone Concept and Bilinear Cohesive Zone Model

As previously mentioned, cohesive zone models define fracture process by relating cohesive zone tractions that resist to the separation displacements at the cohesive zone. The traction-separation relation has been proposed by many researchers in different forms. This research uses

an intrinsic bilinear cohesive zone model (Geubelle and Baylor, 1998; Espinosa and Zavattieri, 2003) as presented in Figure 8. The bilinear model has the ability to reduce the artificial compliance effect by providing an adjustable initial slope in the cohesive law. The model assumes that there is a recoverable linear elastic behavior until the traction reaches the peak value in the traction-separation curve.

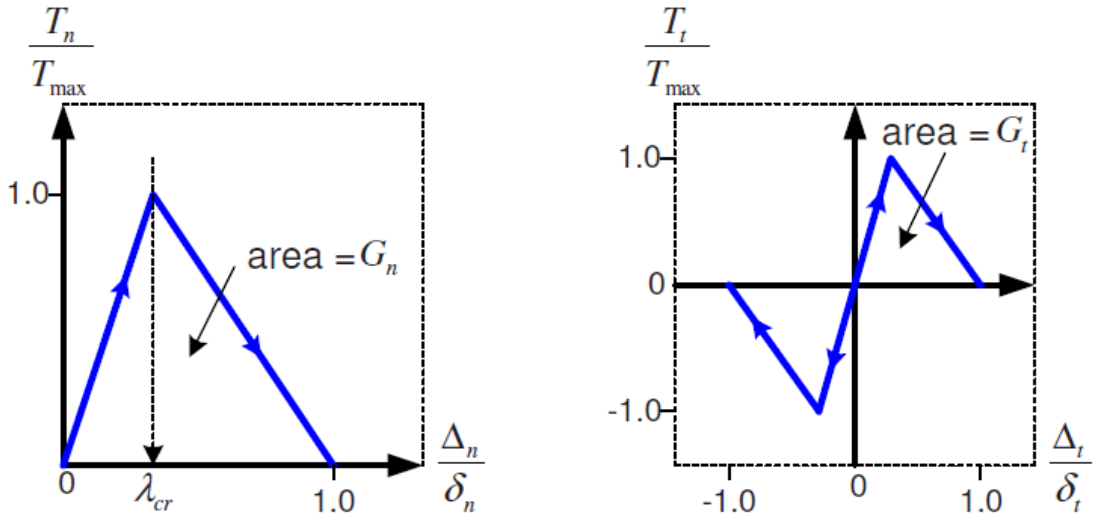

(a) in pure tension (mode I) (b) in pure shear (mode II)

Figure 8. Bilinear cohesive zone model (normalized traction versus normalized separation).

The non-dimensional effective displacement for a two-dimensional case can be given (Espinosa and Zavattieri, 2003) by:

$$\lambda_e = \sqrt{\left(\frac{\Delta_n}{\delta_n}\right)^2 + \xi^2\left(\frac{\Delta_t}{\delta_t}\right)^2} \tag{19}$$

where the subscripts *e*, *n*, *t* represent effective, normal (opening), and tangential (shear sliding), respectively, Δ_n and Δ_t represent the displacement jumps across the cohesive zone, λ is the non-

dimensional displacement, and ξ is the parameter coupling normal and tangential energy release rates.

As shown in Figure 8, cohesive zone traction in the bilinear model increases from zero to a peak value (*i.e.*, cohesive strength, T_{max}) in a linear elastic fashion then presents linear softening that accounts for progressive damage occurring in the fracture process zone. At the maximum traction, a parameter (λ_{cr}) can be identified. The non-dimensional displacement λ_{cr} is considered an important parameter in the bilinear model, since the parameter defines initiation of damage in the fracture process zone, and also controls the pre- and post-peak slopes of the model. Other important displacement quantities, the critical displacements, δ_n and δ_t, represent displacement jumps where complete separation occurs for pure mode I and pure mode II fracture problems, respectively, inferring zero traction.

For the pre-peak region ($\lambda_e \leq \lambda_{cr}$), the normal and tangential components of the traction vector are given by:

$$T_n = \frac{T_{\max}}{\lambda_{cr}} \cdot \left(\frac{\Delta_n}{\delta_n} \right) \tag{20}$$

$$T_t = \frac{\alpha T_{\max}}{\lambda_{cr}} \cdot \left(\frac{\Delta_t}{\delta_t} \right) \tag{21}$$

where $\alpha = \xi^2(\delta_n/\delta_t)$

For the post-peak region ($\lambda_e > \lambda_{cr}$), the normal and tangential components of the traction can be expressed as follows:

$$T_n = \frac{1-\lambda_e}{1-\lambda_{cr}} \cdot \frac{T_{\max}}{\lambda_e} \cdot \left(\frac{\Delta_n}{\delta_n} \right) \tag{22}$$

$$T_t = \frac{1-\lambda_e}{1-\lambda_{cr}} \cdot \frac{\alpha T_{\max}}{\lambda_e} \cdot \left(\frac{\Delta_t}{\delta_t} \right) \tag{23}$$

The cohesive zone fracture energy (*i.e.*, work of separation) is calculated by integrating the cohesive zone traction with respect to the separation distance. The work of separation in pure normal displacement condition (mode I fracture - G_n) and in pure shear sliding condition (mode II fracture - G_t) can be expressed by Equation 24 and Equation 25, respectively.

$$G_n = \int_0^{\delta_n} T_n d\Delta_n = \frac{1}{2} \delta_n T_{\max} \tag{24}$$

$$G_t = \int_0^{\delta_t} T_t d\Delta_t = \alpha \frac{1}{2} \delta_t T_{\max} = \xi^2 \frac{1}{2} \left(\frac{\delta_n}{\delta_t} \right) \delta_t T_{\max} = \xi^2 G_n \tag{25}$$

Equation 25 provides a physical meaning for the parameter ξ.

Another bilinear traction-separation relation has been used by Song (2006a, 2006c). In that model, a critical displacement where complete separation happens, δ_c, is defined. Assuming that $\delta_n = \delta_t = \delta_c$ and that $\alpha = 1$, Equation 20 to 23 can be rewritten as:

For $\lambda_e \leq \lambda_{cr}$,

$$T_n = \frac{T_{\max}}{\lambda_{cr}} \cdot \left(\frac{\Delta_n}{\delta_c} \right) \tag{26}$$

$$T_t = \frac{T_{\max}}{\lambda_{cr}} \cdot \left(\frac{\Delta_t}{\delta_c} \right) \tag{27}$$

For $\lambda_e > \lambda_{cr}$,

$$T_n = \frac{1-\lambda_e}{1-\lambda_{cr}} \cdot \frac{T_{\max}}{\lambda_e} \cdot \left(\frac{\Delta_n}{\delta_c} \right) \tag{28}$$

$$T_t = \frac{1-\lambda_e}{1-\lambda_{cr}} \cdot \frac{T_{\max}}{\lambda_e} \cdot \left(\frac{\Delta_t}{\delta_c} \right) \tag{29}$$

Also assuming that ξ = 1, the cohesive zone fracture energy can be calculated by computing the area below the bilinear traction-separation curve with peak traction $T_{\max}$ and critical displacement δ_c, as follows:

$$G_c = \frac{1}{2} \delta_c T_{\max} \tag{30}$$

The model proposed by Song (2006a, 2006c) has been used in the implementation of the rate-dependent cohesive zone model proposed in the next chapter.

Chapter 4

Rate-Dependent CZ Model

Modeling the fracture behavior of asphalt concrete mixtures is a complex subject due to factors such as heterogeneity, inelastic mechanical behavior, and rate-dependent fracture characteristics of the mixtures. The fracture behavior can be modeled with different approaches, and one that has become popular in the recent years is via the implementation of cohesive zone models, as previously illustrated. Several researchers have used the cohesive zone technique to model the fracture behavior of asphalt mixtures. However, most of the fracture models found in the literature have failed to address the rate-dependent fracture characteristics of the mixtures.

To account for the rate-dependent fracture behavior of asphalt mixtures, a rate-dependent CZ fracture model is presented in this chapter and implemented as a user-element (UEL) subroutine that is incorporated into the mainframe of ABAQUS. Most of the FEM implementation scheme of the rate-independent CZ model proposed by Song (2006c) was used for the proposed rate-dependent model. However, the proposed model represents an improvement to the model proposed by Song (2006c) in the sense that it assigns individual sets of CZ fracture properties (*i.e.,* cohesive strength and fracture energy) to each CZ element in the FEM mesh according to the rates of displacement differences across each CZ element.

4.1. FEM Implementation

This section briefly describes the implementation of a rate-independent CZ model into the mainframe of ABAQUS in the form of a UEL subroutine. The finite element implementation of the contribution of the cohesive elements to the force vector, **f**, and tangent stiffness matrix, **K**, was proposed by Song (2006a) and is reviewed below. This work represents an extension of the UEL subroutine presented by Song (2006c) to incorporate the rate-dependent characteristics of the cohesive zone fracture properties, *i.e.*, cohesive strength and fracture energy. More details about the FEM implementation of the rate-independent CZ model that served as basis for this work can be found in Song (2006c).

Equations 31 and 32 are used by Song (2006a) to define global nodal $\boldsymbol{f}$ and $\boldsymbol{K}$ for a four-noded cohesive element (see Figure 9) in the isoparametric domain $-1 < \xi < 1$.

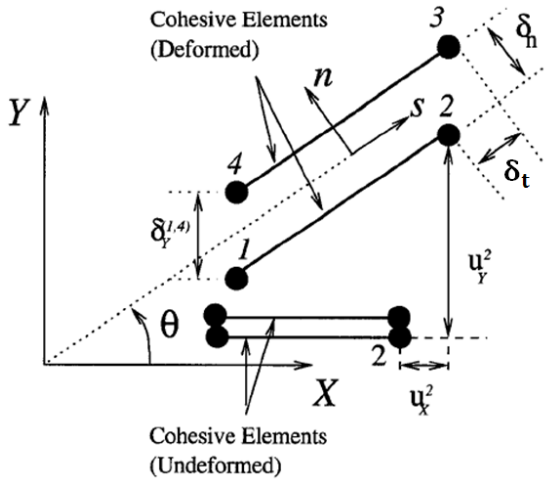

Figure 9. Four-node cohesive element (Song, 2006a).

$$\boldsymbol{f} = \int_{-1}^{1} \boldsymbol{B}^T \boldsymbol{t}\, J_0\, d\xi \tag{31}$$

$$\boldsymbol{K} = \int_{-1}^{1} \boldsymbol{B}^T \boldsymbol{C} \boldsymbol{B}\, J_0\, d\xi \tag{32}$$

where $\boldsymbol{t}$, J_0, and $\boldsymbol{C}$ = traction vector, Jacobian between isoparametric and original coordinates, and tangent modulus matrix. Matrix $\boldsymbol{B}$ is defined as:

$$\boldsymbol{B} = \boldsymbol{R}\,\boldsymbol{N}\,\boldsymbol{L} \tag{33}$$

where $\boldsymbol{R}$ (directional cosines matrix) defines the orthogonal transformation from the global to the local elemental coordinate system, *i.e.*, (*X*, *Y*) to (tangential (or t) and normal (or n) local directions for each cohesive element) in 2-D; $\boldsymbol{N}$ defines the matrix of shape functions and $\boldsymbol{L}$ is an operator matrix used to define the relative displacements δ_X and δ_Y between top and bottom nodes of each cohesive element.

Matrix $\boldsymbol{B}$ is used to transform the global displacement vector, $\boldsymbol{u}$, into the relative local displacement vector, δ_t and δ_n, as follows:

$$\begin{Bmatrix}\delta_t\\ \delta_n\end{Bmatrix} = \boldsymbol{B}\boldsymbol{u} = \boldsymbol{R}\,\boldsymbol{N}\,\boldsymbol{L}\,\boldsymbol{u}$$

or (34)

$$\begin{Bmatrix}\delta_t\\ \delta_n\end{Bmatrix} = \begin{bmatrix}\cos\theta & \sin\theta\\ -\sin\theta & \cos\theta\end{bmatrix}\begin{bmatrix}N_1 & 0 & N_2 & 0\\ 0 & N_1 & 0 & N_2\end{bmatrix}\begin{bmatrix}1 & 0 & 0 & 0 & 0 & 0 & -1 & 0\\ 0 & 1 & 0 & 0 & 0 & 0 & 0 & -1\\ 0 & 0 & 1 & 0 & -1 & 0 & 0 & 0\\ 0 & 0 & 0 & 1 & 0 & -1 & 0 & 0\end{bmatrix}\begin{bmatrix}u_X^1\\ u_Y^1\\ u_X^2\\ u_Y^2\\ u_X^3\\ u_Y^3\\ u_X^4\\ u_Y^4\end{bmatrix}$$

where θ and u_M^n = angle between global and local coordinate systems; and global displacement of node *n* (*n*=1 to 4) in global coordinate *M* (*X* or *Y*). Shape functions N_1 and N_2 are defined in the isoparametric domain as:

$$N_1 = \frac{1}{2}(1 - \xi) \tag{35}$$

$$N_2 = \frac{1}{2}(1 + \xi) \tag{36}$$

The displacement jumps in the local coordinate system, δ_t and δ_n, are used in the computation of the traction vector, $\boldsymbol{t}$, according to the traction-separation cohesive law adopted. To compute the tangent modulus matrix, $\boldsymbol{C}$, one needs to differentiate $\boldsymbol{t}$ with respect to δ_t and δ_n. The components of the tangent modulus matrix are then given by:

$$C_{ij} = \frac{\partial t_i}{\partial \delta_j} \tag{37}$$

where i, j = t or n.

Gaussian quadrature is used to approximate the integral of the functions shown in Equations 31 and 32 at two specified Gaussian integration points, *i.e.*, -0.5773502691896 and 0.5773502691896 with the associated function weights equal to 1.

4.2. Rate-Dependent Cohesive Zone Model

The rate-dependent CZ model uses the same implementation scheme reviewed in the section above. However, the proposed rate-dependent code assigns individual sets of cohesive strength and cohesive fracture energy to each cohesive element in the FE mesh based on the rate of displacement jumps between the two faces of the cohesive elements.

The rate-dependence of the fracture properties is defined via Equations 38 and 39. Equation 38 represents a simplification of the rate- and temperature-dependent expression for cohesive strength defined by Espinosa and Zavattieri (2003) because the consideration of thermal

effects on the fracture properties is out of the scope of this dissertation. A similar rate-dependent expression is assumed for the other CZ property, *i.e.*, the cohesive fracture energy, G_c.

$$T_{max} = T_{max}^{ref} \left\{1 + \beta_T \, ln\left(\frac{\dot{\delta}_e}{\dot{\delta}_e^{ref}}\right)\right\} \tag{38}$$

$$G_c = G_c^{ref} \left\{1 + \beta_G \, ln\left(\frac{\dot{\delta}_e}{\dot{\delta}_e^{ref}}\right)\right\} \tag{39}$$

where $\dot{\delta}_e^{ref}$, T_{max}^{ref}, G_c^{ref}, and β_T and β_G = reference displacement jump rate, cohesive strength at $\dot{\delta}_e^{ref}$, cohesive fracture energy at $\dot{\delta}_e^{ref}$, and model parameters determined with the aid of experimental test results (fracture tests with the SCB geometry in the research). δ_e represents the evolving effective displacement jump in each cohesive element and is calculated as:

$$\delta_e = \sqrt{{\delta_n}^2 + {\delta_t}^2} \tag{40}$$

The effective displacement jump rate, $\dot{\delta}_e = \frac{\partial \delta_e}{\partial t}$, is individually calculated for each cohesive element for separation displacements within the region of recoverable linear elastic behavior of the cohesive traction-separation law. With the calculated $\dot{\delta}_e$, the fracture properties shown in Equations 38 and 39 are computed and used to update the traction vector, $\boldsymbol{t}$, and tangent modulus matrix, $\boldsymbol{C}$.

4.3. Model Verification

In this section, numerical simulation results using the newly-developed rate-dependent cohesive zone model are compared to analytical solutions of a simple problem. To check if the implementation is made correctly, a uniaxial bar problem was simulated. The bar was assumed to be elastic and a four-node cohesive zone element was placed in the middle of the bar between

two elements of bulk material. Table 2 summarizes the applied loads, geometry, and material properties of the uniaxial bar problems simulated for the verification of the rate-dependent fracture model.

Table 2. Applied loads, geometry, and material properties of the uniaxial bar problem used to verify the rate-dependent fracture model.

Material Properties				Dimensions (m)
Undamaged Properties		Fixed Cohesive Fracture Properties		1 x 2
Young's Modulus (Pa)	6.09E+10	Initial Stiffness (Pa/m)	500	
Poisson's Ratio	0.15	T_{max}^{ref} (Pa)	10	
		G_c^{ref} (J/m^2)	1	

Case	Rate-Dependent?	Rate-Dependent Fracture Properties			Loading Rate (m/sec)	
		β_T	β_G	$\dot{\delta}_e^{ref}$ (m/sec)	Ux_rate	Uy_rate
Figure 10c	No	0	0	-	0	0.1
Figure 10e					0.1	0
Figure 10g					0.1	0.3
Figure 11					0	0.1, 0.2
Figure 12	Yes	-0.05	-0.05	1		0.01, 0.1, 1
Figure 13a		-0.05, 0, 0.05	0			0.1
Figure 13b		0	-0.05, 0, 0.05			0.1
Figure 14a		-0.05, 0, 0.05	0	0.01		0.1
Figure 14b		0	-0.05, 0, 0.05			0.1

Figure 10c, 10e, and 10g show comparisons for simulations conducted under different fracture modes, *i.e.*, mode I, mode II, and mixed-mode, respectively. Figure 10a shows the initial configuration of the uniaxial bar, and Figure 10b, 10d, and 10f show the boundary conditions applied on the three simulations. As clearly seen in Figure 10c, 10e, and 10g, both numerical and analytical results were identical for all three fracture modes.

To obtain the results shown in Figure 10, β_T and β_G (see Equations 38 and 39) were set to 0 and the cohesive zone model became rate-independent, *i.e.*, $T_{max} = T_{max}^{ref}$ and $G_c = G_c^{ref}$. To demonstrate that rate-independence of the cohesive zone properties for the case where $\beta_T = \beta_G = 0$, the problem shown in Figure 10b was simulated one more time for a different value of applied strain rate, 0.05 ε/sec. Figure 11 shows the comparison of the results for both applied strain rates (0.05 and 0.10 ε/sec) and, as expected, no difference was observed in the results, since the fracture properties were not affected by the applied loading rate when $\beta_T = \beta_G = 0$.

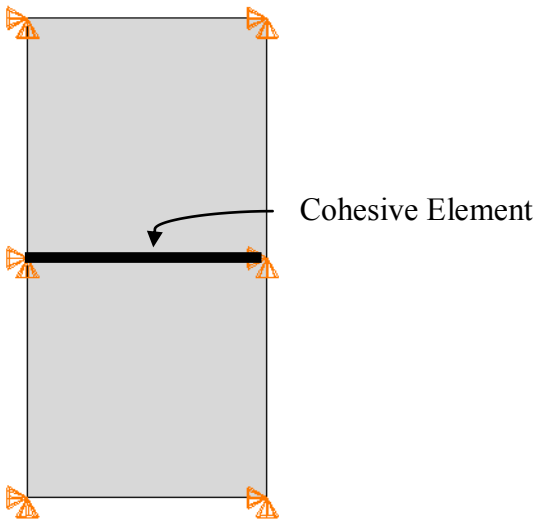

(a)

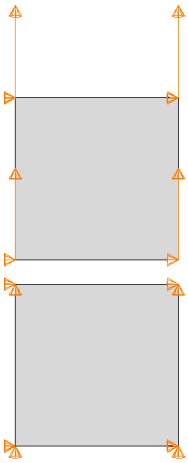

(b)

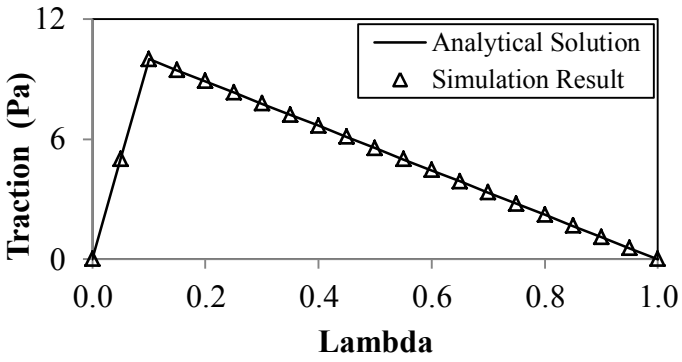
12
6
0
Traction (Pa)
0.0
0.2
0.4
0.6
0.8
1.0
Lambda
Analytical Solution
Simulation Result

(c)

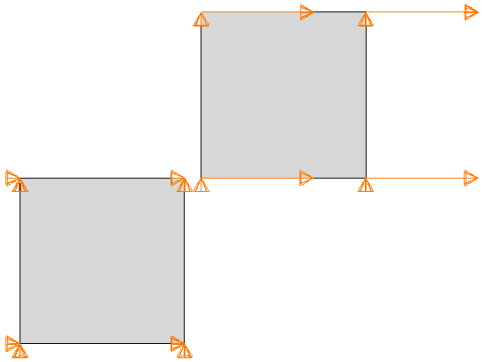

(d)

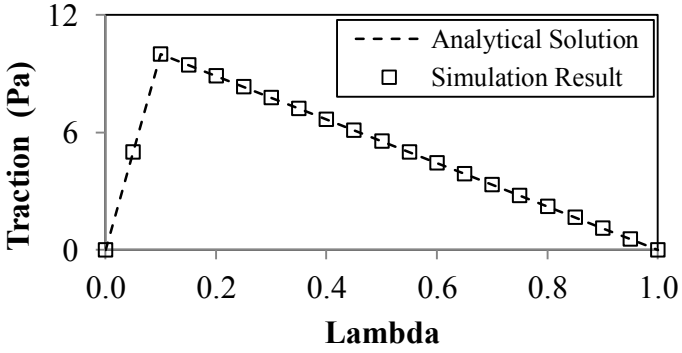
12
6
0
Traction (Pa)
0.0
0.2
0.4
0.6
0.8
1.0
Lambda
Analytical Solution
Simulation Result

(e)

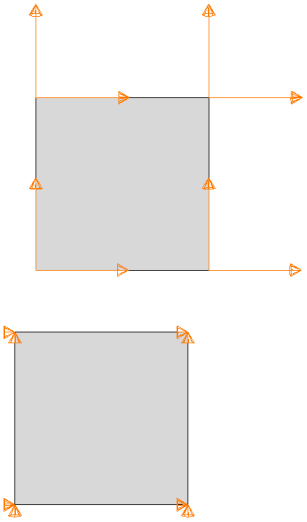

(f)

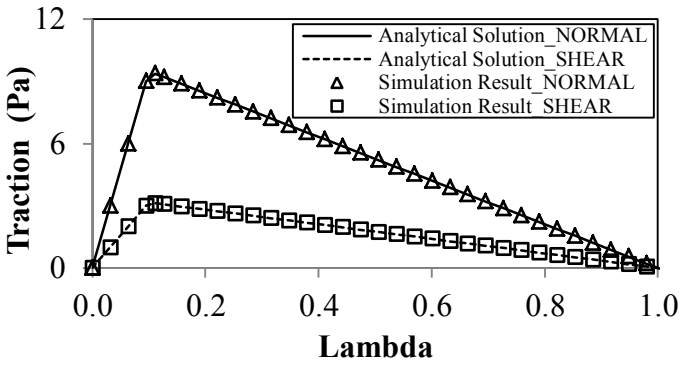

(g)

Figure 10. A uniaxial bar problem to check the accuracy of the UEL implementation for different fracture modes: (a) Initial configuration; (b), (d), and (f) Boundary conditions; and (c), (e), and (g) Comparisons with analytical solutions.

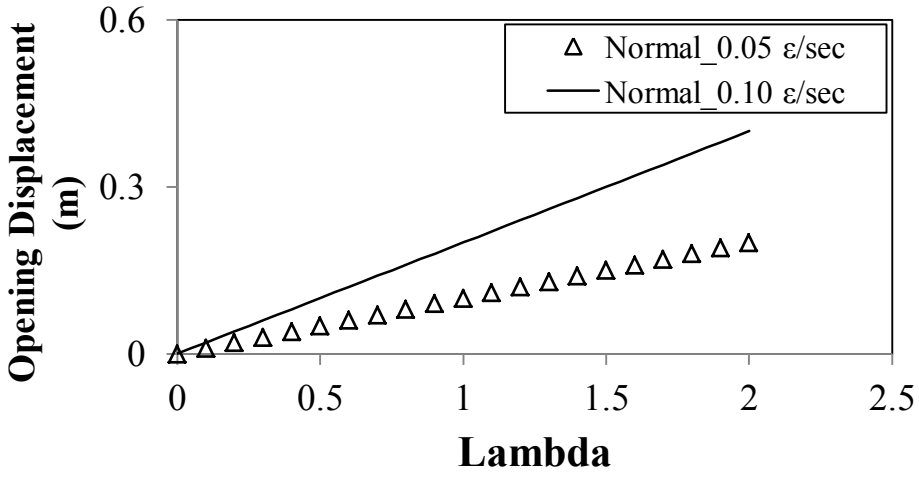

(a)

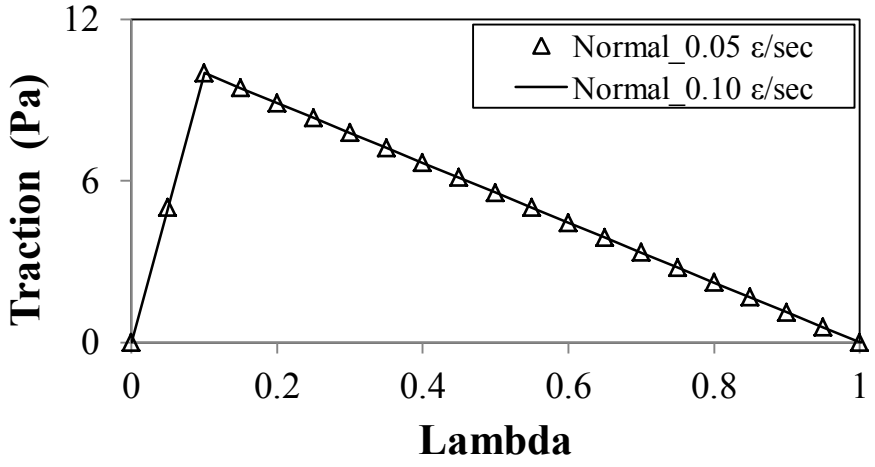

(b)

Figure 11. Rate-independent behavior for β_T and β_G = 0: (a) Two different applied strain rates, *i.e.*, 0.05 and 0.10 $\boldsymbol{\varepsilon}$ /sec; and (b) Identical mechanical responses to both applied rates.

Finally, to demonstrate the ability of the model to simulate rate-dependent fracture, new simulations were performed for $\dot{\delta}_e^{ref}$ = 1 m/sec and $\beta_T = \beta_G$ = - 0.05. Three different strain rates were applied to the uniaxial bar: 0.500, 0.050, and 0.005 ε/sec. Figure 12 shows that numerical and analytical results were identical for all three applied rates.

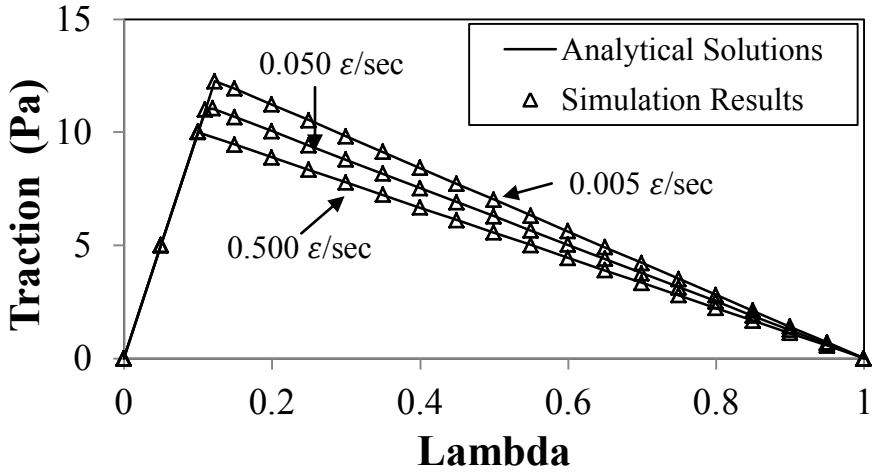

Figure 12. Rate-dependent behavior for β_T and β_G = -0.05 and three different applied strain rates, *i.e.*, 0.005, 0.050, and 0.500 ε/sec.

4.4. Sensitivity Analysis

Extra simulations were performed to illustrate how parameters β_T, β_G, and $\dot{\delta}_e^{ref}$ affected the rate-dependent model predictions. Figure 13a shows results for three different values of β_T (-0.05, 0, and 0.05) for β_G = 0. The results indicate that cohesive strength decreased (lower peak in the force-time curve) with the increase of β_T and that fracture energy was kept constant (for β_G = 0, $G_c = G_c^{ref}$) by adjusting the width of the curves. Figure 13b shows results for three different values of β_G (-0.05, 0, and 0.05) for β_T = 0. From the results, it is clear that the cohesive fracture energy decreased (narrower force-time curve) with the increase of β_G and that the cohesive strength was kept constant, as expected (for β_T = 0, $T_{max} = T_{max}^{ref}$).

The inversely proportional relation between cohesive fracture properties (T_{max} and G_c) and rate-dependent parameters (β_T and β_G) was due to the fact that the displacement rate experienced by the cohesive element, *i.e.*, $\dot{\delta}_e$ = 0.1 m/sec, was smaller than the assigned

reference displacement rate, *i.e.*, $\dot{\delta}_e^{ref}$ = 1 m/sec. In that case, the logarithmic terms of the expressions shown in Equations 38 and 39 became negative and resulted in fracture properties that were inversely proportional to the applied loading rates. As shown in Figure 14, T_{max} and G_c became proportional to β_T and β_G, respectively, when $\dot{\delta}_e > \dot{\delta}_e^{ref}$ (0.10 m/sec > 0.01 m/sec).

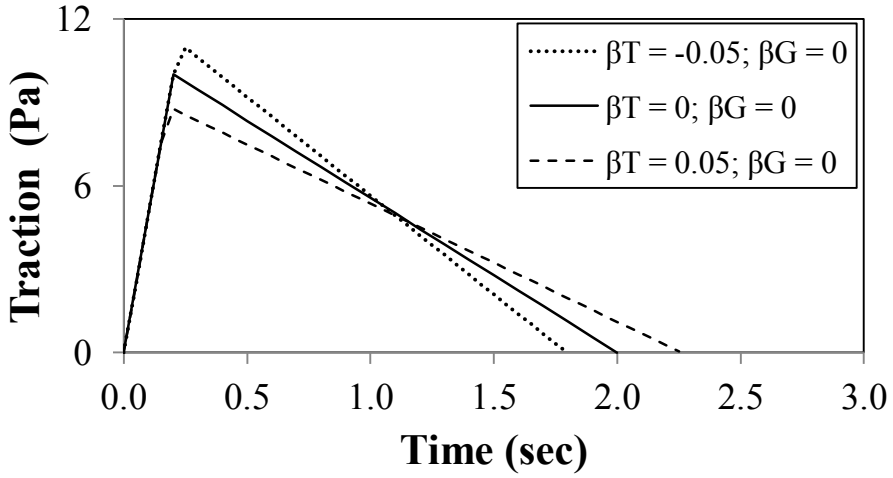

(a)

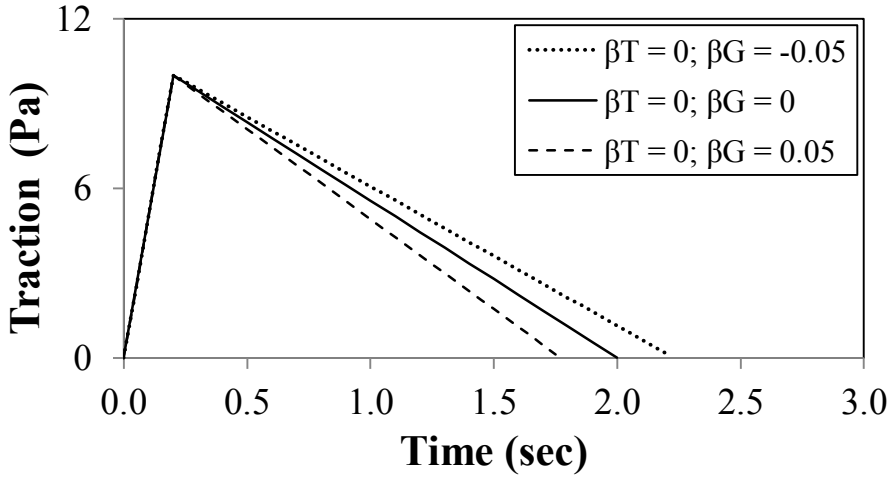

(b)

Figure 13. Rate-dependent fracture for $\dot{\delta}_e^{ref}$ = 1 and various: (a) β_T and (b) β_G.

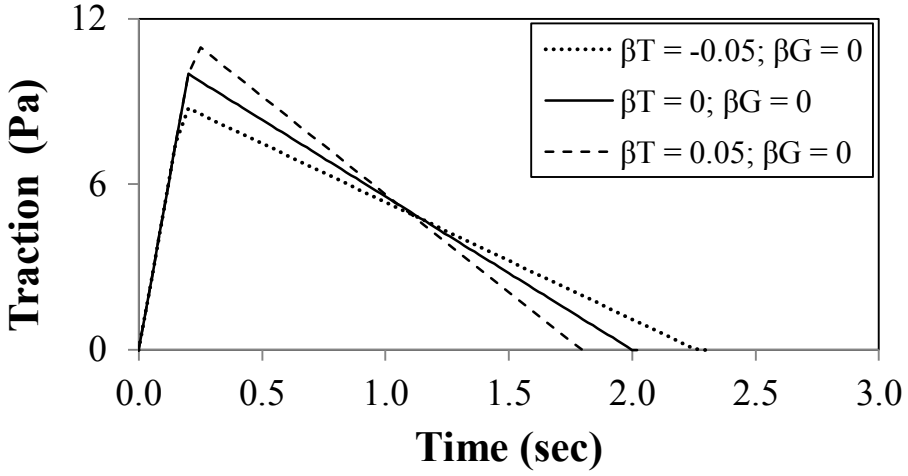

(a)

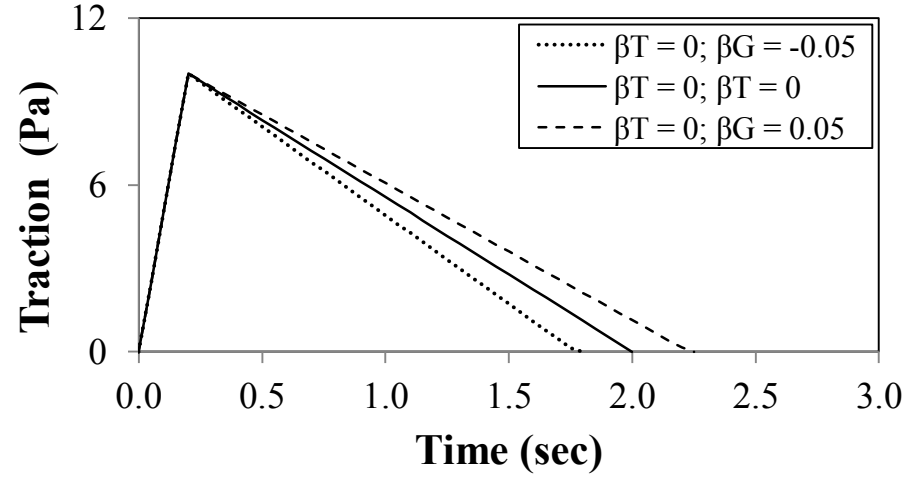

(b)

Figure 14. Rate-dependent fracture for $\dot{\delta}_e^{ref}$ = 0.01 and various: (a) β_T and (b) β_G.

Chapter 5

Experimental Program

This research considers the heterogeneous HMA mixtures as materials composed of two distinct phases (see Figure 15): isotropic linear elastic aggregate particles and isotropic linear viscoelastic FAM mixture (asphalt binder + fine aggregate particles + air voids). To model fracture damage in the mixtures, cohesive zone elements were inserted within the FAM phase. This assumption of fracture only within the FAM phase was based on the observation that HMA mixtures at intermediate service temperatures without moisture damage generally tend to crack through the FAM phase.

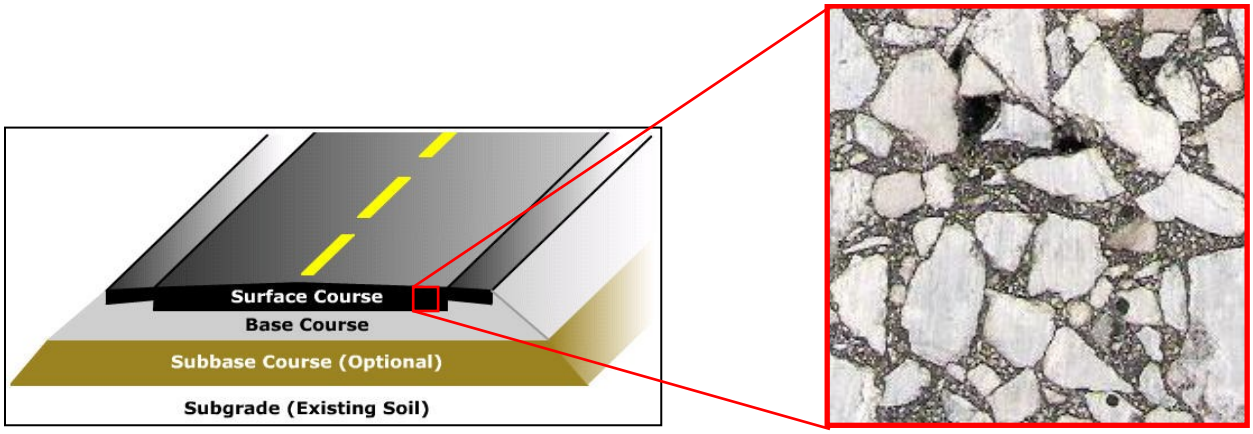

Figure 15. Illustration of the two distinct phases of asphalt mixtures considered in this research, *i.e.*, coarse aggregates (in gray) and FAM (in black).

The testing methodologies followed to characterize the material properties of the different mixture phases considered in the research are presented below. Following the property characterizations, this chapter also presents experimental testing results of dynamic modulus of

asphalt mixtures that were used in a later chapter for the validation of the computational microstructure model presented in this research.

5.1. Material Properties of Mixture Constituents

5.1.1. Linear Elastic Properties of Aggregate Particles

Young's modulus of aggregate particles was measured using a nano-indentation technique (Khanna *et al.*, 2003). The nano-nindentation tests were performed using a hard indenter with known mechanical properties and geometric characteristics. During the indentation process, the nano-indenter was pressed against the surface of the samples in multiple locations. Then, the load was held constant for a certain period of time and removed afterwards. The depth of penetration, h, was recorded and the area of indentation was determined using the known geometry of the indenter tip. Load and depth of penetration during the test were plotted on a graph to create a load-displacement curve (Figure 16b). From the unloading part of that curve, the contact stiffness, S (Equation 42), was calculated and used to estimate the modulus of elasticity of the aggregate samples, E_a, using Equation 41. Figure 16a illustrates the indentation process. More details about the indentation process can be found in Karki (2010).

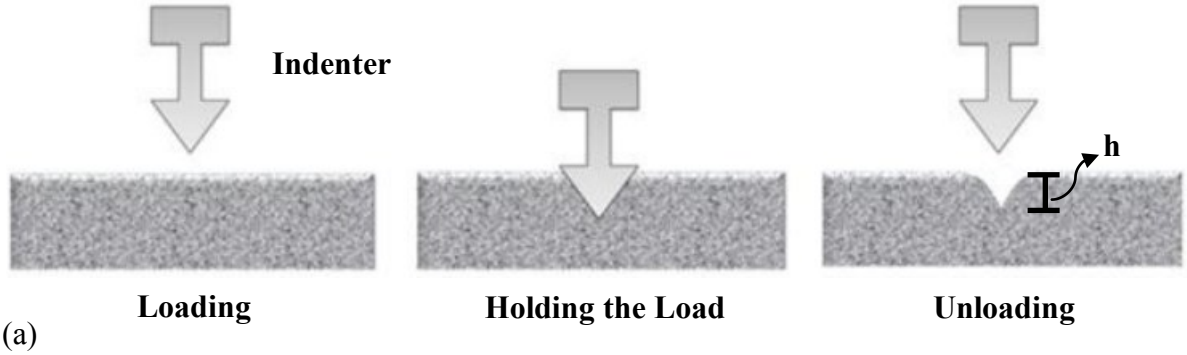

(a)

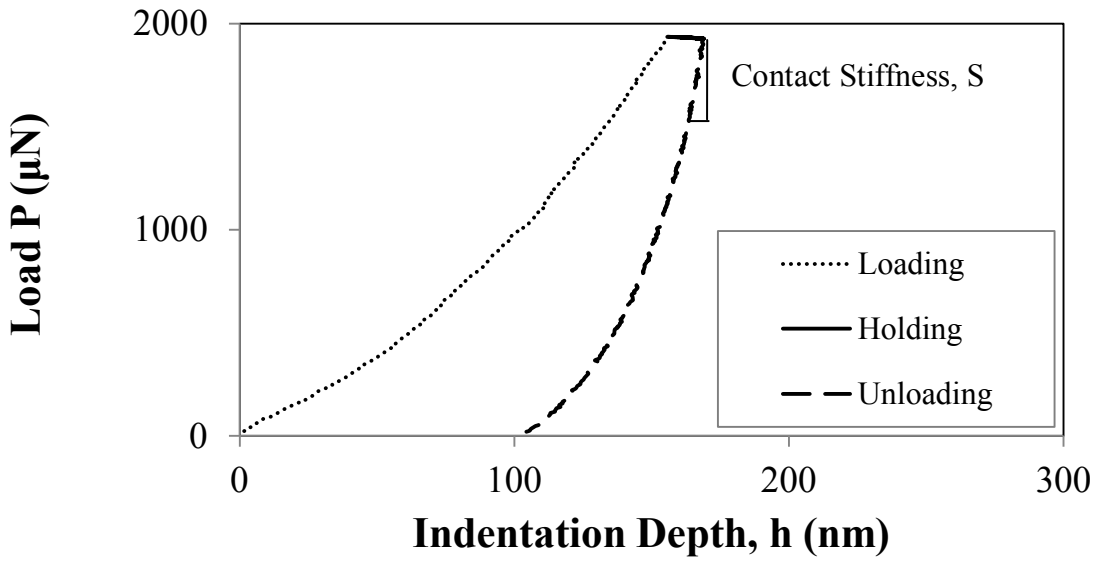

(b)

Figure 16. An illustration of the nano-indentation test: (a) Indentation process consisting of loading, holding and unloading steps; and (b) An example of a plot of load-depth of penetration used to determine sample stiffness.

Several assumptions were made related to the nano-indentation technique, including: (1) purely elastic deformation upon unloading; (2) determination of the reduced compliance by combining the compliance of the aggregate specimen and of the indenter tip in a model with springs in series, as shown in Equation 41; and (3) determination of the contact stiffness by using Equation 42.

$$\frac{1}{E_r} = \frac{1-\nu_i^2}{E_i} + \frac{1-\nu_a^2}{E_a} \tag{41}$$

$$S = 2\sqrt{\frac{A}{\pi}}E_r \tag{42}$$

where S, A, E_r, E_i, E_a, ν_i and ν_a = contact stiffness, contact area, reduced modulus, indenter modulus (1,141 GPa in this study), elastic modulus of aggregates, Poisson's ratio of the indenter (0.07 in this study), and Poisson's ratio of aggregates. The contact stiffness was obtained by taking the slope of the experimentally measured stiffness of the upper portion of the unloading data (Oliver and Pharr, 1992). As shown in Figure 17, 20 measurements were made resulting in a mean E_a of 60.9 GPa and a standard deviation of approximately 11 GPa. Poisson's ratio (ν_a) was assumed to be equal to 0.15 (Barksdale, 1993).

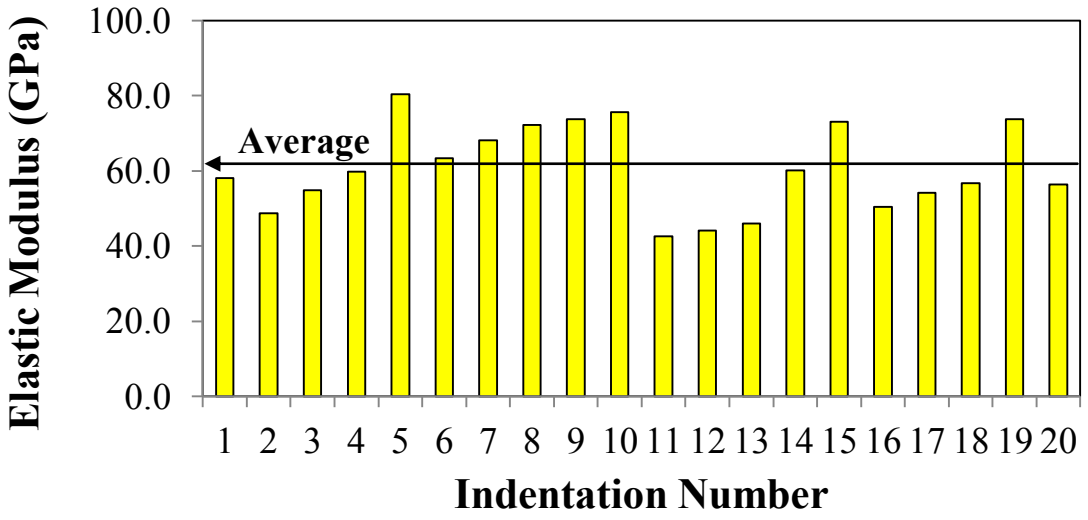

Figure 17. Nano-indention results of Young's modulus for aggregate particles (Karki, 2010).

5.1.2. Linear Viscoelastic Properties of FAM Mixture

The mixture used in this study was a FAM consisting of a PG 64-28 binder (13.3%) and fine aggregates (limestone and gravel) smaller than 0.6 mm and hydrated lime (1.5% of total mass of aggregates). Table 3 shows the FAM mixture gradation and Table 4 summarizes physical properties of materials and volumetric parameters of the mixture. The FAM mix design was

developed based on the volumetric mix design of its HMA mixture containing 4% of air voids (Karki, 2010). The binder content used in the design of the FAM mixture corresponded to the total amount of binder used in the HMA mixture minus the amount of binder that is absorbed into surface voids of aggregates larger than 0.6 mm and that covers those aggregates in thin films of 12 μm. The selection of the FAM mixture for this study was based on several rationales, such as (a) it being well known that HMA mixtures at intermediate service temperatures without moisture damage tend to crack through the matrix phase, (b) testing repeatability of the FAM mixture is likely to be higher than that of highly heterogeneous HMA mixtures, and (c) testing results from the FAM mixtures can be directly applied to computational microstructure models that simulate the damage-related performance of HMA mixtures by accounting for the individual component properties and microstructural heterogeneity of the mixtures.

Table 3. FAM mixture gradation.

Material	Sieve (% retained)			
	#50	#100	#200	-200
Screenings (limestone)	8.6%	7.9%	-	12.5%
3ACR (gravel)	11.4%	4.3%	25.0%	12.5%
47B (gravel)	8.6%	9.2%	-	-

Table 4. Physical properties of materials and volumetric parameters of the FAM mixture

Hydrated Lime	
Specific Gravity	2.343
Dry Brightness, G.E.	92
Median Particle Size - Sedigraph	2 micron
pH	12.4
BET Surface Area	22 m^2/g
-100 Mesh (150 µm)	100.0%
-200 Mesh (75 µm)	99.0%
-325 Mesh (45 µm)	94.0%
Apparent Dry Bulk Density - Loose	22lbs./ft^3
Apparent Dry Bulk Density - Packed	35lbs./ft^3

Fine Aggregates			
Aggregate	**G_{sb}**	**Absorption Capacity (%)**	**FAA (%)**
Screenings (limestone)	2.478	3.66	46.7
3ACR (gravel)	2.556	1.13	43.7
47B (gravel)	2.605	0.49	37.3

PG 64-28 Binder			
Test	**Temperature (°C)**	**Test Result**	**Required Value**
Unaged DSR, G*/sinδ (kPa)	64	1.21	Min. 1.00
RTFO - Aged DSR, G*/sinδ (kPa)	64	3.01	Min. 2.20
PAV - Aged DSR, G*sinδ (kPa)	19	2,112	Max. 5,000
PAV - Aged BBR, Stiffness(MPa)	-18	181	Max. 300
PAV - Aged BBR, m-value	-18	0.32	Min. 0.30

FAM Mixture	
Density (kg/m^3)	2206.03
Asphalt Content (%)	13.3

Dynamic frequency sweep tests were conducted to identify linear viscoelastic material properties of the FAM phase. The PG 64-28 asphalt binder was blended with only fine aggregate particles (29% of limestone and 71% of gravel) smaller than 0.6 mm to create cylindrical FAM specimens of 50 mm in length and 12 mm in diameter. The process to fabricate these testing samples included several steps. First, aggregate particles were sieved. To remove the excessive amount of dust adhering to finer particles, one of the aggregates (fine limestone) had to be washed after the sieving step. Fine aggregates and asphalt binder were proportioned following a mix design procedure described by Karki (2010). Aggregates and binder were pre-heated to the mixing temperature of 146^{o}C and mixed at 135 ^{o}C. A sample (80 mm in height and 150 mm in diameter) was compacted with a Superpave gyratory compactor (SGC) that applied a compaction pressure of 600 kPa at a speed of 30 gyrations per minute. The bulk specimens were sliced with a diamond saw machine and the top and bottom slices (15-mm-thick slices) were discarded. The testing specimens (50 mm in length and 12 mm in diameter) were cored out of the middle slice of the SGC sample. Figure 18 illustrates the several steps for the fabrication of the FAM samples.

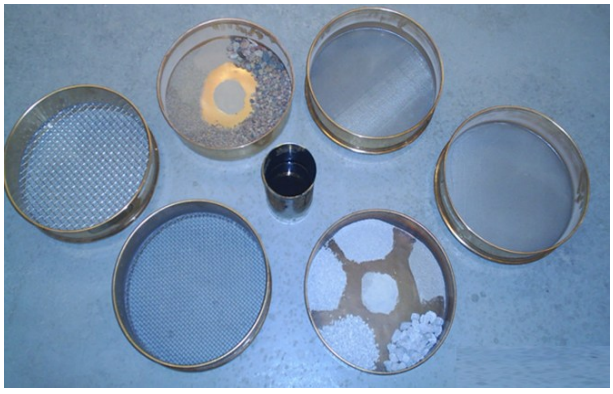

(a)

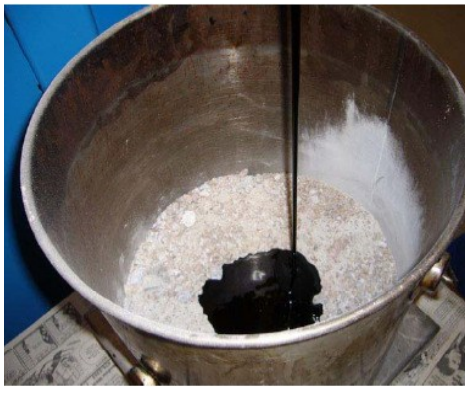

(b)

(c)

(d)

(e)

(f)

Figure 18. FAM sample fabrication process: (a) Aggregate sieving; (b) Mixing aggregates and binder; (c) Compacting a sample with a SGC compactor; (d) Sliced SGC sample; (e) Coring testing samples out of the middle section of the SGC sample; and (f) Testing sample.

The specimens were then tested in a rheometer (see Figure 20) by applying a low torsional sinusoidal strain of 0.0065%, which is a level of strain within the linear viscoelastic range, with varying frequencies (0.01 to 25 Hz) at several different temperatures (5^{o}C, 20^{o}C, and 40^{o}C). Considering the FAM phase as a thermorheologically simple material, the well-known frequency (or time) - temperature superposition principle was employed to obtain the linear

viscoelastic master curves of the storage modulus in the frequency domain for a reference temperature of 20°C. Then, the whole master curve was slightly shifted to the reference temperature of 21°C. Figure 19 illustrates the process of master curve generation.

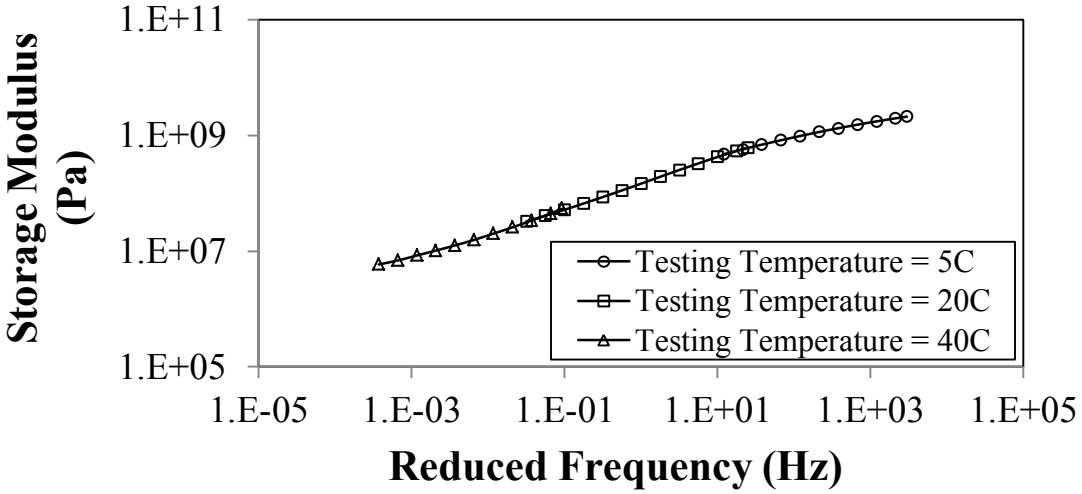

(a)

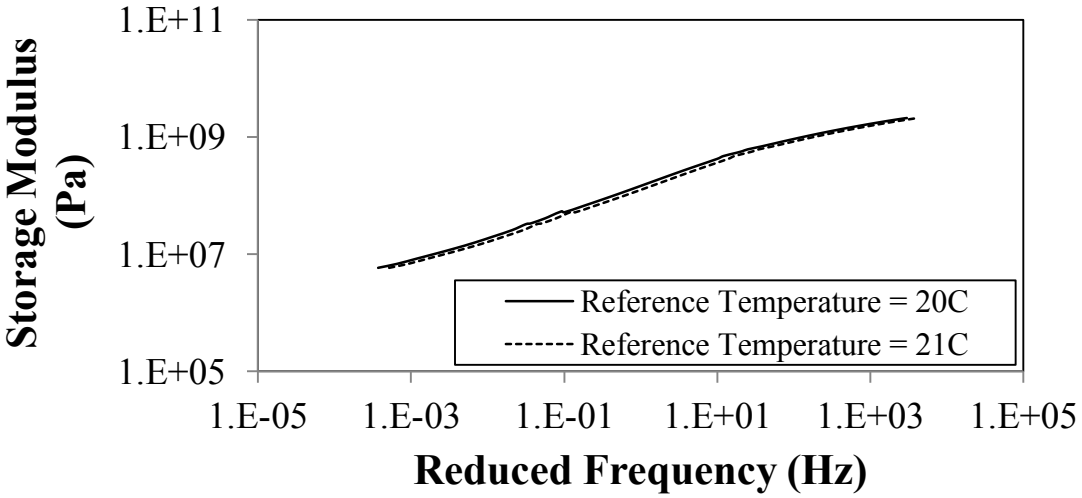

(b)

Figure 19. Test results of storage modulus for three testing temperatures - master curve at a reference temperature of: (a) 20°C; and (b) 21°C.

Using the procedure described in other studies (Kim *et al.* 2003, 2005, 2006a, 2006b), the Prony series parameters in the storage modulus were used to define time-domain shear relaxation modulus. Poisson's ratio of 0.35 was assumed. Table 5 shows the linear viscoelastic properties obtained for the FAM used in this study, *i.e.*, spring constants and relaxation time in the generalized Maxwell model, E_i and ρ_i, respectively.

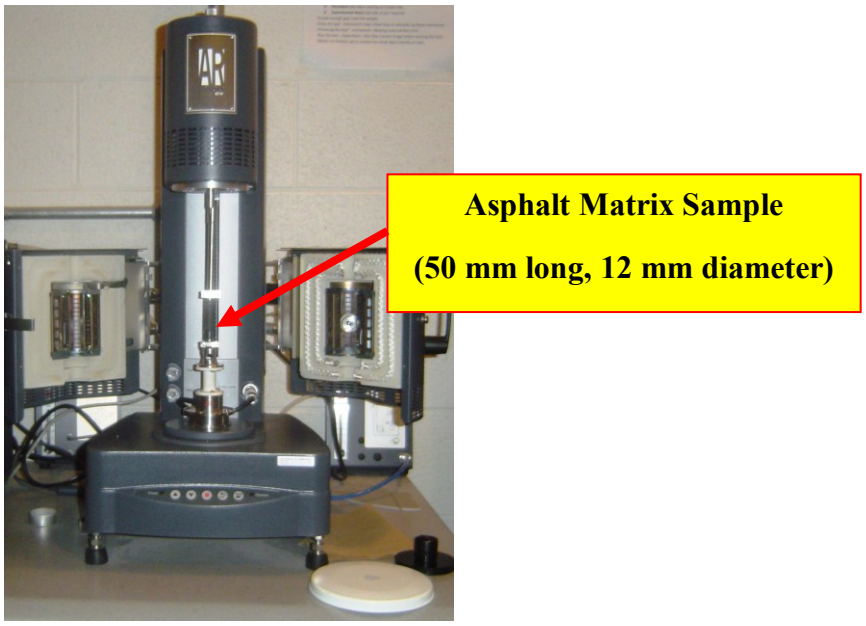

Figure 20. Inside view of the rheometer used to obtain linear viscoelastic properties of FAM samples.

Table 5. Prony series coefficients of the matrix phase at 21°C

i	E_i (MPa)	ρ_i (sec)
1	3026.1	8.0E-05
2	1484.1	8.0E-04
3	1333.6	8.0E-03
4	435.0	8.0E-02
5	159.6	8.0E-01
6	50.0	8.0E+00
7	17.9	8.0E+01
8	3.0	8.0E+02
∞	12.2	-

5.2. Fracture Properties of FAM mixtures

The convenient SCB geometry was selected for fracture testing. Originally developed to characterize the fracture behavior of rocks based on the concepts of Linear Elastic Fracture Mechanics (LEFM) (Chong and Kuruppu, 1984; Lim *et al.*, 1994; Adamson *et al.*, 1996), since the 1990s the SCB testing configuration has become a popular geometry for evaluating the fracture behavior of asphalt mixtures (Molenaar *et al.*, 2002; van Rooijen and de Bondt, 2008; Li and Marasteanu, 2010) and was chosen for this study among other available geometries due to several benefits. The SCB testing is practically attractive - even if it has some limitations, such as the existence of an arching effect (Wagoner *et al.*, 2005b) - in that it is very simple to perform, and multiple testing specimens can be easily prepared via a routine process of mixing and Superpave gyratory compacting of asphalt mixtures. Furthermore, the SCB geometry is even more attractive considering the fracture characteristics of field cores.

SCB specimens were fabricated by slicing SGC samples and introducing a mechanical notch 2.5 mm wide and 25 mm deep, as shown in Figure 21. Before testing, individual SCB specimens were placed inside the environmental chamber of a mechanical testing machine for

temperature equilibrium targeting the reference temperature of 21°C. Following the temperature-conditioning step, various monotonic displacement rates were applied to the top centerline of the SCB specimens. Metallic rollers separated by a distance of 122 mm (14 mm from the edges of the specimen) were used to support the specimen. Reaction force at the loading application line was monitored by the data acquisition system of the mechanical testing machine. Opening displacements at the mouth and at the tip of the initial notch were also monitored with high-speed cameras and a digital image correlation (DIC) system. Figure 22 shows the SCB testing set-up incorporating the high speed cameras and the DIC system.

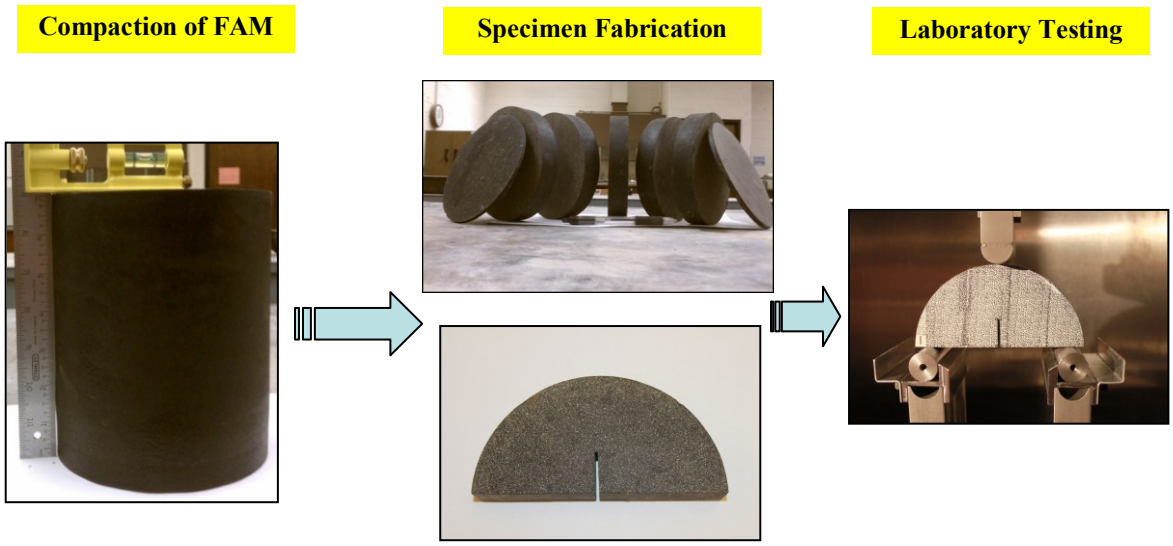

Figure 21. FAM specimen fabrication and laboratory fracture test.

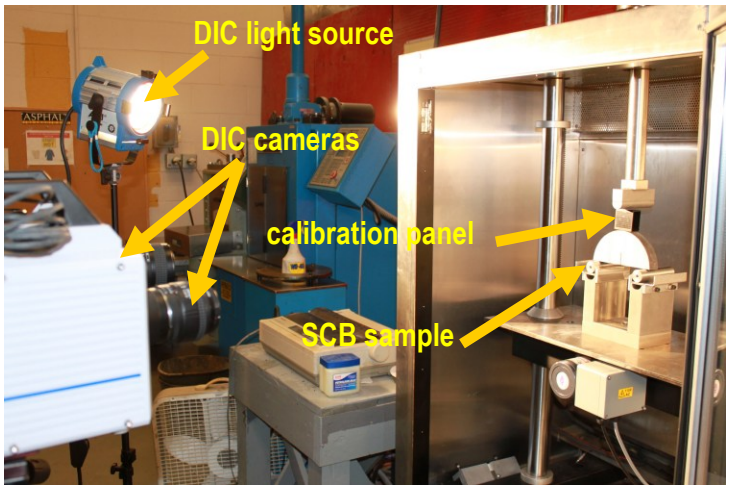

(a)

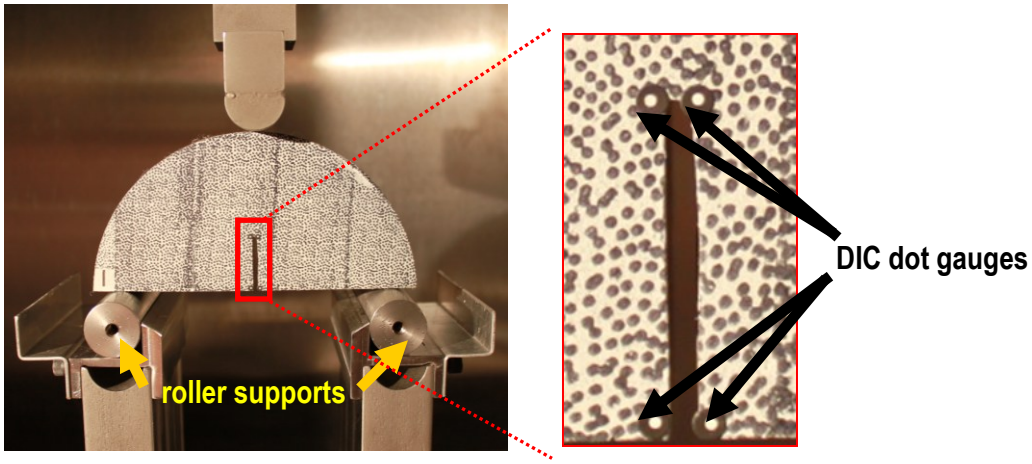

(b)

Figure 22. Experimental testing set-up: (a) An overview of the whole testing set-up; and (b) A closer view of a SCB specimen ready to be tested.

Concerning the fracture testing of SCB specimens subjected to constant displacement rates, the first step in developing the testing protocol was to determine a proper specimen thickness. This was motivated by the fact that expensive three-dimensional simulations can be closely approximated by two-dimensional simulations (such as a plane stress condition) if the specimen is thin enough to be subject to the plane stress fracture condition. Thin specimens are

subject to plane stress loading at the crack tip, while thick specimens experience crack-tip triaxiality in the interior of the section. The stress state in the central region is essentially plane strain at distances from the crack tip that are small compared to the plate thickness. Near the free surface, the stress triaxiality is lower, but a state of pure plane stress exists only at the free surface. Based on this fact, three specimen thicknesses (25, 38, and 50 mm) were attempted for two different loading rates (50 mm/min and 100 mm/min), and test results were compared.

Test results (in the form of force - loading time plots) from the three thicknesses at the two different loading rates generally demonstrated that 38 mm-thick specimens produced results that closely approximate those for the 25 mm-thick specimens by taking a ratio between two specimen thicknesses (*i.e.*, 25/38). The same trend was not observed from the 50 mm-thick specimens with a thickness ratio of 0.50 (25/50). Test results indicated that two-dimensional simulations can be performed with test results of SCB specimens less than 38 mm thick when such simulations assume the plane stress condition. A similar finding was also reported in a study by Li and Marasteanu (2004), in which simulations of the SCB test demonstrated the existence of stresses in the out-of-plane direction for specimens with a thickness of 50 mm. Negligible out-of-plane stresses were observed from 25 mm-thick specimens. Based on the test results herein and the similar finding by Li and Marasteanu (2004), the fracture tests of the FAM mixture were conducted with 25 mm-thick SCB specimens.

A total of eighteen, 25 mm-thick SCB specimens were then fabricated to investigate fracture characteristics of the FAM mixture within a wide range of loading rates. Nine different rates (1, 5, 10, 25, 50, 100, 200, 400, and 600 mm/min) were attempted in this study. For each loading rate, two replicates were tested at 21^{o}C. Testing was highly repeatable without large discrepancies observed among the replicates. Figure 23 presents the SCB test results (two

replicates per loading rate) by plotting the reaction forces at the point of load application as the loading time increased. Due to the significantly different testing times necessary to complete at different individual rates, test results were plotted separately in three figures: Figure 23a shows results for loading rates 1, 5, and 10 mm/min; Figure 23b shows results for loading rates 25, 50, and 100 mm/min; and Figure 23c shows results for loading rates 200, 400, and 600 mm/min. Figure 24 shows averaged SCB test results of reaction force as a function of CTOD and CMOD (Figure 24a and Figure 24b, respectively) and reveals similar levels of critical displacements for all the rates, but an increase in the peak load as the loading rate increases. Clearly, the figures reveal the rate-dependent global mechanical behavior of the FAM mixture.

The rate-dependent mechanical response is related to several effects, such as the viscoelasticity of the FAM and the fracture characteristics throughout the fracture process zone (or cohesive zone). As noted earlier, test results are incorporated with numerical simulations that account for both material viscoelasticity and cohesive zone fracture process. This is done to separately identify the sources of rate dependency so as to better determine if the rate-dependent mechanical response is related to the fracture process. Cohesive zone fracture parameters determined through this experimental-numerical integrated approach can provide the rate-related fracture characteristics of the mixtures.

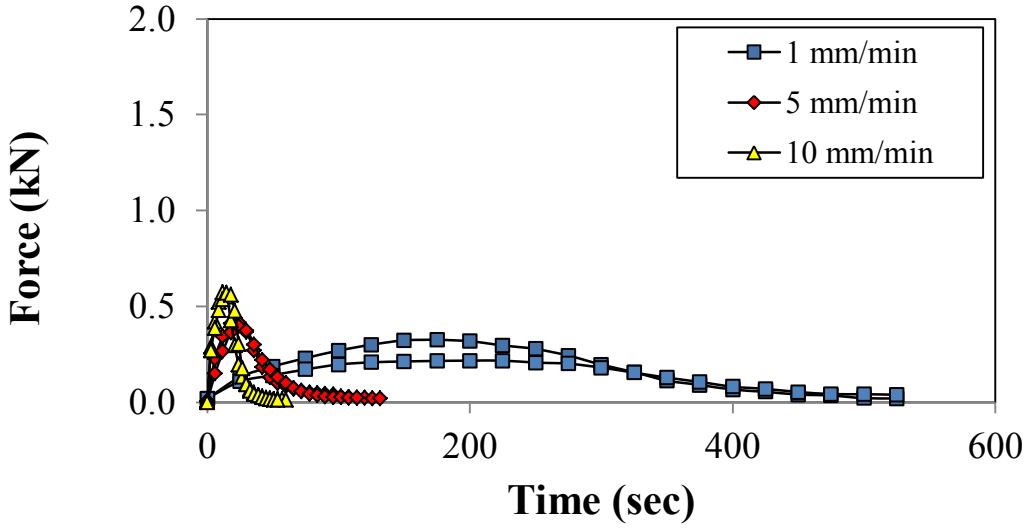
2.0
1.5
1.0
0.5
0.0
Force (kN)
0
200
400
600
Time (sec)
1 mm/min
5 mm/min
10 mm/min

(a)

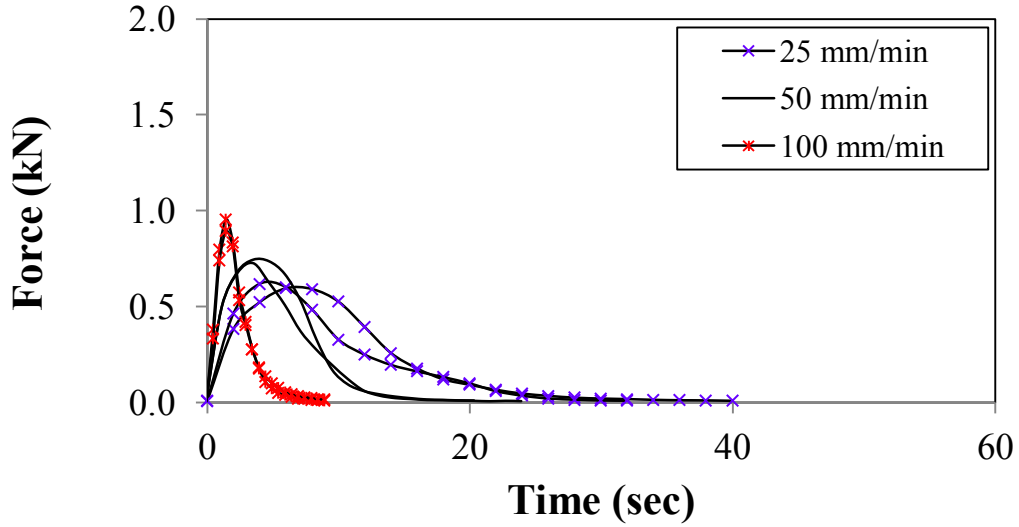
2.0
1.5
1.0
0.5
0.0
Force (kN)
0
20
40
60
Time (sec)
25 mm/min
50 mm/min
100 mm/min

(b)

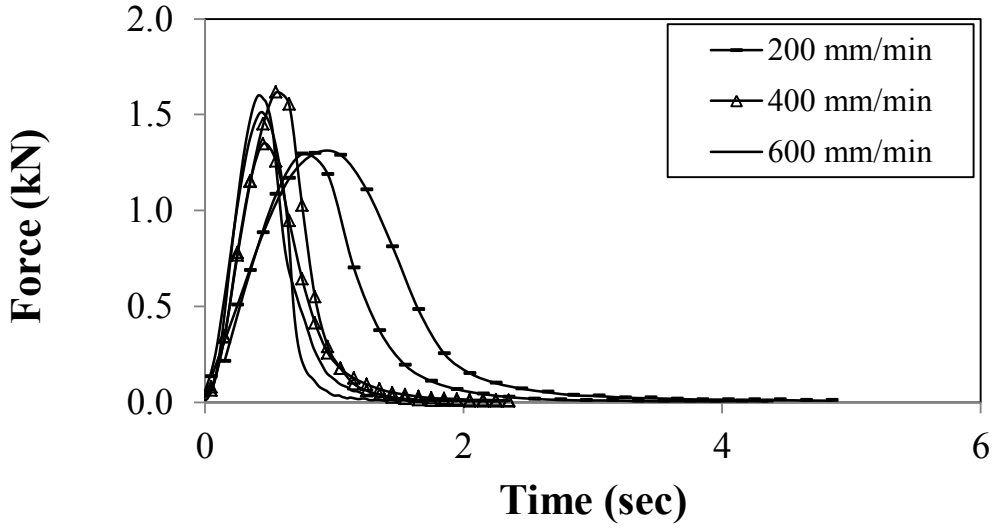

(c)

Figure 23. SCB test results of force-time at the nine different loading rates: (a) 1, 5, and 10 mm/min; and (b) 25, 50, and 100 mm/min; and (c) 200, 400, and 600 mm/min.

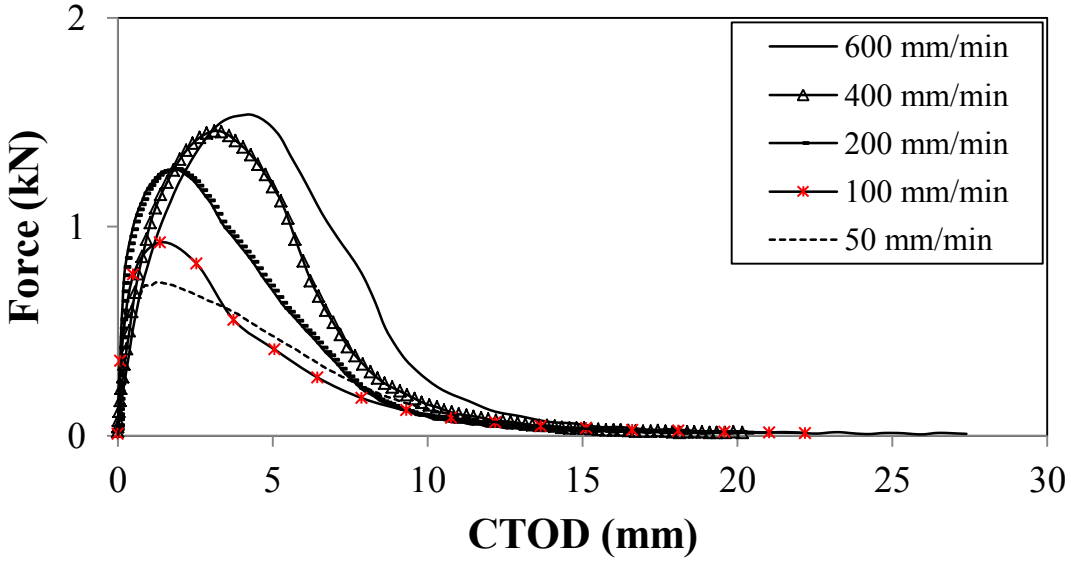

(a)

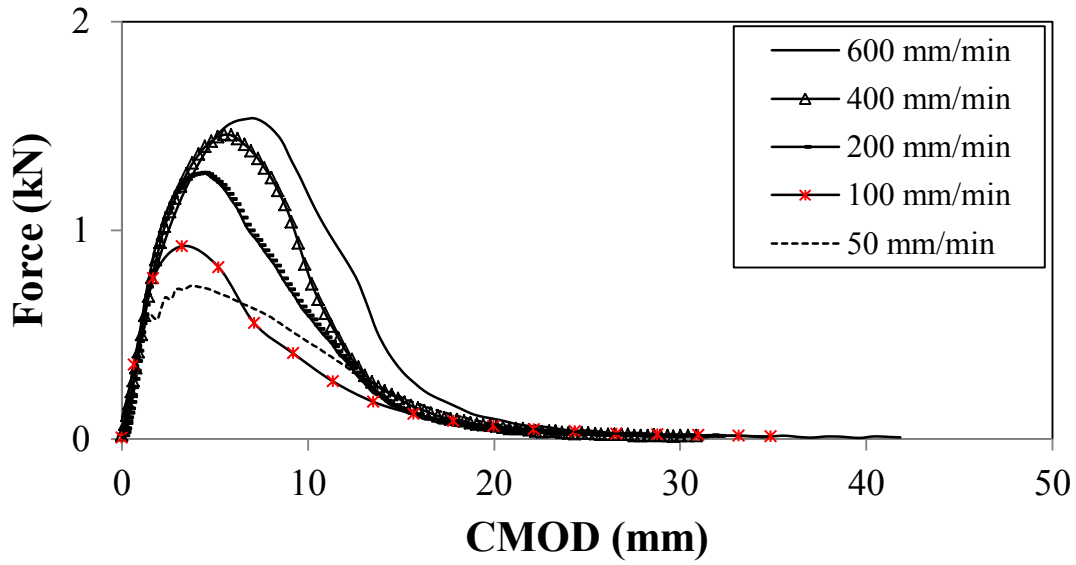

(b)

Figure 24. SCB test results for four different loading rates, *i.e.*, 100, 200, 400, and 600 mm/min: (a) Force-CTOD; and (b) Force-CMOD.

5.3. Laboratory Tests with HMA Mixtures

5.3.1. Dynamic Modulus

Dynamic modulus tests were performed on cylindrical asphalt concrete specimens in the uniaxial testing mode (see Figure 25). Table 6 shows the proportions of the different aggregates used in the gradation of the asphalt concrete mixture. PG 64-28 binder (5.5%) and hydrated lime (1.5%) were also added to the mixture. Table 6 also shows volumetric characteristics of the mixture, which were within the limits specified by the Nebraska Department of Roads for a SP4 Special mixture.

Table 6. Asphalt concrete mixture gradation and volumetric properties.

Material	Sieve (% retained)									
	1/2"	3/8"	#4	#8	#16	#30	#50	#100	#200	-200
5/8" LS (limestone)	5.0%	5.4%	-	-	-	-	-	-	-	-
2A (gravel)	-	0.6%	2.6%	-	-	-	-	-	-	-
Screenings (limestone)	-	-	-	14.0%	15.0%	4.2%	1.2%	1.1%	-	1.8%
47B (gravel)	-	-	-	4.0%	-	0.7%	1.2%	1.3%	-	-
3ACR (gravel)	-	-	6.8%	18.0%	-	2.1%	1.6%	0.6%	3.5%	1.8%
1/4" LS (limestone)	-	-	7.7%	-	-	-	-	-	-	-

Property	NDOR Limits	Test Result
Gmm	-	2.431
Gsb	-	2.577
Gmb	-	2.336
%Va	4 ± 1	3.9
%VMA	> 14	14.3
%VFA	65 - 78	72.7
%Pb	-	5.5
D/B	0.7-1.7	1.4

The sample fabrication process was similar to that described above to obtain cylindrical samples of the FAM mixture. The SGC samples (170 mm in height and 150 mm in diameter) of the HMA mixture used in the study were cored with a coring machine and sliced with a diamond saw machine and the top and bottom slices (10-mm-thick slices) were discarded. To measure the displacement of gauge points glued to the specimens, three linear variable differential transformers (LVDTs) were mounted onto the surface of the specimen at 120^{o} radial intervals with a 100-mm gauge length. To reach the specified testing temperatures, the specimens were placed inside the environmental chamber of the universal testing machine used in the research. Steel disks were placed on the top and bottom faces of the specimens for the application of a uniformly distributed load to the specimens. The loading levels were carefully adjusted until the

strain levels were within the range of 50 - 75 $\mu\varepsilon$. Vertical deformations averaged from the three LVDTs were used to calculate the dynamic modulus, defined simply as the ratio of the sinusoidal stress amplitude to the sinusoidal strain amplitude. As suggested in AASHTO TP 62-03, five temperatures (-10.0, 4.4, 21.0, 37.8, and 54.4 ^{o}C) and six loading frequencies (25.0, 10.0, 5.0, 1.0, 0.5, and 0.1 Hz) were used. The frequency-temperature superposition concept was applied in order to develop a master curve representing the dynamic modulus of the HMA mixture, as shown in Figure 26.

Figure 25. HMA specimen fabrication and laboratory test of dynamic modulus.

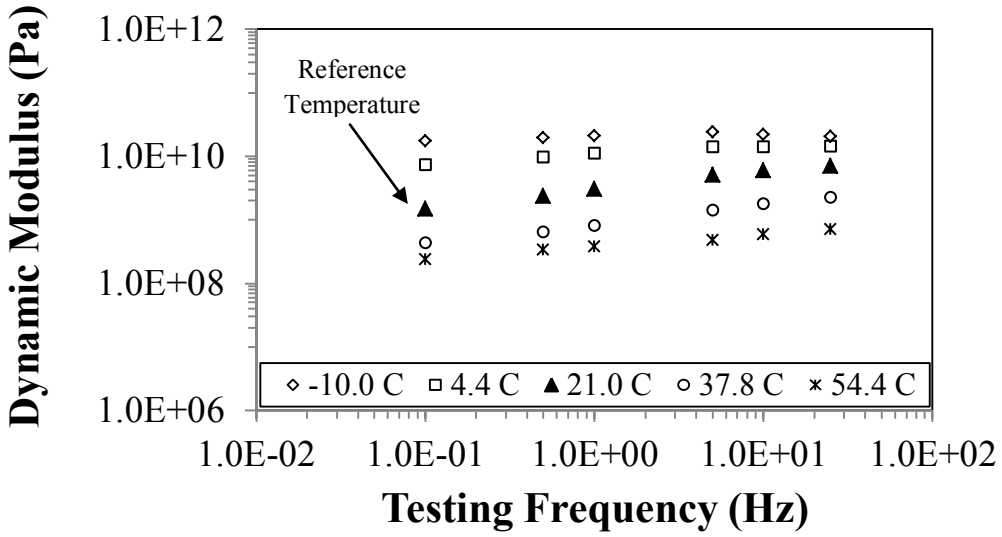

(a)

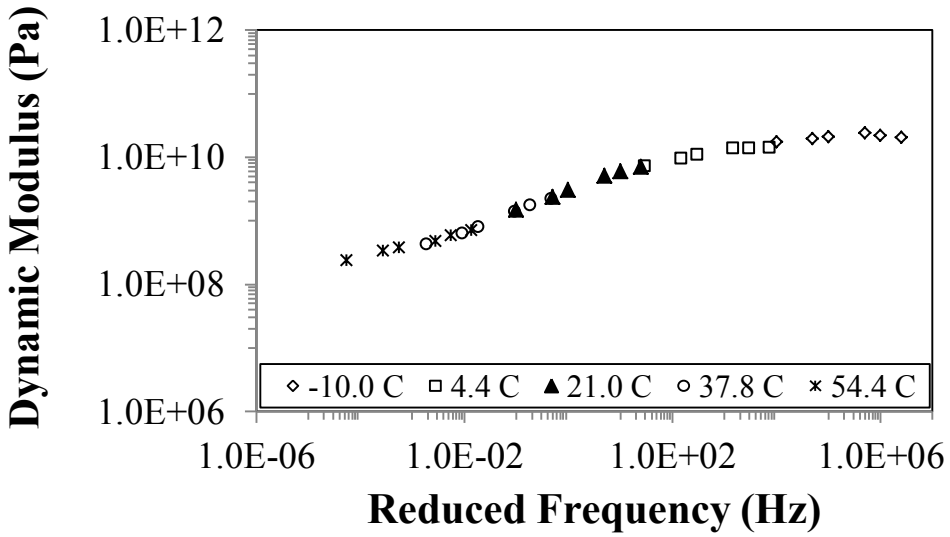

(b)

Figure 26. Dynamic modulus of the HMA mixture: (a) Testing results for each temperature; and (b) Master curve for a reference temperature of 21.0 ^{o}C.

Chapter 6

Characterization of Cohesive Zone Fracture Process

The viscoelastic nature of the asphaltic FAM phase creates a complication in identifying cohesive zone fracture properties. Part of the energy monitored by calculating the area below the experimental force-displacement (or loading time) curves is related to the energy dissipated due to the viscoelastic behavior of the FAM. Thus, fracture parameters along the fracture process zone should be identified locally, not by the global force-displacement results (Song *et al.*, 2008). Based on this fact, numerical simulations of the SCB tests were first conducted with the rate-independent bilinear cohesive zone model to determine the cohesive zone fracture parameters required to initiate and propagate cracks through the specimens. The results demonstrated the rate-dependence of the cohesive fracture properties. To account for that rate-dependence in the FAM phase, further modeling of the SCB tests was performed using the newly developed rate-dependent cohesive zone model to calibrate the rate-dependent model parameters for cohesive strength and fracture energy. The calibrated model parameters were used as inputs for the simulation of more general structures (*e.g.*, heterogeneous HMA samples), as shown in the next chapter. All simulations were performed assuming a plane stress two-dimensional approximation.

6.1. FEM Modeling of SCB Fracture Test

A convergence study was first conducted to identify the appropriate size of cohesive elements to model the SCB fracture testing of the FAM specimens. Four different element sizes, *i.e.*, 0.5, 1.0, 2.0, and 5.0 mm were investigated. Figure 27 shows the four meshes generated for this study and Figure 28, the corresponding simulation results in the form of force-time graphics. Even though no major differences were observed, it appears that the simulation result was convergent for a cohesive element size smaller than 2.0 mm. Thus, an element size of 1.0 mm was chosen for the remaining simulations of the SCB tests.

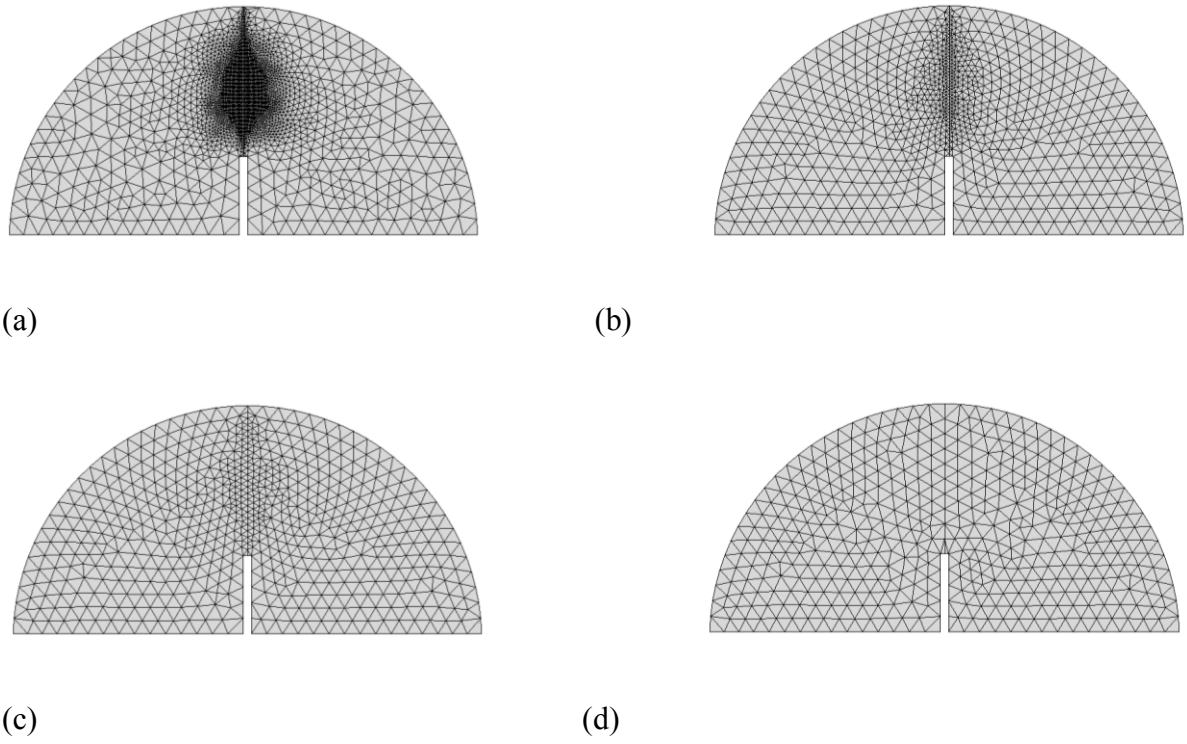

(a) (b)

(c) (d)

Figure 27. Mesh convergence study for four cohesive element sizes: (a) 0.5 mm; (b) 1.0 mm; (c) 2.0 mm; and (d) 5.0 mm.

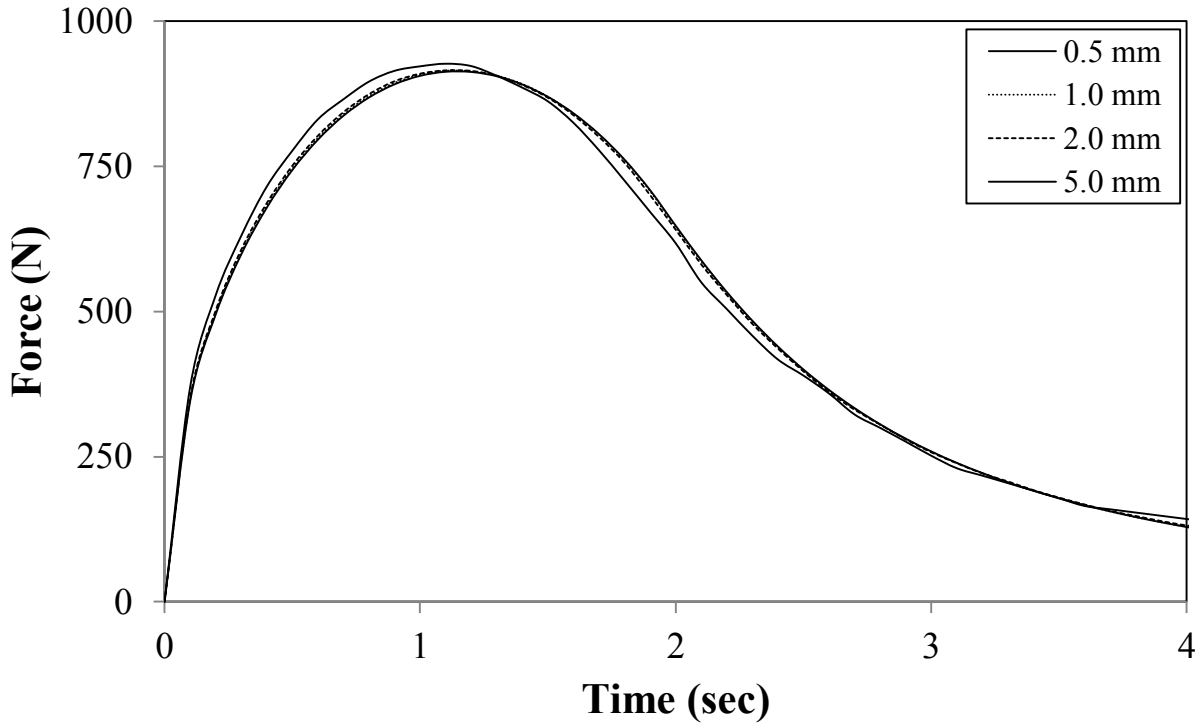

Figure 28. Mesh convergence study - simulation results.

Figure 29 presents the selected mesh and its corresponding boundary conditions used to model the SCB fracture testing of the FAM specimens. As shown, the mesh contains cohesive zone elements along the centerline of the virtual SCB specimen. The Prony series parameters obtained from the linear viscoelastic dynamic frequency sweep tests were used for the viscoelastic matrix elements, and the bilinear cohesive zone model illustrated in a previous chapter was used to simulate fracture in the middle of the matrix specimen as the opening displacements increased.

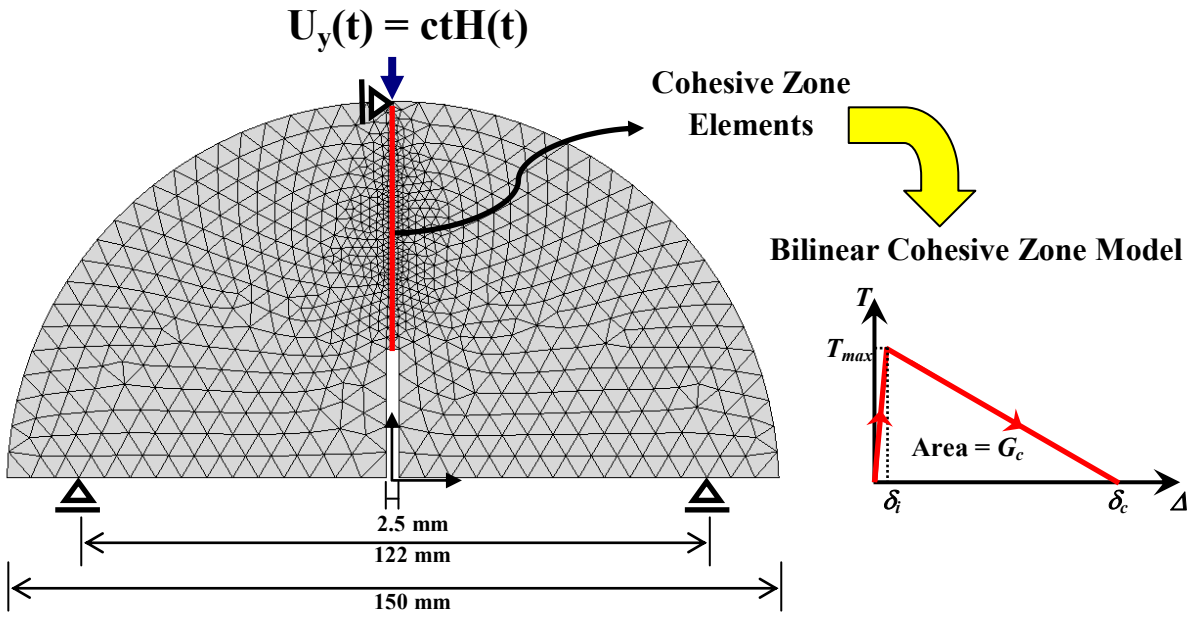

Figure 29. A finite element mesh and its boundary conditions to model the SCB testing.

As previously mentioned, the behavior of the bilinear cohesive zone elements is such that there is a recoverable linear elastic behavior until the cohesive traction (***T***) reaches the cohesive strength (T_{max}) in the traction-separation curve. When the traction reaches its maximum (*i.e.*, cohesive strength) at the corresponding displacement δ_i, damage starts to take place, and the ability of the cohesive zone elements to sustain traction is gradually reduced until it reaches a critical separation displacement, δ_c . At that point, the complete dissipative and irreversible failure of the cohesive zone element is reached, and the process is repeated for the next cohesive elements.

Besides cohesive strength, two other parameters define the shape of the bilinear traction-separation model: the initial slope, K, and the cohesive fracture energy, G_c. The fracture energy (*i.e.*, work of separation) is calculated by integrating the cohesive zone traction with respect to the separation distance (Δ). The value of the initial slope K, has been determined through a

convergence study designed to find a sufficiently large K value to guarantee a level of initial stiffness that renders insignificant artificial compliance of the cohesive zone model. In theory, the cohesive elements should be rigid prior to the initiation of damage because unit surfaces representing the formation of cracks are only duplicated in the damaged bodies after the beginning of the fracture process, which is triggered by the cohesive damage initiation criterion and represented by the softening part of the traction-separation curves. Due to the complexity associated with numerical implementation of the initial rigidity, the recoverable part prior to damage initiation is generally included in the traction-separation curve; however, the effects of artificial compliance due to the pre-peak ascending region should be minimized. Thus, a convergence study was conducted to obtain the value of K, and it was observed that a numerical convergence can be met when the pre-peak slope is greater than 5e+12 Pa/m (or, alternatively, λ_{cr} smaller than 0.00052 - see Figure 30). This value was used for the remaining simulations.

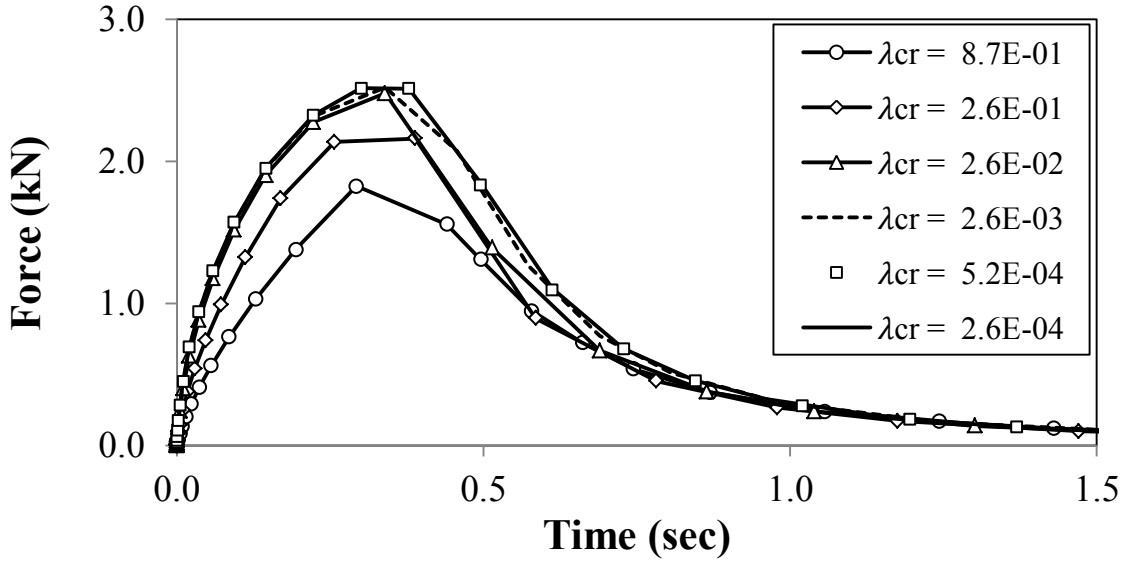

Figure 30. Convergence study to find the appropriate initial stiffness of cohesive elements.

Using the initial cohesive stiffness of 5e+12 Pa/m, T_{max} and G_c were determined for each loading rate via a calibration process between the simulation and test results. Cohesive zone parameters were adjusted until a good match between experimental results and numerical simulations was observed. Figure 31a and 31b present a strong agreement between the test results and numerical simulations. Validity of the cohesive zone properties determined herein was further verified from Figure 31c and 31d, where test results and numerical simulations for the crack (notch) mouth opening displacements (CMOD) and the crack (notch) tip opening displacements (CTOD) were plotted, respectively, as the loading time increased. As mentioned earlier, the CMOD and CTOD data were obtained from high-speed cameras of a DIC system. Figure 31 clearly demonstrates that the model parameters were accurately defined with no major discrepancies between the experimental and numerical results.

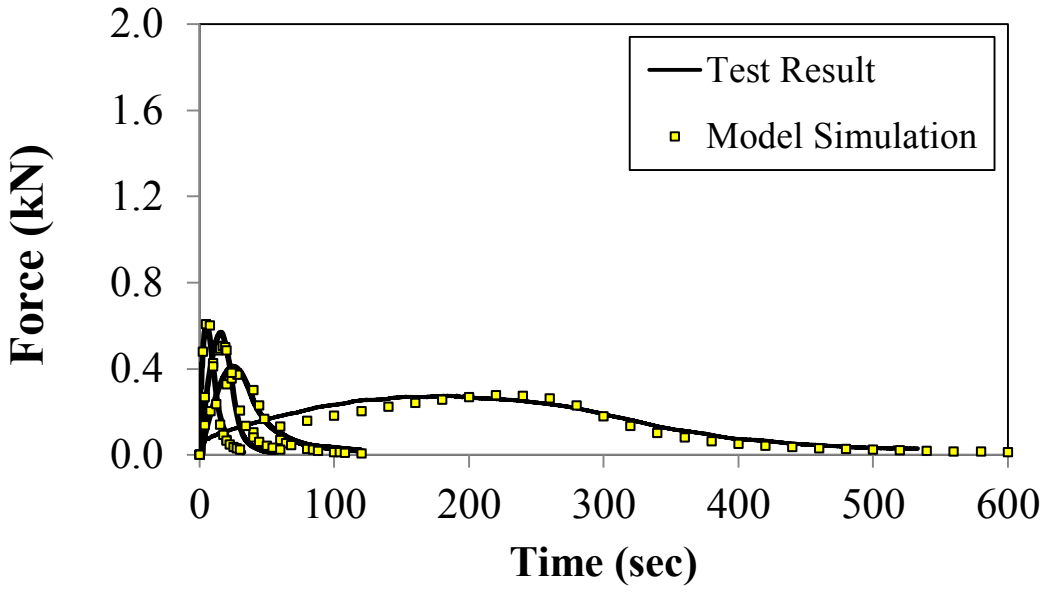

(a)

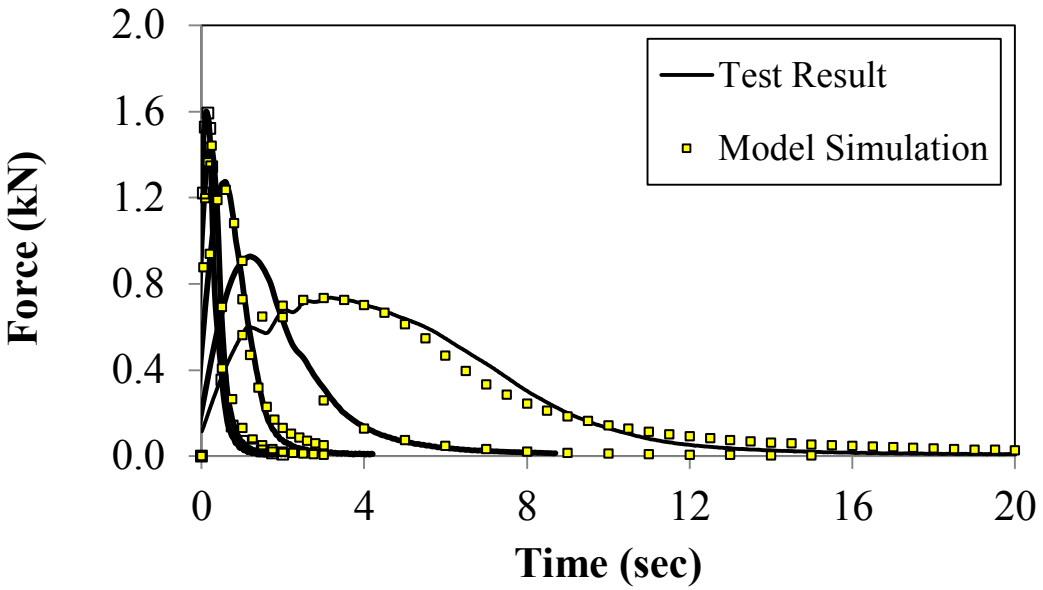
2.0
1.6
1.2
0.8
0.4
0.0
Force (kN)
0
4
8
12
16
20
Time (sec)
Test Result
Model Simulation

(b)

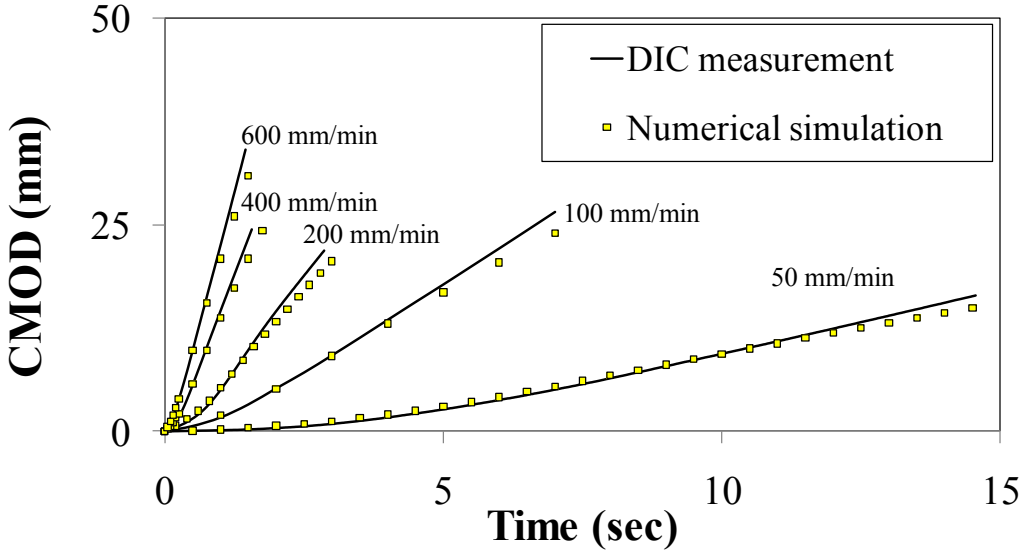
50
25
0
CMOD (mm)
0
5
10
15
Time (sec)
DIC measurement
Numerical simulation
600 mm/min
400 mm/min
200 mm/min
100 mm/min
50 mm/min

(c)

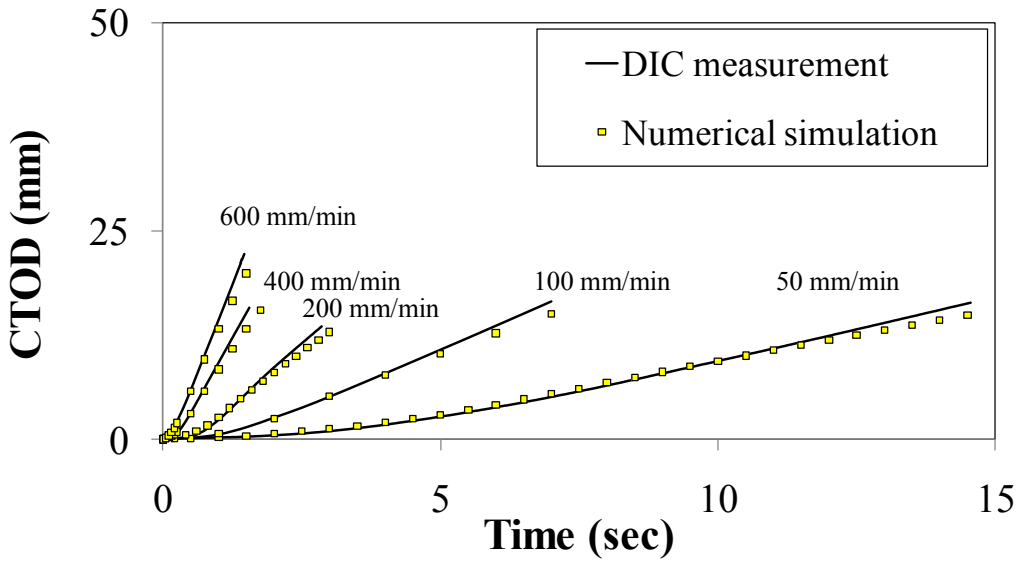

(d)

Figure 31. Test results vs. numerical simulation: (a) and (b) Reaction force, (c) CMOD, and (d) CTOD; as the loading time increased.

The two fracture parameters (T_{max} and G_c) identified at the local fracture process zone were plotted in Figure 32 as the applied loading rates varied. It appears that cohesive strength was fairly rate-independent until the loading rates are less than 50 mm/min, while the cohesive zone fracture energy generally increased as the loading rates became higher. The trends presented in Figure 32 infer that the rate-related nature of the fracture characteristics needs to be considered accordingly when modeling the mechanical performance of typical asphalt concrete mixtures and pavements in which a wide range of strain rates is usually associated due to the mixture's significant heterogeneity and the various loading conditions.

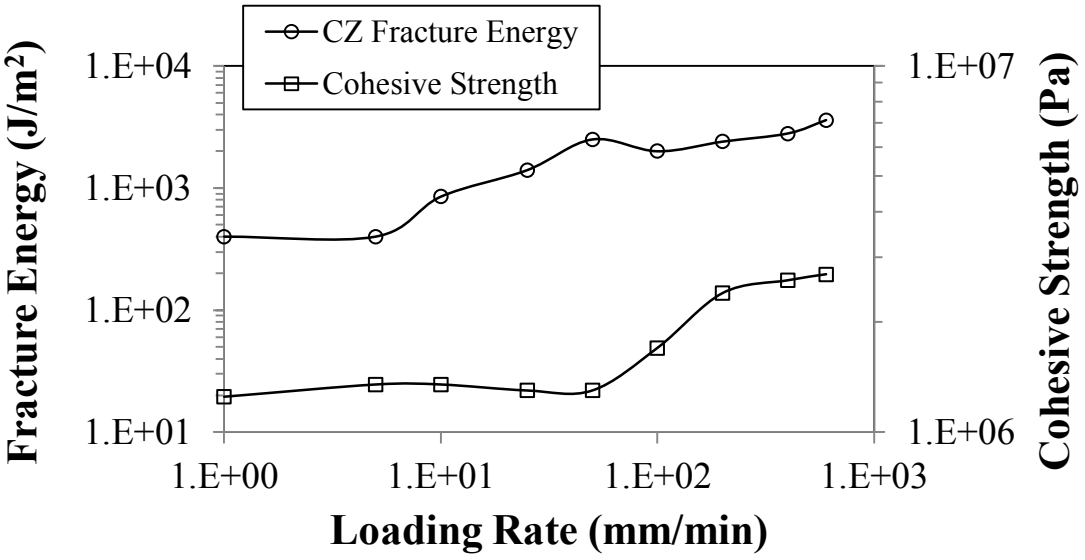

Figure 32. Cohesive zone fracture parameters at different loading rates.

The trends observed in Figure 32 are in accordance with what has been reported in several studies that attempt to characterize the rate-related fracture characteristics of adhesive and polymeric materials (Rahulkumar *et al.*, 2000; Nguyen *et al.*, 2004; Marzi *et al.*, 2009). In those studies, both strength and fracture energy tended to be constant when cracks propagated at lower speeds, while both fracture parameters increased with crack velocity for an intermediate level of crack velocity.

Figure 33 compares the fracture energy characterized at the local fracture process zone based on the cohesive zone model with the fracture energy usually obtained by calculating an area under the load-CMOD (or load-CTOD) curve that is normalized by the area of the fractured surface, *i.e.*, initial ligament length multiplied by the specimen thickness (Song *et al.*, 2008; Wagoner *et al.*, 2005a and 2005b). As presented in the figure, the fracture energies obtained from the area under the load-CMOD (or load-CTOD) curve were larger than the fracture energy obtained at the fracture process zone with the same trend. Furthermore, it is clear that fracture

energy values obtained from the load-CTOD curve were closer to the values characterized at the fracture process zone than those obtained from the load-CMOD curve. This observation was expected since, as noted previously, the energy obtained from CMOD measurements may overestimate the true fracture toughness, as it includes other sources of energy dissipation such as material viscoelasticity, which is not related to the fracture process.

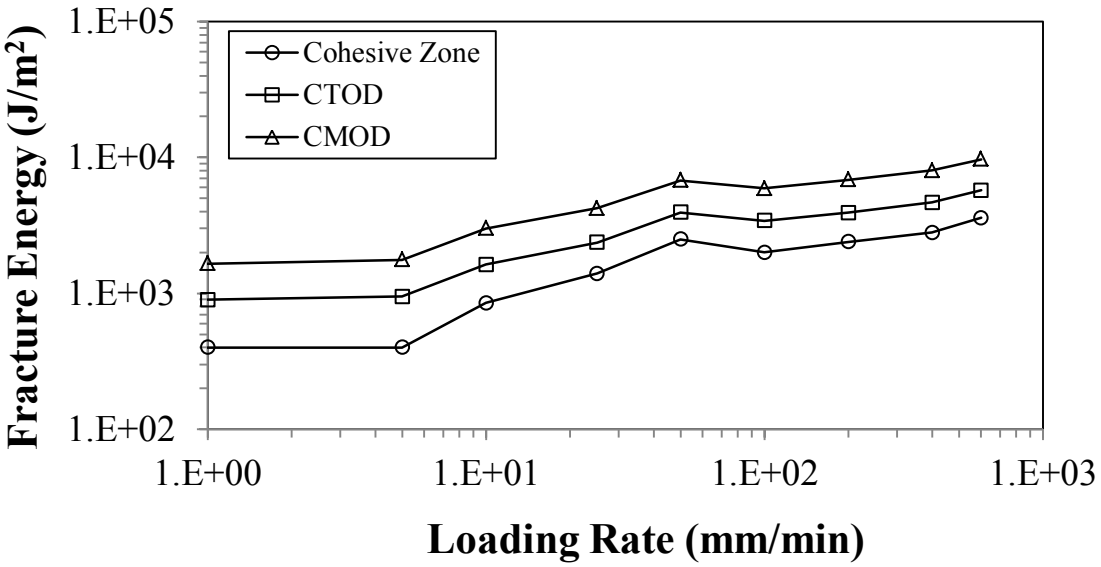

Figure 33. Fracture energy characterized based on local fracture process zone, CTOD, and CMOD.

In an attempt to seek a better identification of energy components involved during the matrix SCB fracture testing, an energy balance analysis was conducted, and results were presented in Figure 34b. The figure shows that the internal energy, which is equal to the external work done, is composed of several sources of energy: the recoverable strain energy that increased until the peak force (Figure 34a) and then abruptly decayed, the energy dissipated by the fracture process through the cohesive zones, and the energy dissipated due to material viscoelasticity of the FAM phase. The fracture energy was negligible to the peak force and

increased gradually as the cohesive zone elements separated. The energy dissipated by viscoelasticity increased before damage was initiated and afterwards stabilized. It is also obvious from the figure that the amount of energy dissipated by material viscoelasticity, in this particular case, is significant compared to the energy dissipated by the fracture process. Both sources of energy dissipation play important roles in the energy balance, which implies that each component should be considered separately with care when modeling fracture in viscoelastic media such as the FAM in this study.

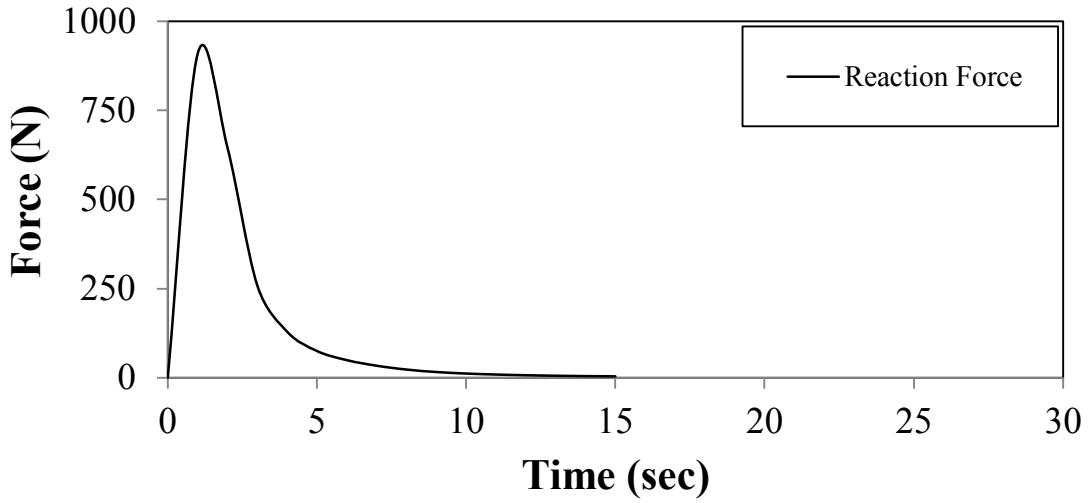

(a)

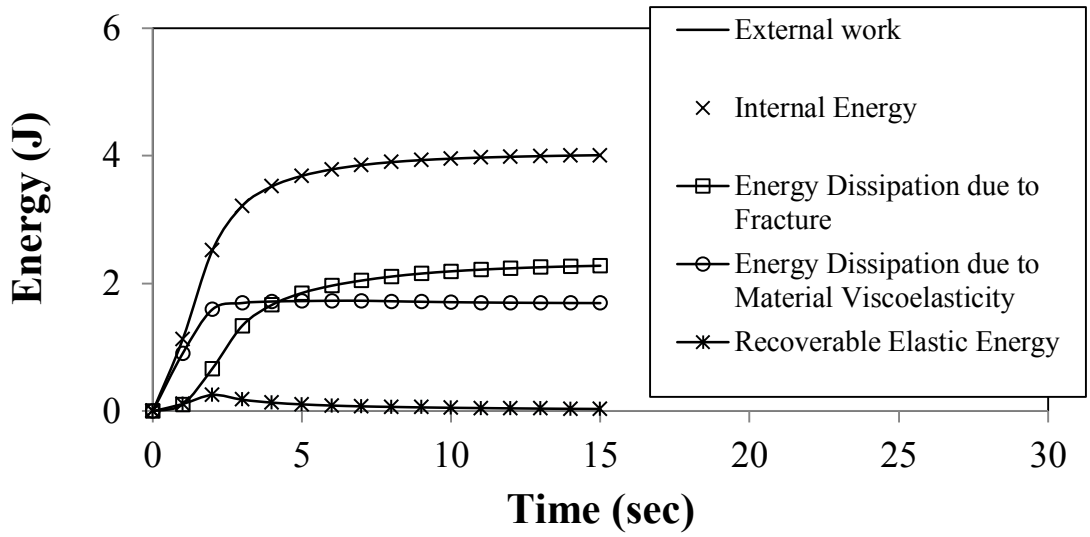

(b)

Figure 34. Energy balance from SCB fracture simulation.

Acknowledging the significance of the different sources of energy dissipation in the fracture problem of viscoelastic media, researchers also suggested that use of CMOD measurements to calculate fracture energy generally results in an overestimation of the true fracture energy of the material (Song *et al.*, 2008). In their work, Song *et al.* (2008) used the DC(T) geometry for fracture testing of asphalt concrete mixtures in low-temperature conditions by introducing two sets of displacement measurement systems: a typical CMOD clip gauge and a new displacement measurement, δ_{25}, which provides a local quantity of CTOD. δ_{25} CTOD measures crack tip opening displacements by attaching two clip gauges at the notch tip at a gauge length of 25 mm on both sides of the DC(T) specimen. Song *et al*. (2008) compared fracture energy resulting from the CMOD measurements with the fracture energy obtained from load-δ_{25} CTOD curves and found that fracture energy can be overestimated if it is calculated from CMOD measurements because the energy from CMOD measurements includes multiple

energy components such as the actual fracture energy and the energy dissipated during the deformation of the viscoelastic bulk material even at low temperatures.

6.2. Characterization of Rate-Dependent CZ Parameters

Figure 32 clearly demonstrates the rate-dependent fracture behavior of asphalt mixtures. As previously stated, the mere consideration of rate-dependence associated to the viscoelastic behavior of the bulk material is not enough to fully model the rate-dependent responses of the mixtures when those are subjected to damaging loads. Models that account for the local rate-dependent fracture behavior at the fracture process zone of asphalt mixtures, such as the one presented in this dissertation, must be used to simulate the localized rate-dependent fracture characteristics of the mixtures.

To illustrate the need for the development of fracture models that account for both material viscoelasticity and local rate-dependent fracture characteristics, simulations of SCB tests at four different loading rates, *i.e.*, 10, 25, 50, and 100 mm/min, were performed. For the first set of simulations (see Figure 35a), the bulk body was considered to behave elastically and fracture in the center line of the virtual SCB specimens was modeled as a rate-independent process. In the second set of simulations (see Figure 35b), the bulk body was modeled as a linear viscoelastic material, and fracture was again considered to be rate-independent.

For both sets of simulations, fracture properties were first calibrated to generate a good agreement between simulation and test results for the applied loading rate of 10 mm/min. Then, the calibrated parameters were used to simulate the other three cases. From Figure 35a, it is clear that the assumption of material elasticity generated results that greatly deviated from the test results. The elastic model was not able to capture the increase in the peak load as the applied

loading rate increased. That limitation was somehow overcome with the consideration of the viscoelastic behavior of the bulk body. As shown in Figure 35b, faster loading rates resulted in curves with higher peak loads. However, a considerable mismatch was still evident between simulation and test results. This demonstrates that the consideration of material viscoelastic constitution for the bulk body is not enough to predict the fracture behavior of asphalt mixtures. Other sources of rate-dependence, such as the local rate-dependent fracture behavior at the fracture process zone of the mixtures, should also be considered in the model.

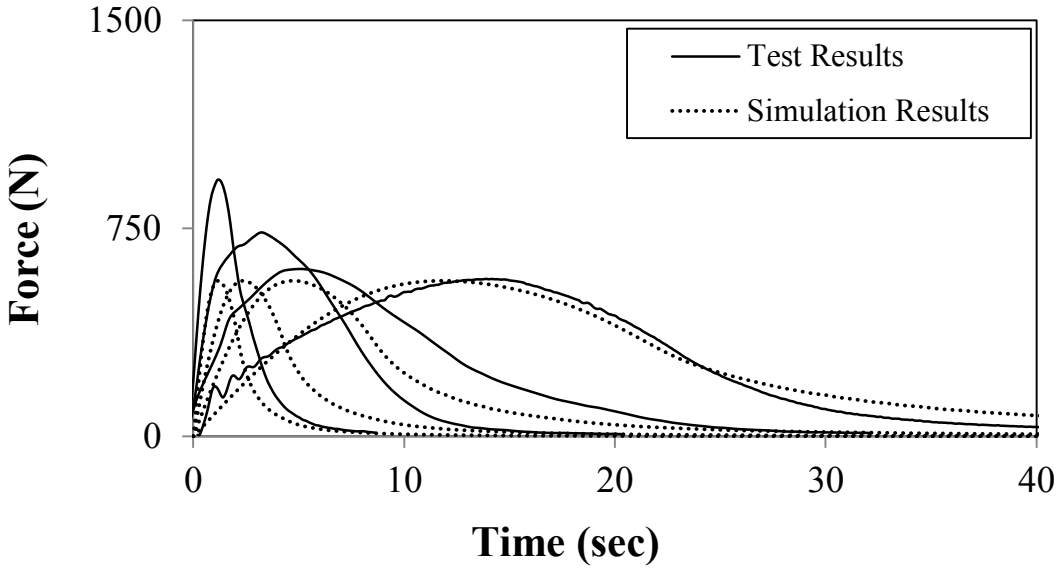

(a)

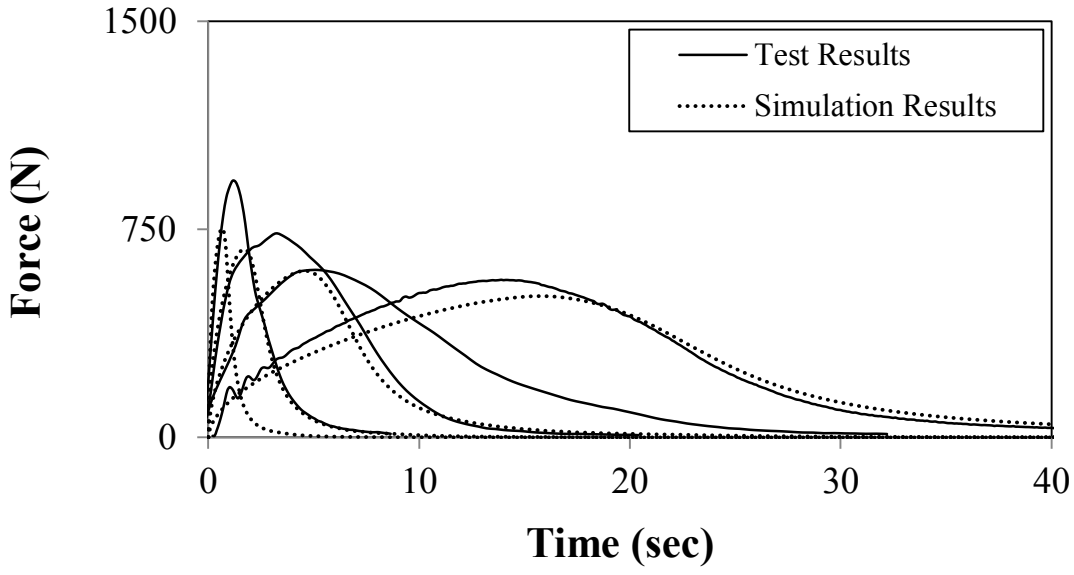

(b)

Figure 35. Simulation of SCB test for various loading rates considering: (a) Material elasticity and rate-independent fracture; and (b) Material viscoelasticity and rate-independent fracture.

The rate-dependent characteristics of cohesive strength and fracture energy shown in Equations 38 and 39, respectively, were calibrated using the newly developed rate-dependent cohesive zone model and simulations of SCB tests considering material linear viscoelastic behavior for the bulk body. An optimization process was performed to calibrate the functions until a reasonable match between numerical simulation and experimental results was observed. Three different loading rates, *i.e.*, 10, 50, and 100 mm/min, were used in the calibration process. Figure 36a presents simulation results compared to SCB test results for the three loading rates and indicates very good agreement for all three rates simulated. To obtain the good agreement shown in Figure 36a, the calibrated parameters used were β_T = 0.2, β_G = 0.5, $\dot{\delta}_e^{ref}$ = 4.0E-8 m/sec, T_{max}^{ref} = 1.0E+06 Pa, and G_c^{ref} = 1000 J/m^2. To confirm that the parameters were properly calibrated, an intermediate loading rate, 25 mm/min, was simulated and the result is shown in

Figure 36b. The good prediction shown in Figure 36b demonstrates that the calibration has been successfully accomplished.

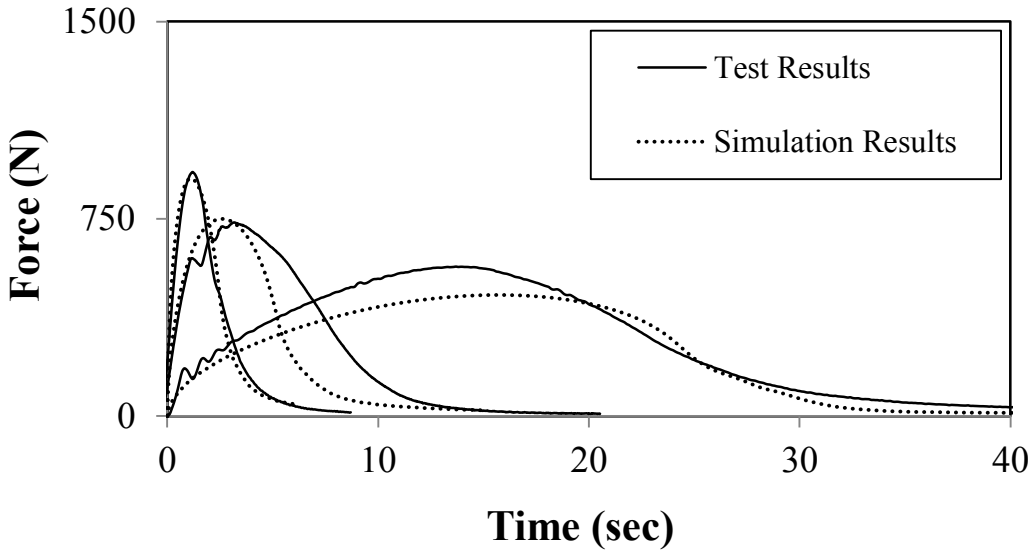

(a)

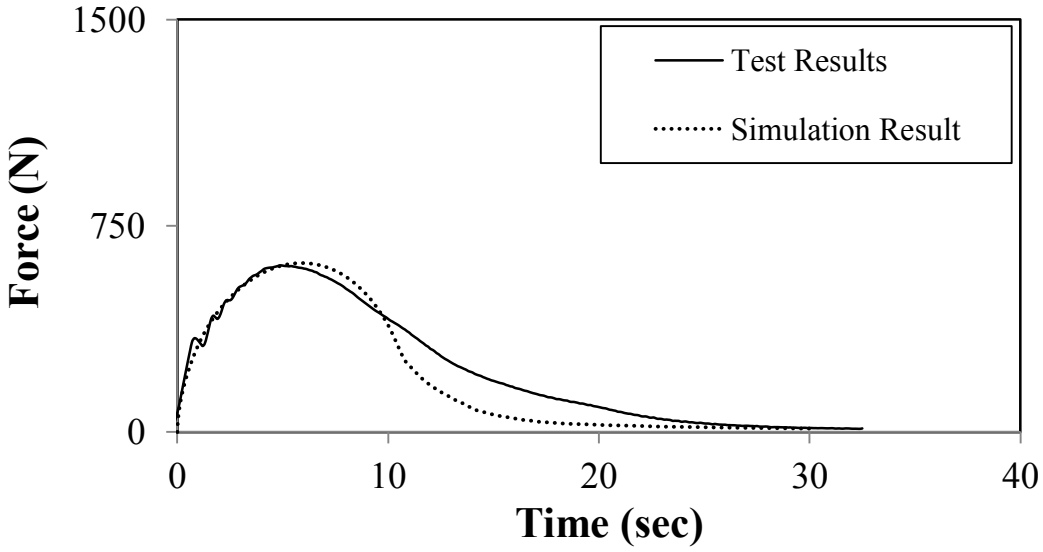

(b)

Figure 36. Calibration of rate-dependent fracture functions: (a) Determination of function parameters; and (b) Prediction of test results for an intermediate loading rate.

Chapter 7

Microstructure Modeling of HMA Mixtures

In this chapter, the computational microstructure model was used to simulate different problems. First, simulations were performed to predict the dynamic modulus of HMA samples and the results were compared to test results obtained from laboratory experiments. Model predictions were also compared to dynamic modulus predictions made by other modeling approaches to demonstrate the potential of the proposed computational microstructure model. Then, the newly implemented rate-dependent cohesive zone fracture model was used to simulate fracture within the microstructure of virtual samples of HMA mixtures. Finally, parametric analyses were performed to demonstrate the ability of the rate-dependent model to account for the effects of important mixture variables on the mechanical behavior of the mixtures.

7.1. Dynamic Modulus of HMA Mixtures

Dynamic modulus, |E*|, has been employed by mechanistic-empirical pavement design protocols to compute the mechanical responses of pavement structures. One of these pavement design protocols was developed in 2004 by the American Association for State Highway and Transportation Officials (AASHTO) and was named as the Mechanistic-Empirical Pavement Design Guide (MEPDG). The material properties used to relate stresses and strains in the MEPDG software are Poisson's ratio (generally assumed to be a constant value) and elastic modulus obtained from dynamic modulus master curves at a given temperature and loading frequency. Even if the two lower hierarchical input levels of MEPDG require only asphalt binder

properties and mixture volumetric characteristics to predict |E*| using Witczak's predictive equation (Witczak and Bari, 2004), the most accurate predictions can be made by performing laboratory dynamic modulus tests that provide level one stiffness characteristics in a dynamic modulus master curve form. Several standards and their adaptations have been used to obtain the dynamic modulus of asphalt concrete mixtures experimentally (ASTM D3497-79; AASHTO TP62; Kim and Seo, 2004). However, the determination of master curves in a wide range of loading frequencies and temperatures has been recognized as a time consuming process.

In the attempt to reduce costs and time required to obtain the dynamic modulus master curves, researchers have been trying to predict the |E*| of the mixtures with semi-empirical (Andrei *et al.*, 1999; Christensen *et al.*, 2003; Bari and Witczak, 2006) and analytical (Hashin, 1965; Christensen, 1969; Buttlar *et al.*, 1999; Kim and Little, 2004; Huang *et al.*, 2007; Shu and Huang, 2008) formulations. However, these approaches have generally shown significant limitations. Semi-empirical model parameters are generally applicable only to local material and environmental characteristics. On the other hand, analytical micromechanics models do not account for the actual geometric heterogeneity and interactions among components in the mixture.

To overcome the generic limitations of the semi-empirical and analytical micromechanics predictive approaches, computational microstructure modeling has actively been pursued. One of the advantages of this modeling approach is that it can account for the effect of mixture heterogeneity by dealing with mixture constituents (*e.g.*, aggregates, asphalt binder) separately. The computational microstructure method also allows a more comprehensive examination of the microstructural, inelastic material behavior of the mixtures so that stresses and strains within the mixture microstructures can be analyzed more realistically. Several studies (Masad *et al.*, 2001;

Papagiannakis *et al.*, 2002; Dai and You, 2007; Aragão *et al*., 2009a, 2009b, and 2010; Aragão and Kim, 2010) proposed finite element method (FEM)-based models, and an explicit numerical technique, called the discrete element method (DEM), has also been employed by several researchers (Abbas and Shenoy, 2005; You and Buttlar, 2006; You *et al.*, 2009).

Although several computational microstructural attempts have shown success, to a certain extent, for predicting the dynamic modulus of asphalt concrete mixtures for the past decade, most of the work found in the open literature has used low-temperature testing conditions, in which there is a smaller dissipation of energy. Consequently, the material behaves much more elastically. Thus, this research focused on the characterization of dynamic modulus master curves of asphalt concrete mixtures at intermediate reference temperatures, where the temperature- and rate-dependent viscoelastic characteristics are much more evident. Two popular semi-empirical models (Witczak's model (Bari and Witczak, 2006) and the modified version (Christensen *et al.,* 2003) of the Hirsh's model (Hirsch, 1962)), an analytically developed micromechanics model by Hashin (Hashin, 1965), and the computational microstructure approach based on the FEM technique were investigated. Table 7 shows the input parameters required by the semi-empirical and analytical models evaluated. Model predictions were compared with dynamic modulus test results obtained from cylindrical asphalt concrete specimens in a wide range of loading frequencies at the target temperature of 21^{o}C. The predictive power of each approach was compared and discussed.

Table 7. Input parameters required by the semi-empirical and analytical models evaluated.

Model	INPUTS	
Hashin	ν_m	0.35
	G_p *(Pa)*	2.2E+10
	V_p	0.866
Witczak	ρ_{200} (%)	4.9
	ρ_4 (%)	27.6
	ρ_{38} (%)	10.8
	ρ_{34} (%)	0.0
	V_a (%)	3.9
	V_{beff} (%)	10.4
Modified Hirsch	*VMA (%)*	14.3
	VFA (%)	72.7

To accomplish the analytical micromechanics and the computational microstructure modeling, asphalt concrete microstructure is necessary. Two-dimensional microstructure of the asphalt concrete mixtures was obtained by using a digital image process of scanned images taken from sawn Superpave gyratory compacted (SGC) samples (150 mm in diameter and 170 mm tall). The compacted cylinders were cut along a vertical plane to reveal the two-dimensional cross-section of the samples. Then, an image treatment process was performed to convert the virgin image (in gray scale) to a binary format (black and white representing the FAM and the aggregates, respectively). The portion of the aggregate gradation finer than 0.30 mm was not distinctively captured by the digital image processing. Therefore, the black portion mixed with particles smaller than 0.30 mm was considered to be the FAM phase (asphalt cement mixed with aggregates less than 0.30 mm and entrained air voids). Figure 37 shows a digital image of an asphalt concrete mixture (100 mm wide and 150 mm tall) after the digital image treatment has been applied. The treated image was then analyzed to quantify the volume fractions of

aggregates in the mixture, because the volume fraction of aggregates (V_p) was used in the Hashin's analytical micromechanics model (described in a previous section).

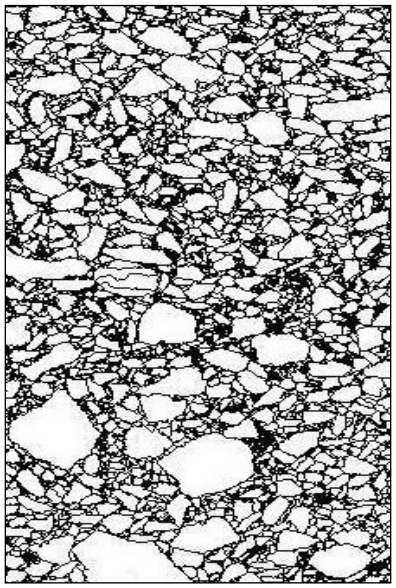

Figure 37. Asphalt concrete microstructure after digital image treatment.

As shown in Figure 37, two distinct phases (aggregates larger than 0.30 mm signified in white and FAM phase in black) appeared. Therefore, laboratory tests were conducted to characterize the material properties of each phase in the mixtures. The experimental results were then used as model inputs for the analytical micromechanics and the computational microstructure models (Hashin's analytical model and the FEM-based computational model, respectively). The material properties required for the models were the linear elastic properties of aggregate particles larger than 0.30 mm and the linear viscoelastic properties of the FAM phase, both obtained as described in an earlier chapter.

With the treated digital image of mixture microstructure and the material properties of each individual mixture constituent, computational microstructure modeling could be conducted. In order to simulate the complex geometry of the microstructure most accurately, the digital

image was discretized to produce 382,704 three-node linear triangular elements; this could represent the smallest aggregate particles (0.30 mm) as a distinctive element. For this particular study, a two-dimensional approximation of the three-dimensional mixtures was adopted because of the significant geometric complexity. Although real events are three-dimensional in nature, a great deal can still be learned from a two-dimensional simplification of the problem. Two-dimensional modeling can provide computational efficiency, and it is a necessary step towards the understanding of global three-dimensional performance.

Isotropic symmetry was considered for both the FAM mixture and the aggregate particles, which were modeled to be linear viscoelastic and linear elastic materials, respectively. Air voids were not explicitly considered in the current model. As an entrained form in the FAM phase, air voids were indirectly considered by equating the apparent density of the FAM to the black portion in the asphalt mixture microstructure. Better representation of air voids in the model remains as future work.

For the FEM simulation, commercial software *ABAQUS* (2008) was used. With the mesh developed, boundary conditions were applied to constrain the vertical displacements (U_Y) of the nodes at the bottom (see Figure 38). A compressive haversine load (T_Y) was evenly applied to the top nodes. To construct a dynamic modulus master curve, a wide spectrum of loading frequencies was simulated (10^{-4} to 10^{4} Hz). Averaged vertical deformations from the two sets of virtual gauge points (shown in Figure 38) were used to calculate the dynamic modulus, defined

simply as the ratio of the haversine stress amplitude to the haversine strain amplitude.

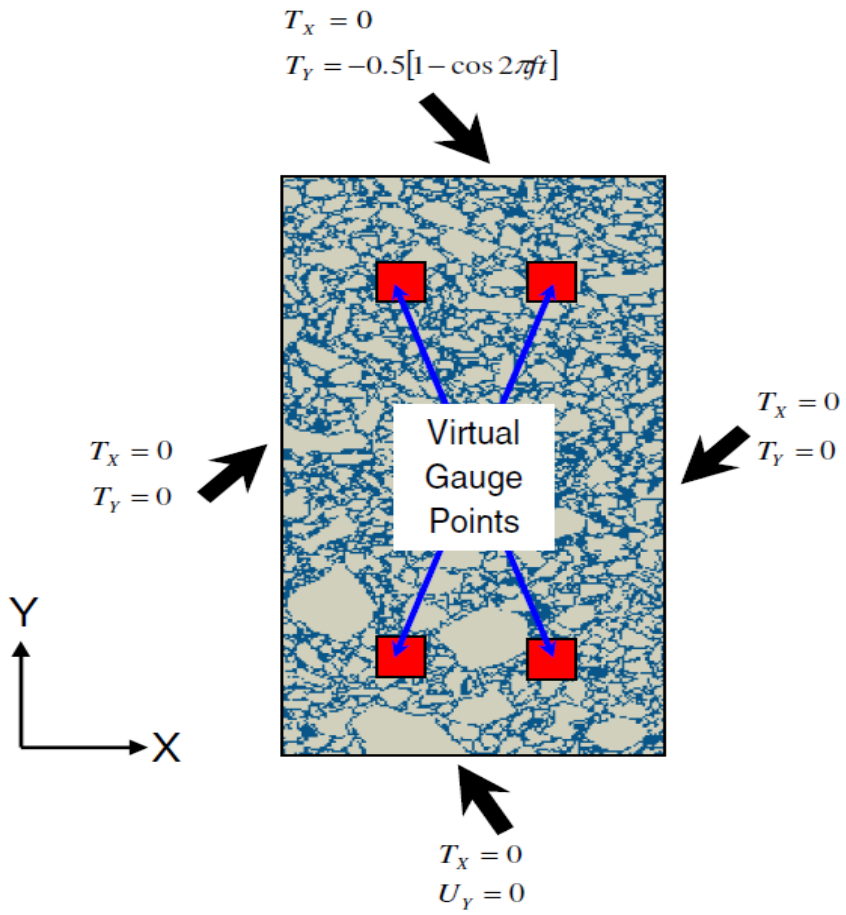

Figure 38. FEM mesh, virtual gauges, and boundary conditions imposed for simulations.

Figure 39 shows dynamic modulus comparisons between each of the predictive models and the experimental data. In general, all predictive models were in fair agreement with the test results. Hashin's model under predicted the dynamic modulus at lower frequencies and over-predicted at higher loading frequencies. The worst predictive power of Hashin's model was expected given that it does not account for the geometric complexity of graded particles and contacts among materials. Witczak's equation simulated dynamic moduli greater than laboratory test results. A vertical shift between the prediction and measurement was observed. The modified Hirsch model typically produced lower moduli than the test, but the deviation between the two

was not significant. Comparison between experimental results and the FEM microstructure model presented a relatively higher deviation at lower loading frequencies but better predictions when the loading frequency was larger. Several factors are related to the deviation, including some clear model limitations such as (a) no explicit consideration of air voids within the mixtures, (b) lack of aggregate-aggregate contact, and (c) two-dimensional simplification of the three-dimensional problem.

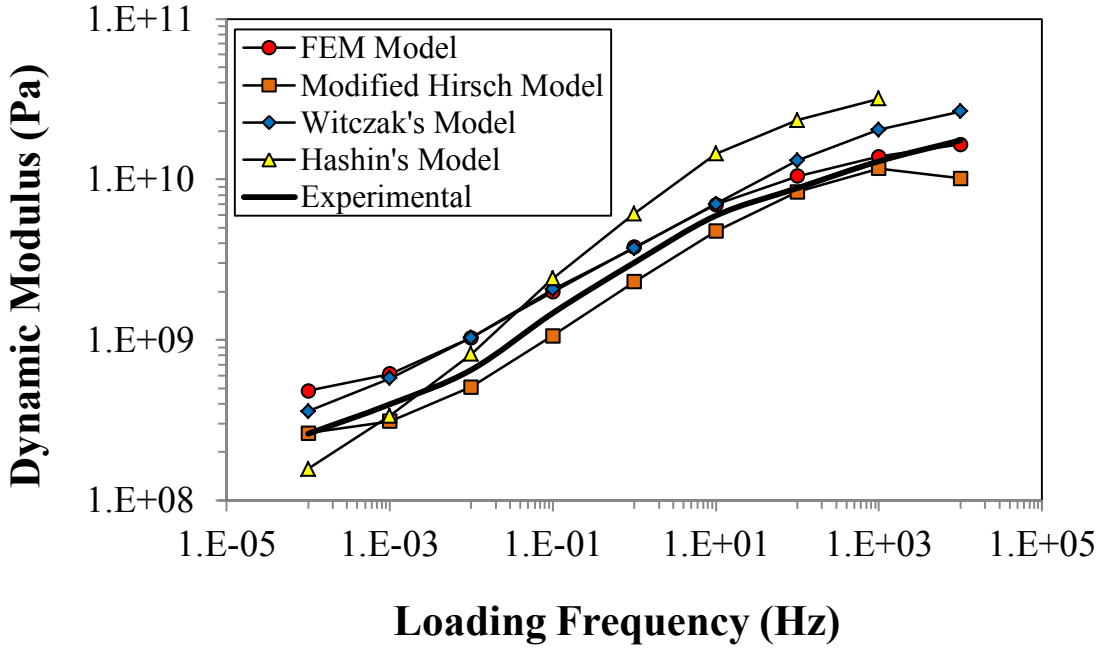

Figure 39. Comparison of dynamic moduli obtained from different approaches.

To investigate the predictive power of each model in a more distinctive manner, the predicted dynamic moduli obtained from each model were cross-plotted to the experimental dynamic moduli, and the results are shown in Figure 40. As shown in the figure, the modified Hirsh model and the FEM model exhibited a relatively small deviation from the line of equality. Hashin's model deviated from the line of equality gradually from lower frequencies (producing low moduli) to higher frequencies (producing higher values of modulus).

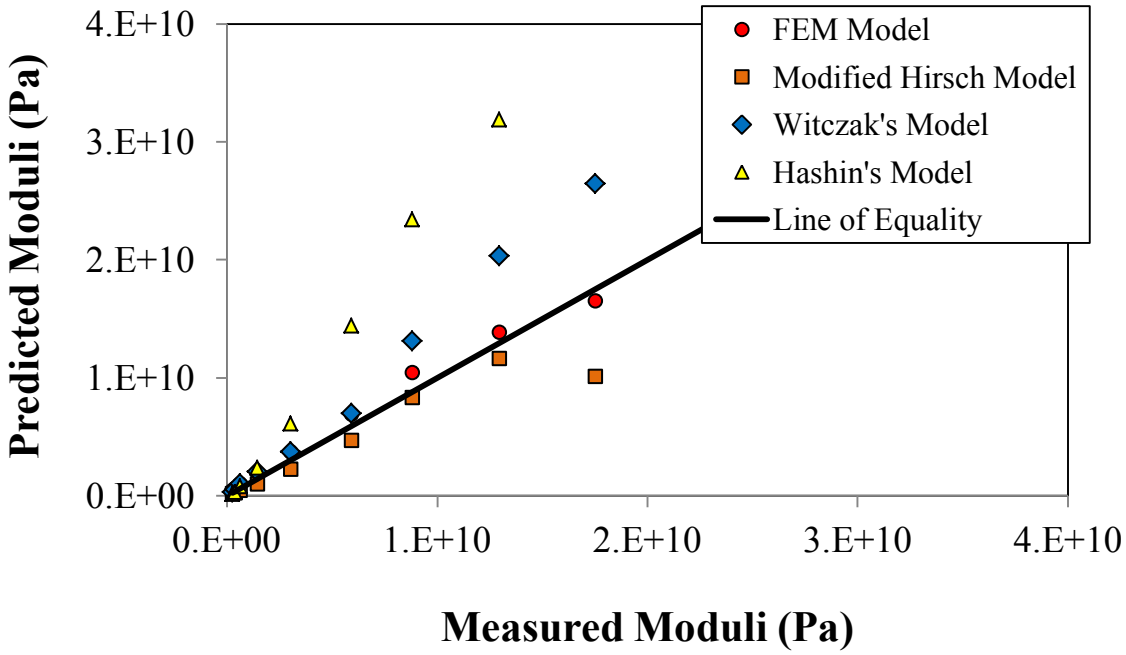

Figure 40. Cross-plots between experimental dynamic moduli and predictions from each model.

In spite of the aforementioned limitations of the current version of the FEM model, the results presented in Figure 40 indicate the high potential of the computational microstructure modeling technique. Computational microstructure modeling has been regarded as an excellent tool for a closer analysis of the stresses and strains within the microstructure of the mixture, which is not possible with the other models presented here. Furthermore, the FEM microstructure model seems to be the best predictive model for evaluating the changes in the overall mixture stiffness given any changes in the mixture composition and mechanical/geometric characteristics of mix components.

7.1.1. Parametric Analysis

A parametric analysis was conducted in this study to illustrate the ability of the computational microstructure model to evaluate the effect of mechanical properties of different mixture constituents on the overall dynamic modulus of the mixture. First, simulations were conducted to evaluate the effect of asphalt content, which affects mixture volumetrics such as V_{beff}, *VMA*, and *VFA*. Two different binder contents (11.5% and 15.4% by total mass of the FAM) were evaluated with a constant aggregate modulus of 60.9 GPa. From the results shown in Figure 41, it is obvious that the binder content and corresponding mixture volumetrics play an important role in the dynamic modulus of mixtures. The use of the FAM properties with higher binder content resulted in lower dynamic modulus values, as expected. The second parametric study was performed by varying aggregate stiffness with three different elastic moduli (20.0, 50.8, and 60.9 GPa), with the same amount of binder content, 15.4%. The simulation results shown in Figure 42 infer that the stiffness of the aggregates strongly affected the overall stiffness of the mixtures.

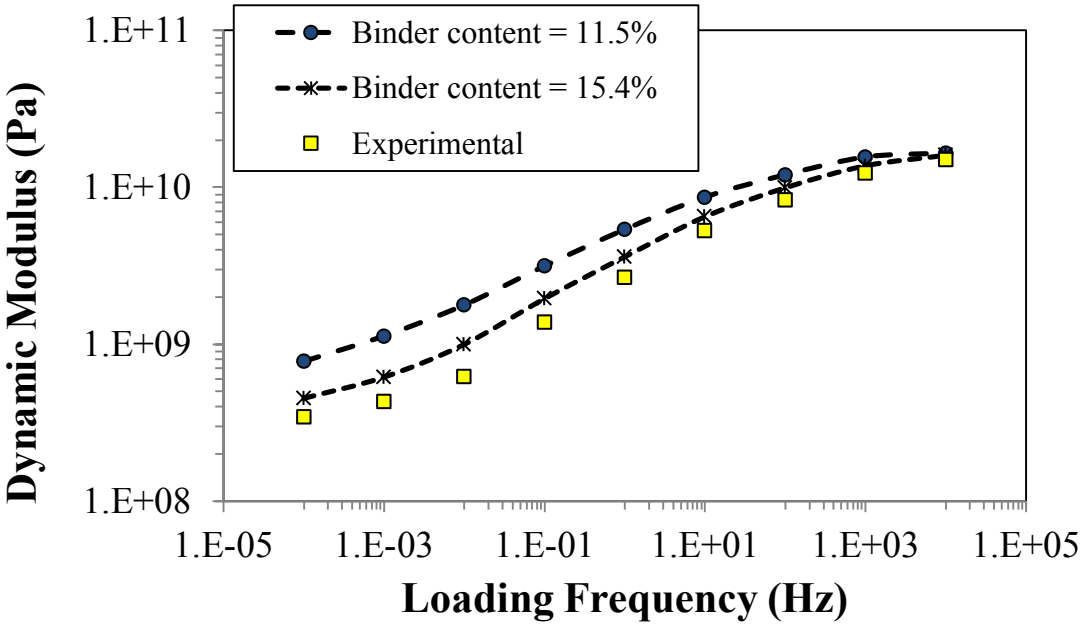

Figure 41. Parametric analysis on binder content in the FAM phase.

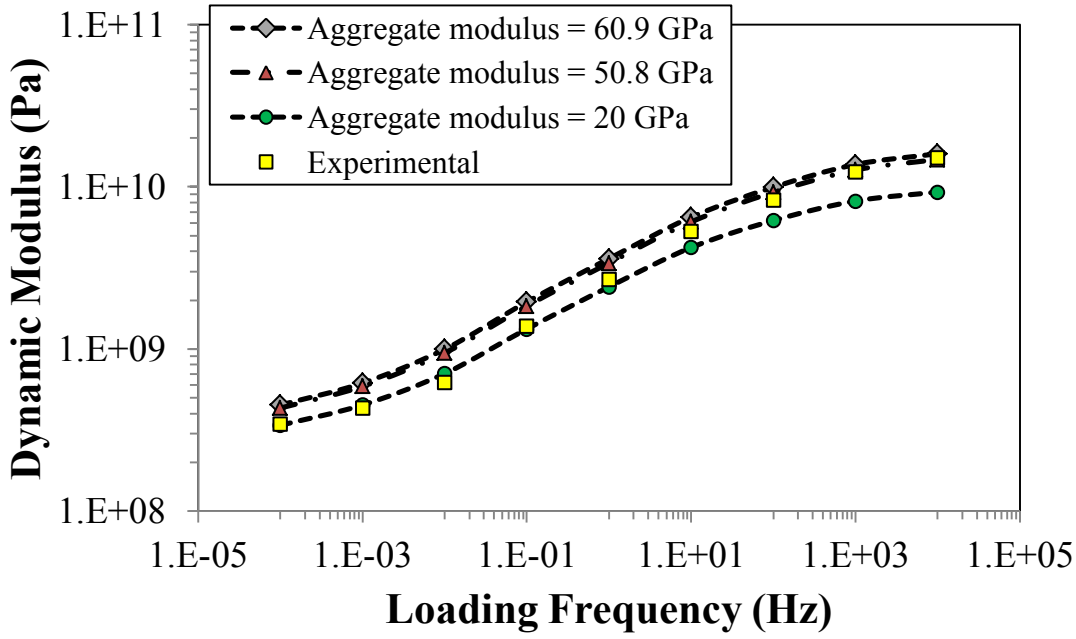

Figure 42. Parametric analysis on aggregate stiffness.

7.2. Rate-Dependent Fracture of HMA Mixtures

As previously described, asphalt concrete mixtures are particulate composites in which a rigid skeleton of aggregate particles is held together by a softer phase of FAM mixture that is composed of asphalt binder, air voids, and fine aggregates. To predict the mechanical behavior of these heterogeneous and viscoelastic composites that experience damage at different length scales, several researchers have proposed various computational predictive models based on the discrete and the finite element methods. These computational microstructure models have stronger scientific basis than empirical methodologies that are based on statistical analyses of regional and case-specific databases. In comparison to other computational approaches, such as those based on the continuum damage mechanics theory, the computational microstructure models are also advantageous because they account for diverse complexities (*e.g.*, material inelasticity, heterogeneity, anisotropy, multiple damage forms). Additionally, computational microstructure models can greatly reduce the costs associated with laboratory experiments because they generally only require individual mixture constituent properties as model inputs.

The accuracy of such microstructural models greatly depends on the level of understanding of the physics of the real problem and on how well the computational models simulate those physical characteristics. These characteristics include the heterogeneity and random distribution of aggregate particles, the inelasticity of the FAM, the large size of the plastic zones around the crack tips of the damaged mixtures, and the rate-dependent characteristics of those fracture zones. Various models have included some of these features, but these models have rarely considered the rate-dependent fracture behavior of the mixtures. This rate-dependent behavior is not exclusively related to the inelasticity of the bulk material. Thus, the mere consideration of viscoelastic constitution for the bulk body is not enough to fully

describe the rate-dependent damage behavior of the mixtures. Instead, the rate-dependence of their fracture process zones should be investigated as a separated phenomenon and properly considered in the models.

To appropriately model that rate-dependent damage behavior, first appropriate fracture test methods should be used. Additionally, research efforts are also required for a better understanding of the fracture characteristics of the mixtures when those are subjected to intermediate temperature conditions. Therefore, this research has proposed a modeling approach based on the cohesive zone concept that combines experimental results and computational modeling of tests with SCB specimens to characterize rate-dependent fracture characteristics of asphalt mixtures at intermediate temperature conditions.

To demonstrate the ability of the rate-dependent fracture model to simulate rate-related fracture in HMA mixtures, simulations of a three-point-bending test were performed by applying different levels of displacement rates to the top center point of virtual HMA samples. Table 8 summarizes the input parameters used in the simulations.

Table 8. Model inputs for HMA fracture simulations

Undamaged Properties					Dimensions (mm)
Linear Elastic Properties of Coarse Aggregates		Linear Viscoelastic Properties of FAM			
		i	E_i (MPa)	ρ_i (sec)	
Young's modulus (Pa)	6.09E+10	1	3026.1	8.00E-05	150 x 60
		2	1484.1	8.00E-04	
		3	1333.6	8.00E-03	
		4	435	8.00E-02	
Poisson's ratio	0.15	5	159.6	8.00E-01	
		6	50	8.00E+00	
		7	17.9	8.00E+01	
		8	3	8.00E+02	
		∞	12.2	-	

Case	Rate-Dependent Fracture Properties of FAM					Loading rate (mm/min)
	β_T	β_G	T_{max}^{ref} (MPa)	G_c^{ref} (kJ/m2)	$\dot{\delta}_e^{ref}$ (m/sec)	
Figure 44a	0.20	0.50	1.0	1.0	4.0E-08	10, 25, 50
Figure 45a	0.20, 0.30, 0.40	0.50				50
Figure 45b	0.40	0.50, 0.70, 1.00				
Figure 45c	0.40	0.50	0.5, 0.8, 1.0	1.0		
Figure 45d	0.40	0.50	1.0	1.0, 1.5, 2.0		
Figure 49	0.15	0.15	0.5	0.2		100

Figure 43a shows the heterogeneous microstructure, FE mesh, and boundary conditions of the first virtual sample of HMA used in this section. Figure 43b shows the central region of the virtual specimen (15 mm x 55 mm) where cohesive elements were inserted within the FAM phase because fracture in asphalt mixtures subjected to intermediate temperature conditions typically occurs within the FAM phase. The decision to limit the area of potential fracture to the central region of the specimens was made to reduce the artificial compliance effects inherently produced by intrinsic cohesive zone models, such as the one used in this research, that are intensified with the increase of the number of cohesive elements in the meshes. Additionally,

preliminary tests conducted in laboratory with beams of HMA mixtures revealed that fracture is limited to that central region. Thus, the insertion of cohesive elements within the whole microstructure of the virtual beams was unnecessary and would increase the computational cost of the simulations.

Figure 43c shows an example of a fractured beam and demonstrates the ability of the model to simulate crack propagation within the heterogeneous microstructures of the mixtures. The inter-granular cracking evolution is in fact one of the important features of computational microstructure models as it allows such models to predict the local fracture characteristics of the mixtures in a more realistic way than other computational models based on the continuum damage approach. Such microstructure models can also be used to evaluate the effects of material properties of mixture components and geometric characteristics of aggregate particles on the fracture behavior of the mixtures without the need for additional expensive and time-consuming laboratory performance tests.

Figure 44a presents simulation results by plotting the reactive force as a function of loading time for three different loading rates: 10, 25, and 50 mm/min. Clearly, rate-dependent fracture behavior is observed as slower loading rates produced more compliant responses than faster loading rates. Figure 44a also shows simulation results using rate-independent cohesive fracture properties. The figure reveals that the overall rate-dependent behavior of the sample was much more evident when the rate-dependent fracture characteristics of the mixtures were considered in the simulations. This was also observed in a study by Aragão and Kim (2010). In that study, the authors demonstrated that the use of rate-independent cohesive fracture properties to predict the fracture behavior of viscoelastic and heterogeneous asphalt mixtures generated predictions that greatly deviated from test results. Different sets of cohesive fracture properties

were required to match test results for different displacement rates applied to the testing specimens. Extra efforts are needed to validate the proposed model via the comparison with experimental test results of real HMA samples. The validation process is currently in progress and significant findings will be presented in the near future.

Another advantage of the computational microstructure modeling approach is that it allows a more comprehensive examination of the microstructural, inelastic material behavior so that stresses and strains within the microstructure can be analyzed more realistically. To illustrate that capability, Figure 44b to 44g show progressive microstructural fracture and stress (S11) contour plots at simulation times ranging between 4 and 14 seconds for the applied displacement rate of 25 mm/min. The contour plots revealed that there was a higher concentration of stresses on the stiff aggregate particles. High stress levels were also observed around the tip of the crack. Stress levels were drastically reduced at the bottom of the beam after the formation of the macro-crack within the sample microstructure.

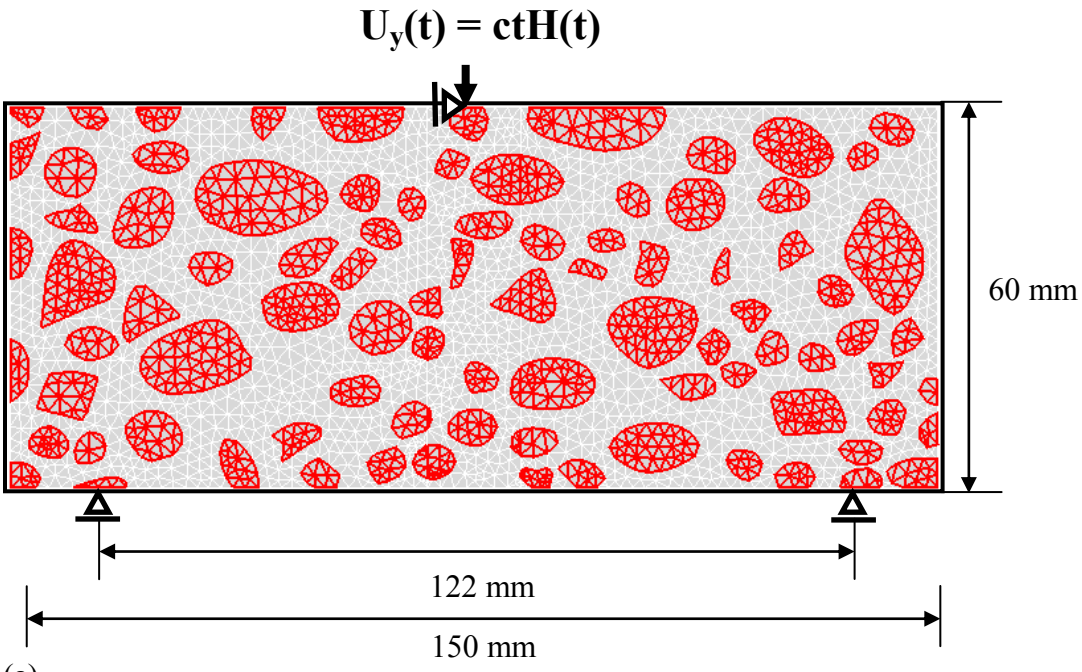

(a)

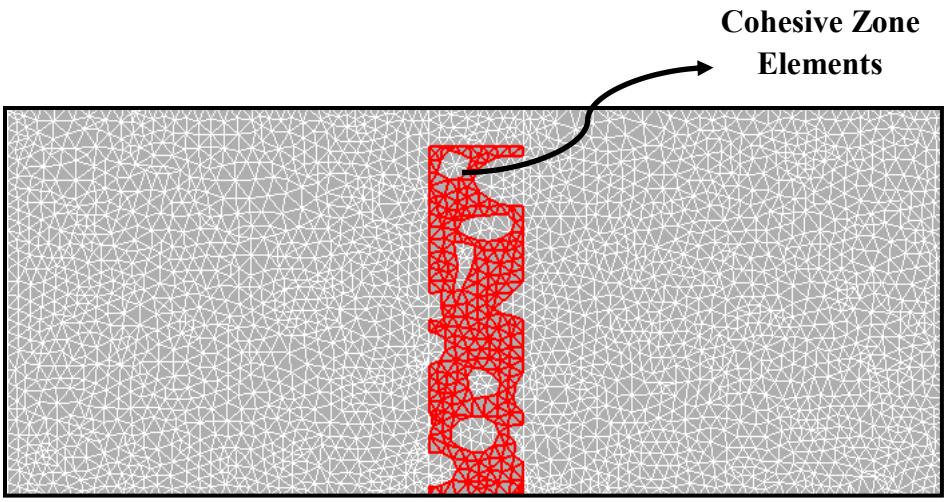

(b)

(c)

Figure 43. Simulation of a three-point-bending test: (a) FEM mesh and microstructure of virtual HMA beam sample; (b) Central region of the virtual specimen where cohesive elements are inserted within the FEM mesh; and (c) An example of a crack path within the heterogeneous microstructure of the beam.

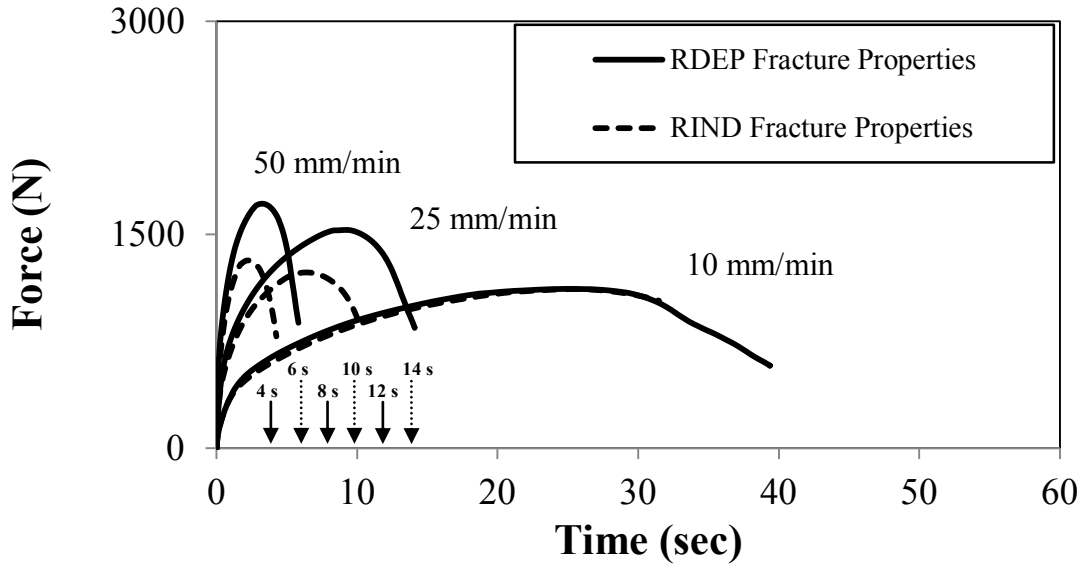
3000
1500
0
Force (N)
RDEP Fracture Properties
RIND Fracture Properties
50 mm/min
25 mm/min
10 mm/min
4 s
6 s
8 s
10 s
12 s
14 s
0
10
20
30
40
50
60
Time (sec)

(a)

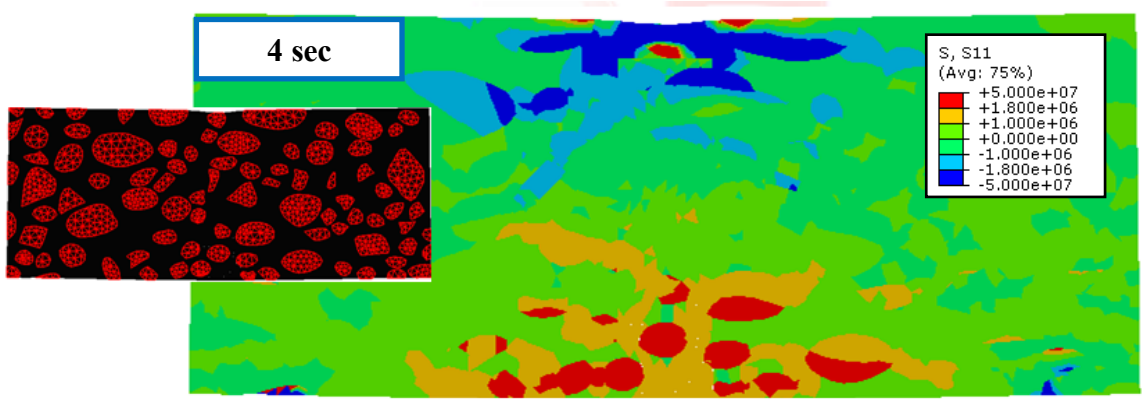
4 sec
S, S11
(Avg: 75%)
+5.000e+07
+1.800e+06
+1.000e+06
+0.000e+00
-1.000e+06
-1.800e+06
-5.000e+07

(b)

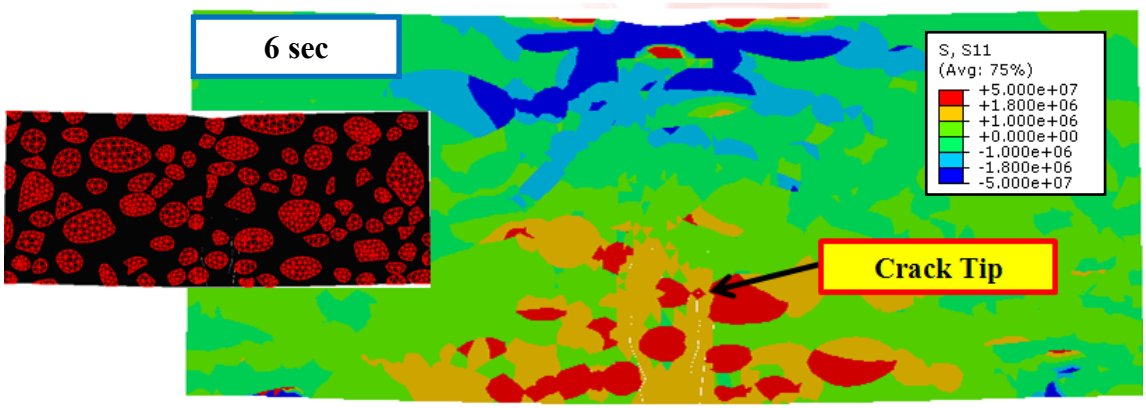
6 sec
S, S11
(Avg: 75%)
+5.000e+07
+1.800e+06
+1.000e+06
+0.000e+00
-1.000e+06
-1.800e+06
-5.000e+07
Crack Tip

(c)

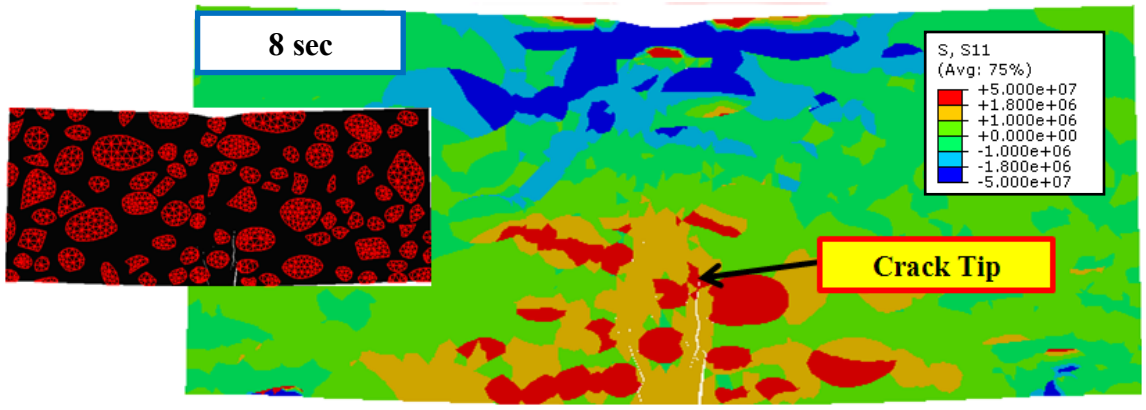
8 sec
S, S11
(Avg: 75%)
+5.000e+07
+1.800e+06
+1.000e+06
+0.000e+00
-1.000e+06
-1.800e+06
-5.000e+07
Crack Tip

(d)

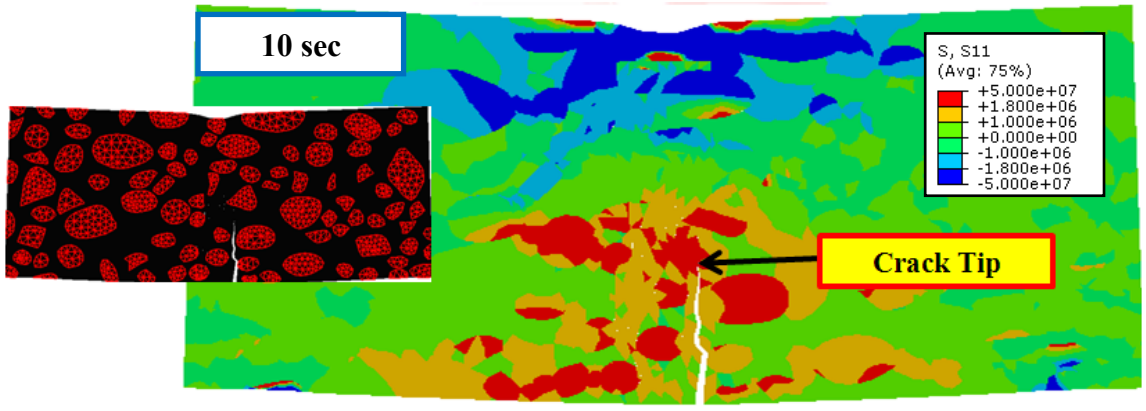
10 sec
S, S11
(Avg: 75%)
+5.000e+07
+1.800e+06
+1.000e+06
+0.000e+00
-1.000e+06
-1.800e+06
-5.000e+07
Crack Tip

(e)

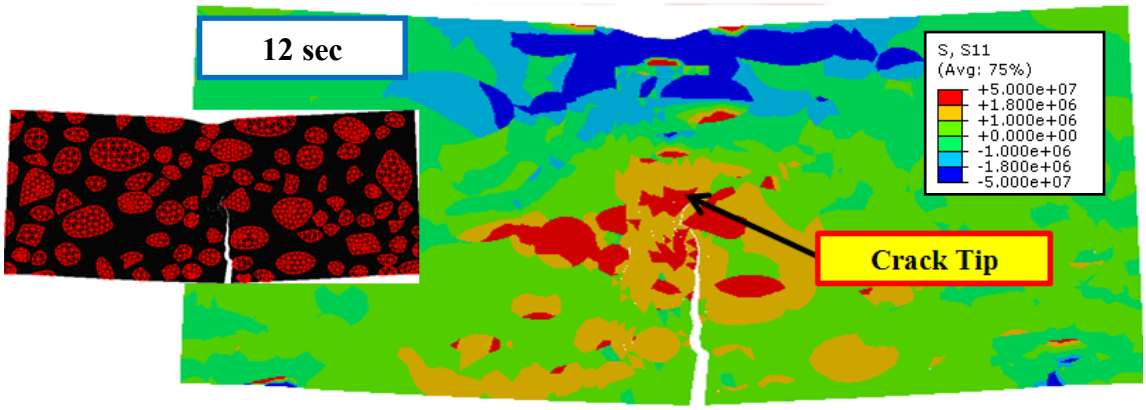
12 sec
S, S11
(Avg: 75%)
+5.000e+07
+1.800e+06
+1.000e+06
+0.000e+00
-1.000e+06
-1.800e+06
-5.000e+07
Crack Tip

(f)

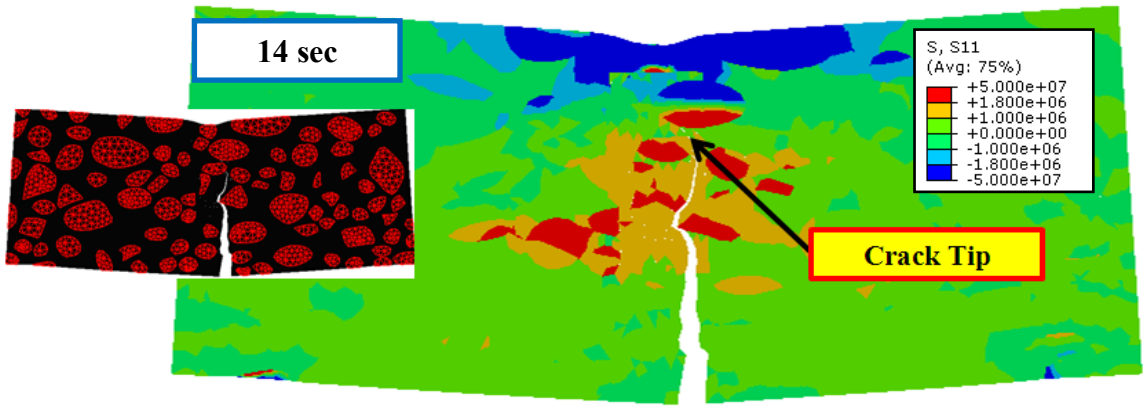

(g)

Figure 44. (a) Virtual beam simulation results demonstrating rate-dependent fracture; and Progressive microstructural fracture and stress (S11) contour plots at: (b) 4 sec; (c) 6 sec; (d) 8 sec; (e) 10 sec; (f) 12 sec; and (g) 14 sec.

7.2.1. Parametric Analysis

The deeper understanding of the effects of small-scale material and mix design properties on the behavior of asphalt mixtures is a fundamental step towards the design of more resistant and long-lasting mixtures. Thus, the primary goal of this research is to develop a computational microstructure modeling framework that will eventually allow researchers and practitioners of the pavement mechanics community to evaluate the effects of component properties and mix design characteristics (some of the key factors directly affecting the quality of the pavement structures) on the mechanical responses of asphalt mixtures.

Among the important variables that affect the mechanical behavior of the mixtures, one can mention volume fraction of aggregate particles. Fracture characteristics of the FAM mixture phase also play a major role on the damage behavior of the mixtures. Thus, this section presents

a sensitivity analysis that illustrates how these parameters affect the overall mechanical behavior of the mixtures.

7.2.2. Rate-Dependent Fracture Properties

The two cohesive fracture parameters that mostly influence the overall mixture responses are the cohesive zone strength and the cohesive fracture energy. Therefore, this section presents sensitivity analysis results for the parameters β_T, β_G, T_{max}^{ref} and G_c^{ref} that define the functions relating cohesive strength and fracture energy to the rate of displacement jumps (see Equations 38 and 39) experienced by each cohesive element in the FEM meshes. For this parametric analysis, the beam shown in Figure 43a was used and the simulations were conducted at a rate of 50 mm/min.

Figure 45 presents the sensitivity of the force-time curve to the four rate-dependent parameters investigated. From the analysis of Figure 45a and 45c, it is clear that as β_T or T_{max}^{ref} increased, the peak load also increased. This was expected because damage initiation is retarded when larger strength values are specified to the cohesive elements. On the other hand, the analysis of Figure 45b and 45d reveals that as β_G or G_c^{ref} increased, the fracture resistance of the mixture also improved, which was demonstrated by the larger area under the force-time curve. This analysis clearly demonstrated that the rate-dependent fracture model developed herein successfully identified the influence of component fracture properties to the overall mixture damage behavior.

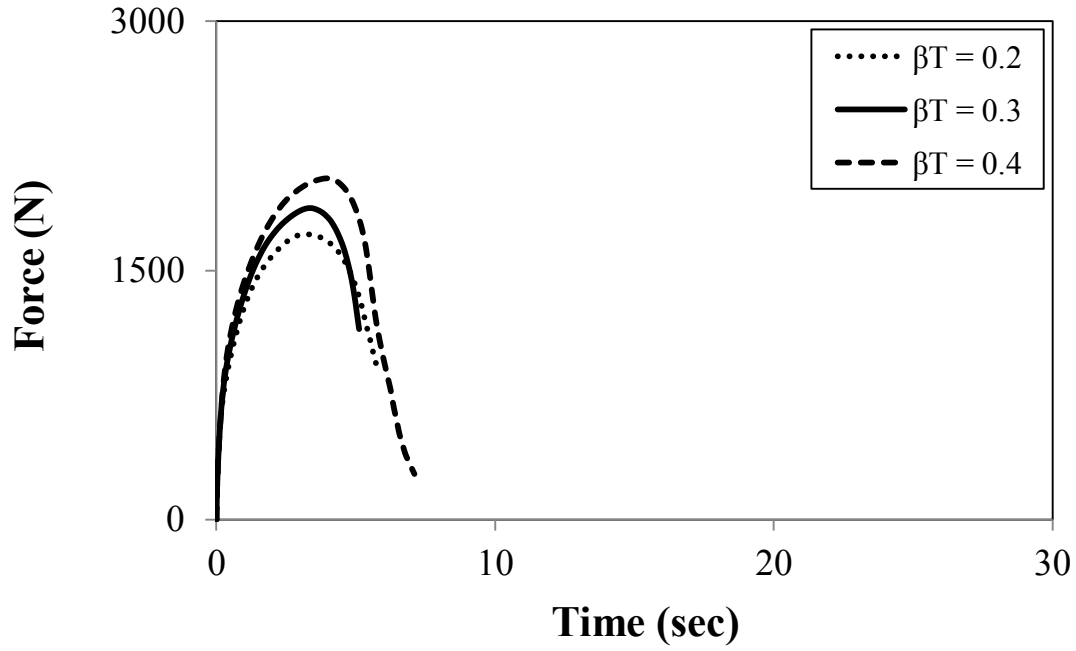
3000
1500
0
Force (N)
0
10
20
30
Time (sec)
βT = 0.2
βT = 0.3
βT = 0.4

(a)

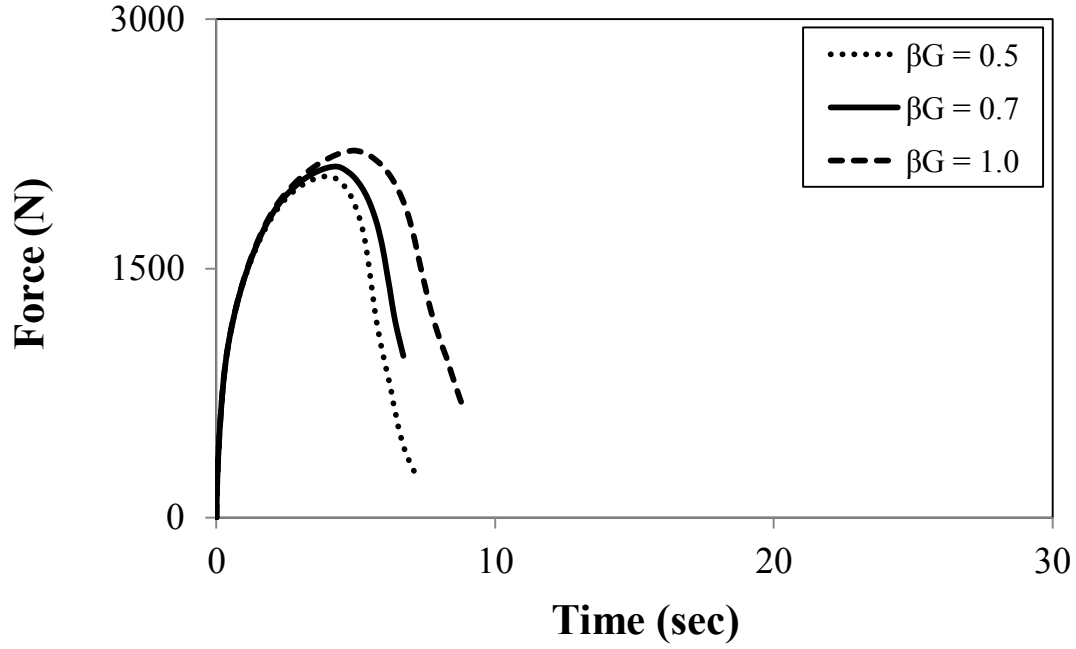
3000
1500
0
Force (N)
0
10
20
30
Time (sec)
βG = 0.5
βG = 0.7
βG = 1.0

(b)

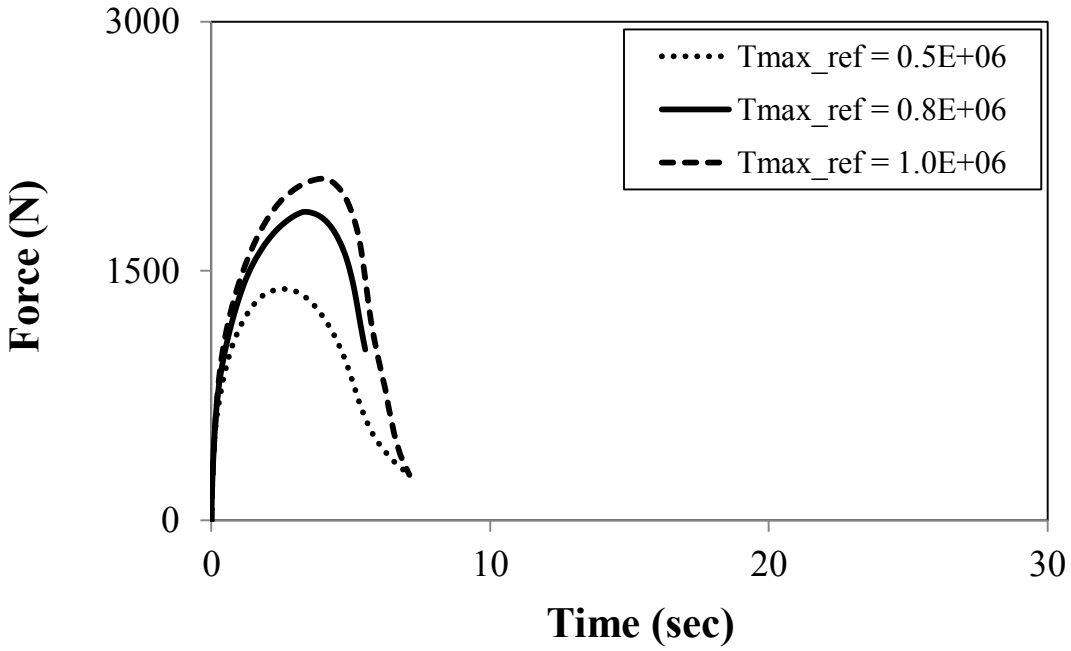

(c)

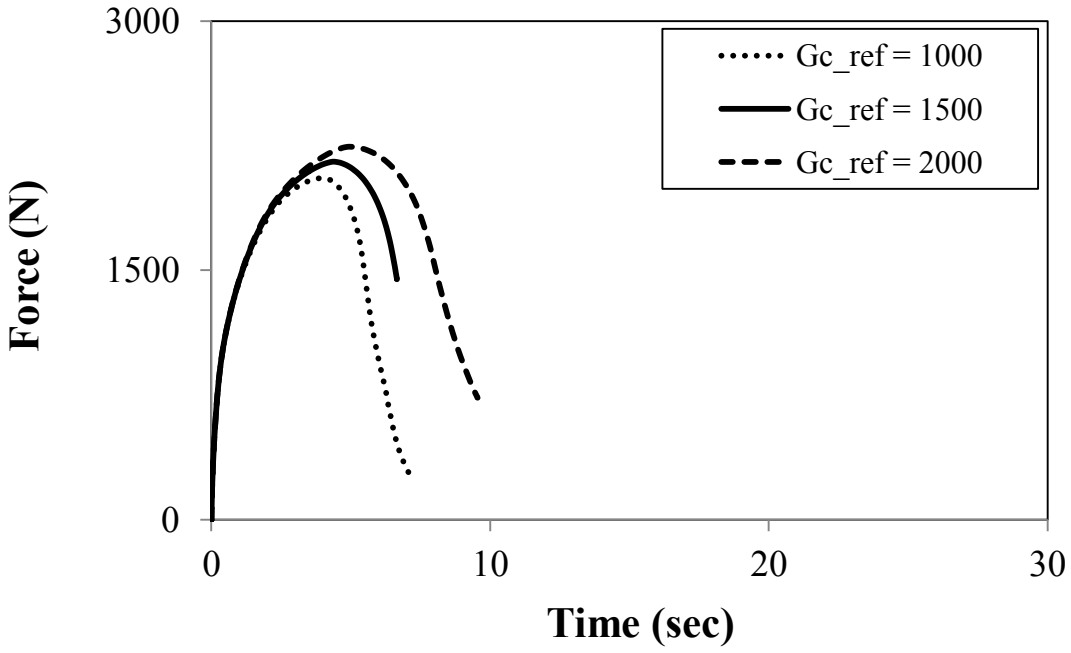

(d)

Figure 45. Parametric analysis for rate-dependent fracture parameters: (a) β_T; (b) β_G; (c) T_{max}^{ref}; and (d) G_c^{ref}.

To further illustrate the effects of the rate-dependent fracture parameters on the fracture behavior of the mixtures, an additional analysis comparing progressive fracture damage levels experienced by the beam at different stages of the simulations was also conducted. Figure 46 shows comparisons for two different T_{max}^{ref}, *i.e.*, 0.5 MPa and 1.0 MPa. As expected, the analysis of Figure 46a and 46b reveals that the beam experienced premature damage initiation for a lower T_{max}^{ref} (0.5 MPa). Damage also propagated faster in the beam when a lower T_{max}^{ref} was assigned, as demonstrated in Figure 46c to 46f. Finally, Figure 47 shows comparisons for two different G_c^{ref}, 1000 J/m^2 and 2000 J/m^2. Damage now initiated at similar simulation stages for both cases, as demonstrated in Figure 47a to 47d. However, as shown in Figure 47e and 47f, after the initiation of damage, crack propagation was much faster for the case with smaller G_c^{ref}, as less energy was required to fully separate the two faces of each cohesive zone element in the mesh.

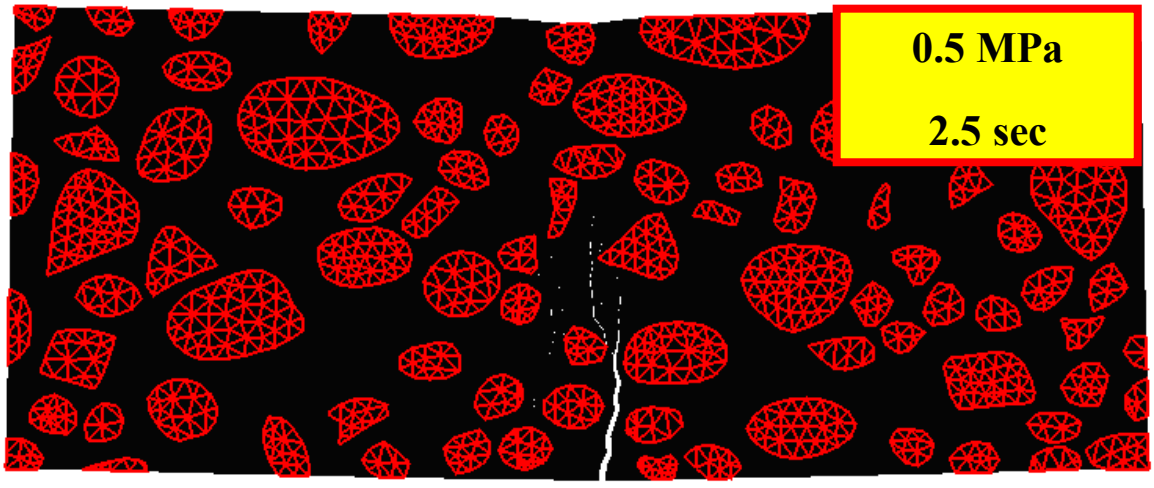

(a)

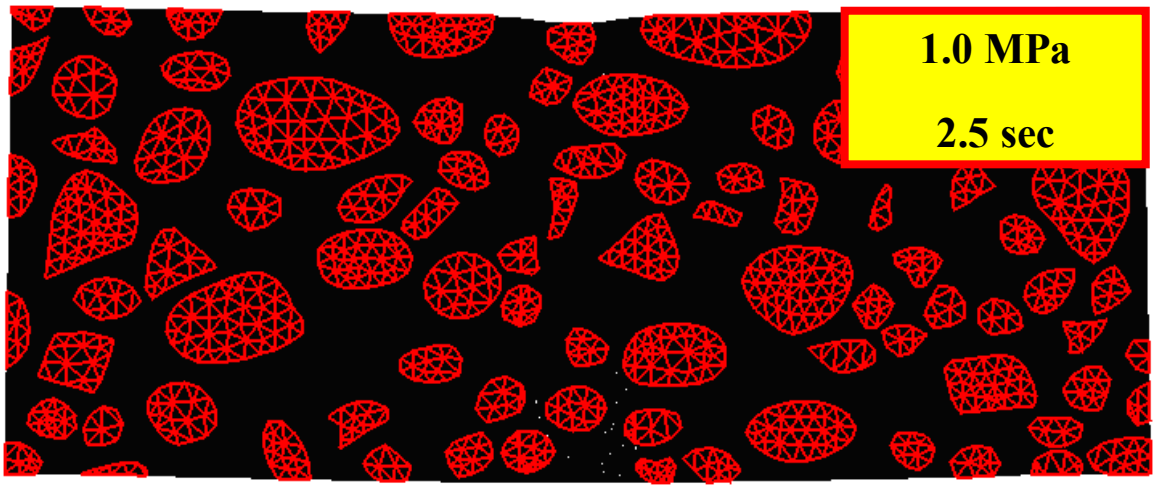

(b)

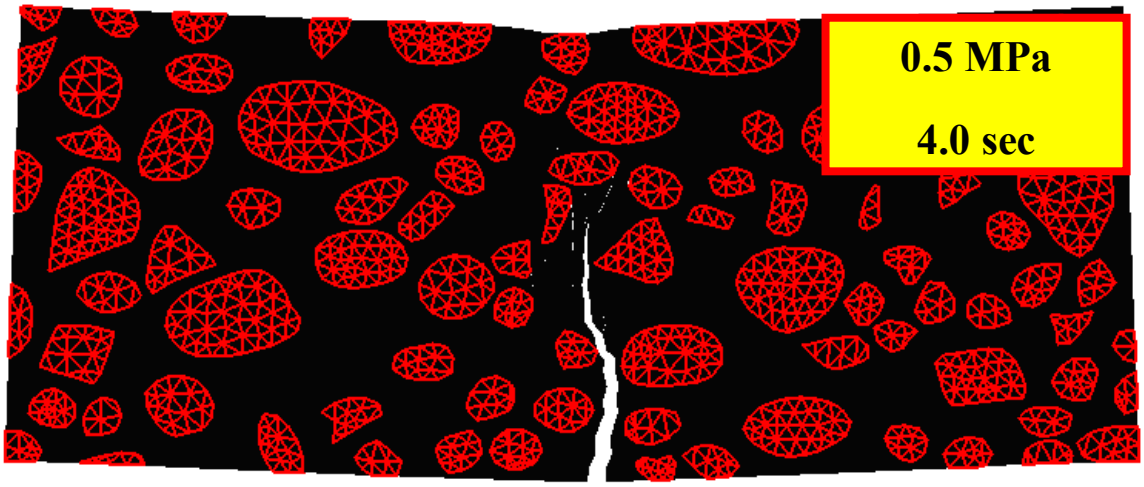

(c)

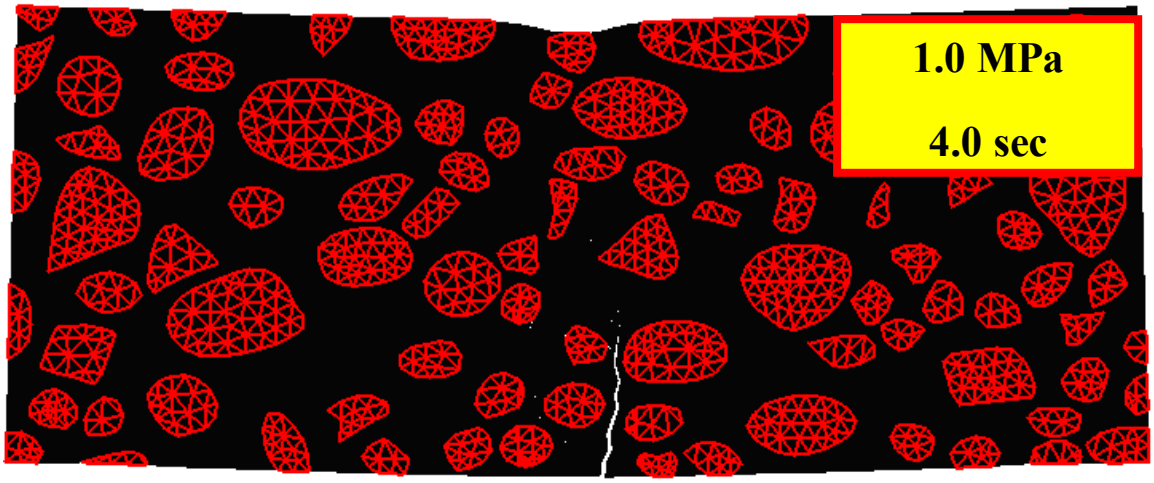

(d)

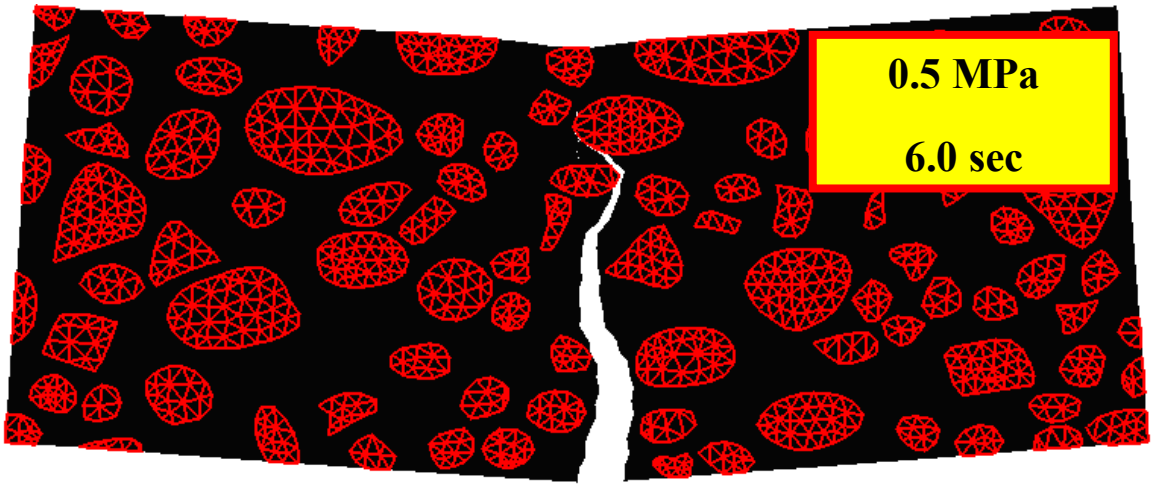

(e)

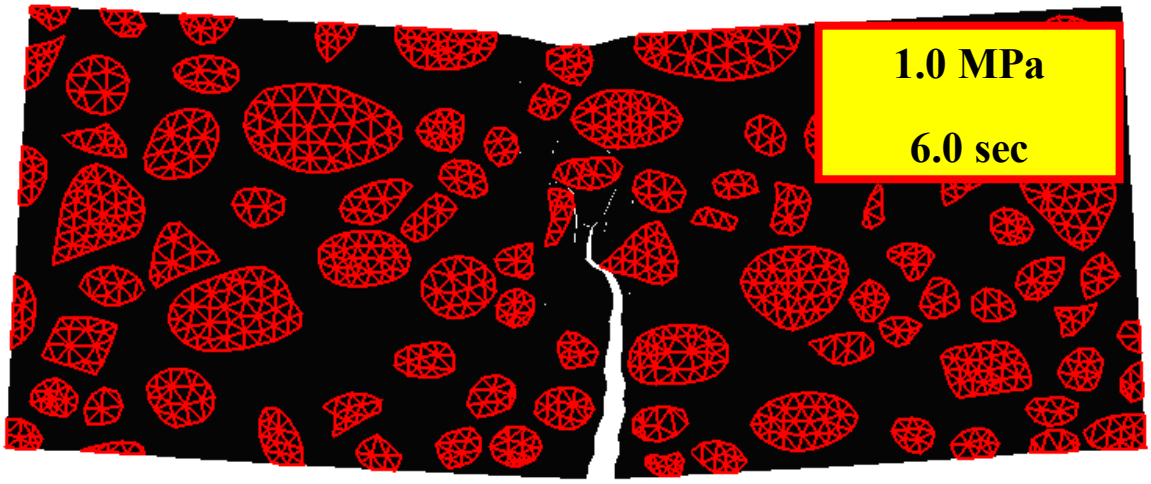

(f)

Figure 46. Progressive microstructural fracture at three simulation times, *i.e.*, 2.5, 4.0, and 6.0 seconds for two different T_{max}^{ref}: (a), (c), and (e) 0.5 MPa; and (b), (d), and (f) 1.0 MPa.

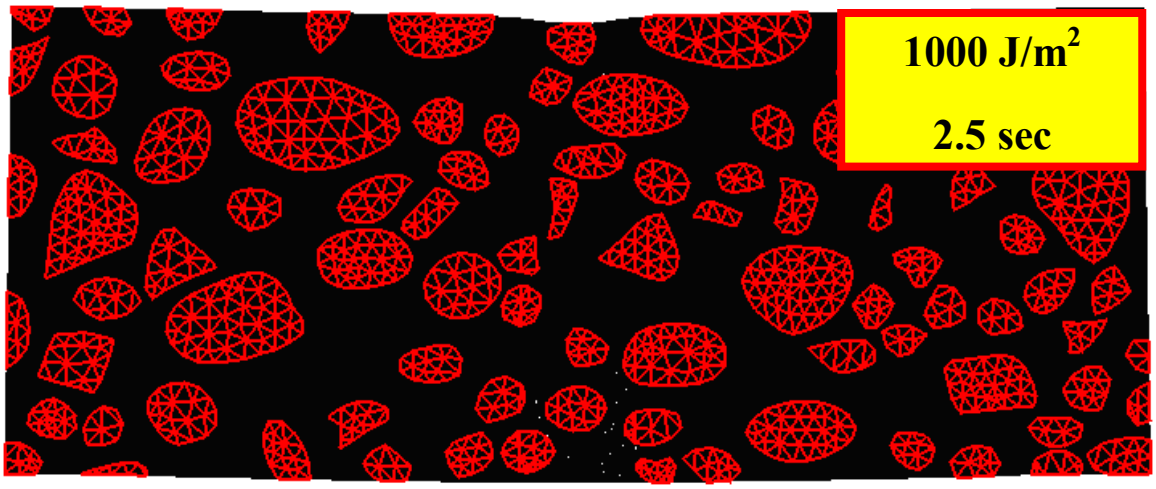

(a)

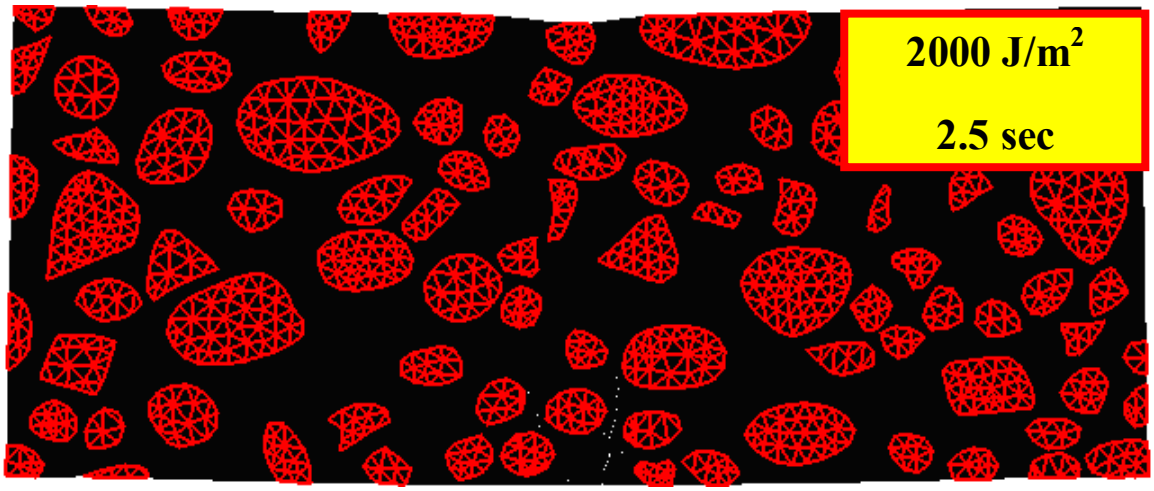

(b)

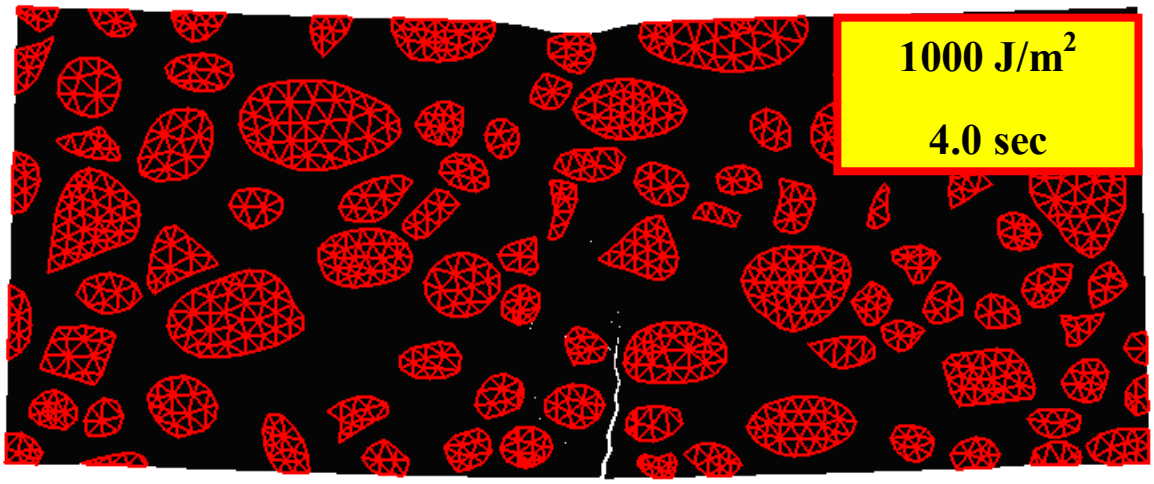

(c)

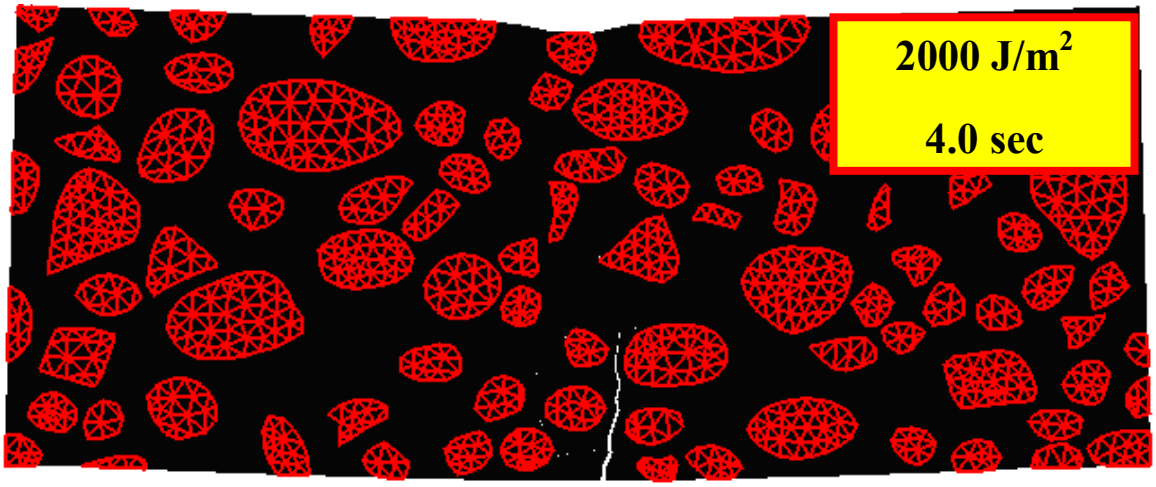

(d)

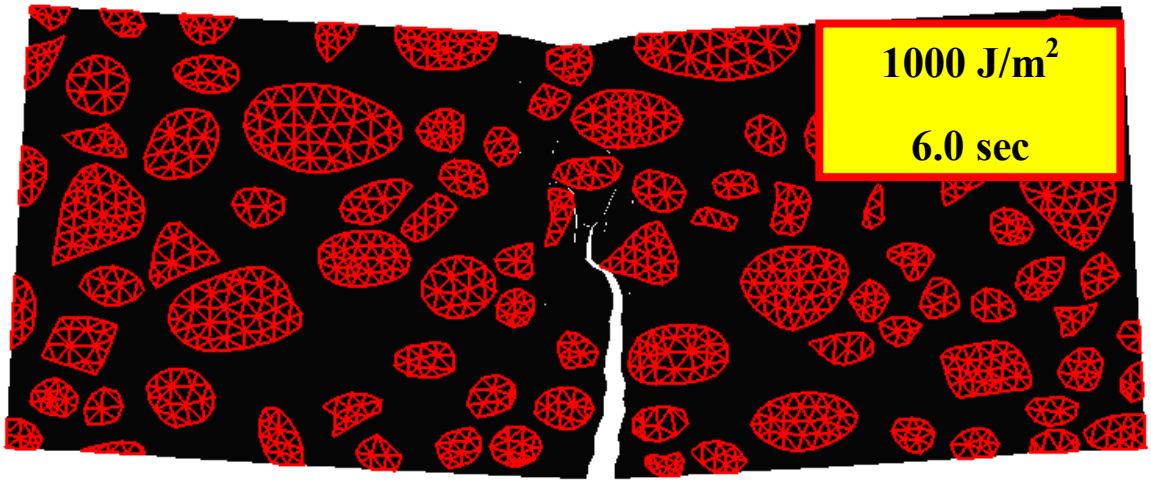

(e)

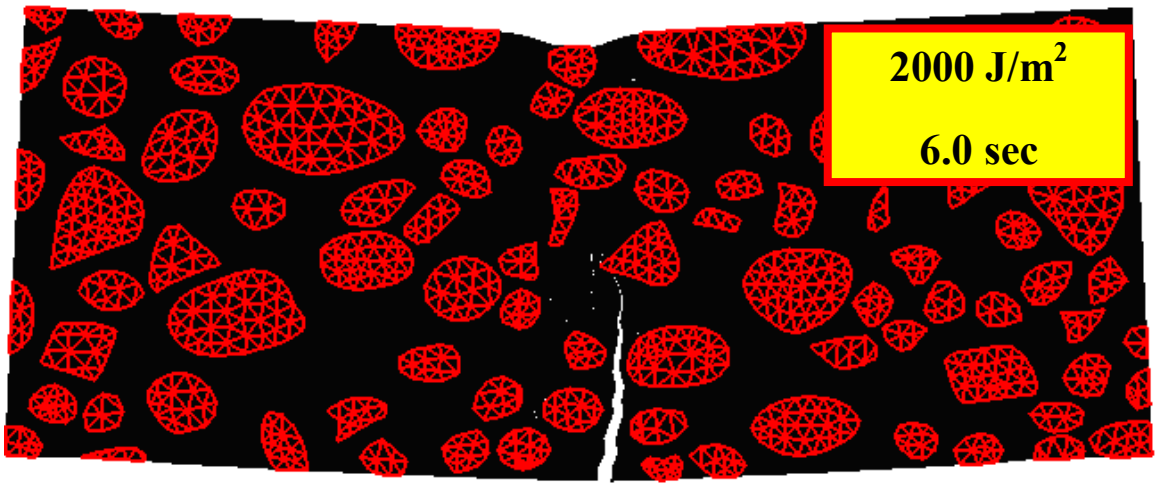

(f)

Figure 47. Progressive microstructural fracture at three simulation times, *i.e.*, 2.5, 4.0, and 6.0 seconds for two different G_c^{ref}: (a), (c), and (e) 1000 J/m^2; and (b), (d), and (f) 2000 J/m^2.

7.2.3. Volumetric Characteristics of Aggregates

Two two-dimensional microstructures of samples of asphalt concrete mixtures were generated to evaluate the effect of volumetric characteristics of aggregate particles on the fracture behavior of HMA mixtures. The microstructures differed on volume fraction of aggregate particles. For the analysis herein, two different values of aggregate volume fraction (qualitatively named as low and high volume fractions) were used to generate the two microstructures.

To simulate the complex geometry of the microstructures, finite-element meshes were generated with triangular elements measuring approximately 1 mm within the central region of the virtual beams and 2 mm outside that region. The objective of the higher refinement level at the central region was to maintain the geometric characteristics (*e.g.*, angularity) of the particles. Additionally, it is important to have a higher refinement level in the regions with higher potential for crack initiation and propagation because the possible crack paths are limited by the topology

of the finite-element mesh. This mesh-dependence problem can be alleviated with the use of more refined meshes close to the evolving crack tips. However, the use of excessively refined meshes may result in very expensive computational cost and may also intensify the problem of artificial compliance that is inherent to intrinsic cohesive models.

The two finite-element meshes generated for the parametric analysis are shown in Figure 48a and 48c. To avoid the effects of the artificial compliance due to the use of an intrinsic cohesive zone model, similar numbers of cohesive elements (2414 and 2170, respectively) were assigned to the meshes. Figure 49 presents the sensitivity of the force-time curve to the volume fraction of aggregate particles. Figure 50 shows snapshots of the virtual beams at a simulation time of 0.54 seconds and illustrates the different levels of microstructural damage experienced by the beams. Figure 50 also shows contour plots of stress tensor component S11. The contours reveal a higher concentration of stress at rigid aggregate particles and around the crack tips.

From Figure 49, it is clear that both initial stiffness and strength of the mixture increased as the volume fraction of aggregates increased (*i.e.*, sample 48a vs. sample 48b). The figure also shows that damage started earlier for the beam with higher concentration of aggregate particles (sample 48a). That was expected because the higher concentration of stiff particles increases the levels of stress in the FAM around the particles. Thus, the cohesive damage initiation criterion is met sooner and macro-cracks form and propagate earlier than they would form and propagate in a sample with fewer particles.

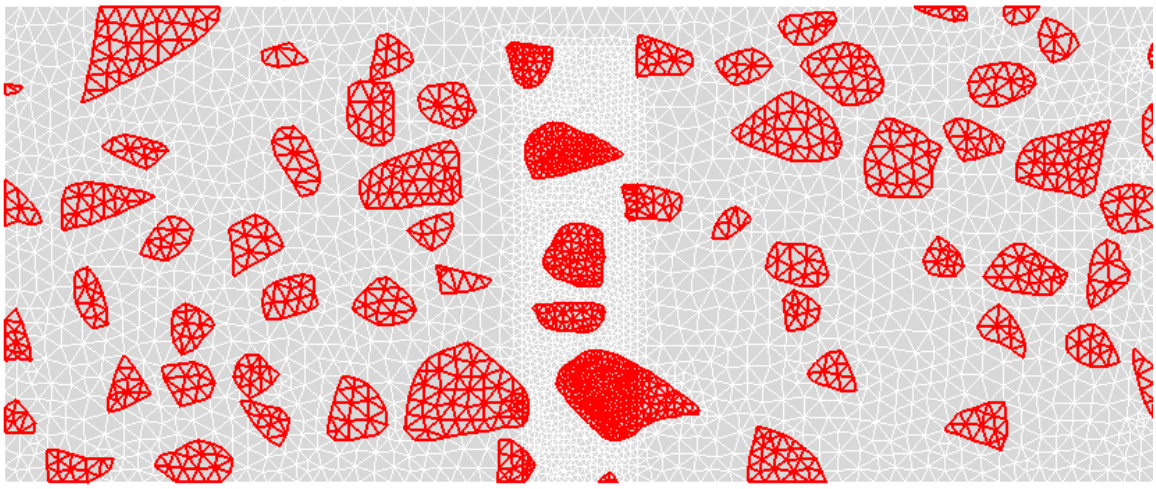

(a)

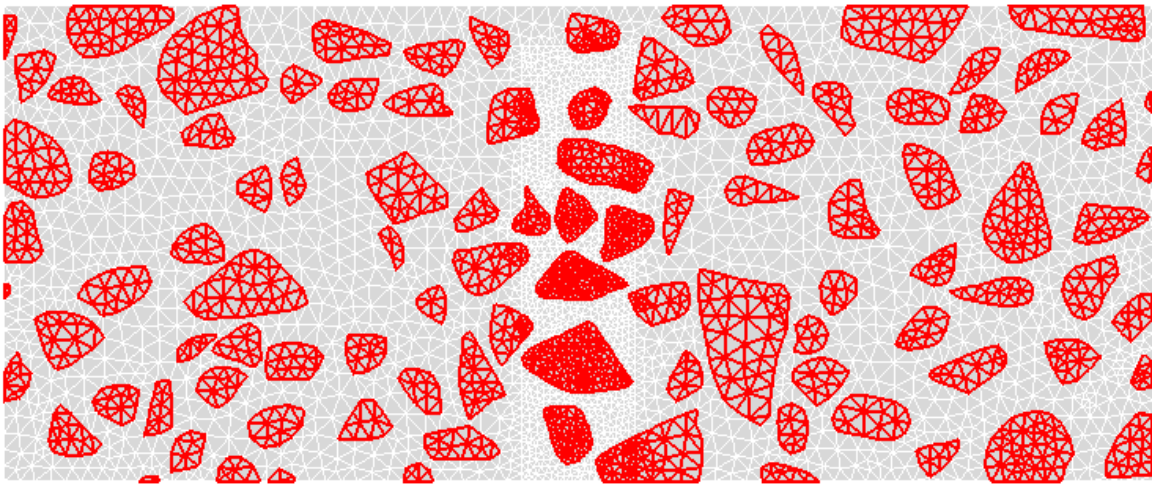

(b)

Figure 48. Parametric analysis - FEM mesh and microstructure of virtual HMA beam samples: (a) Low volume fraction of aggregates and; (b) High volume fraction of aggregates.

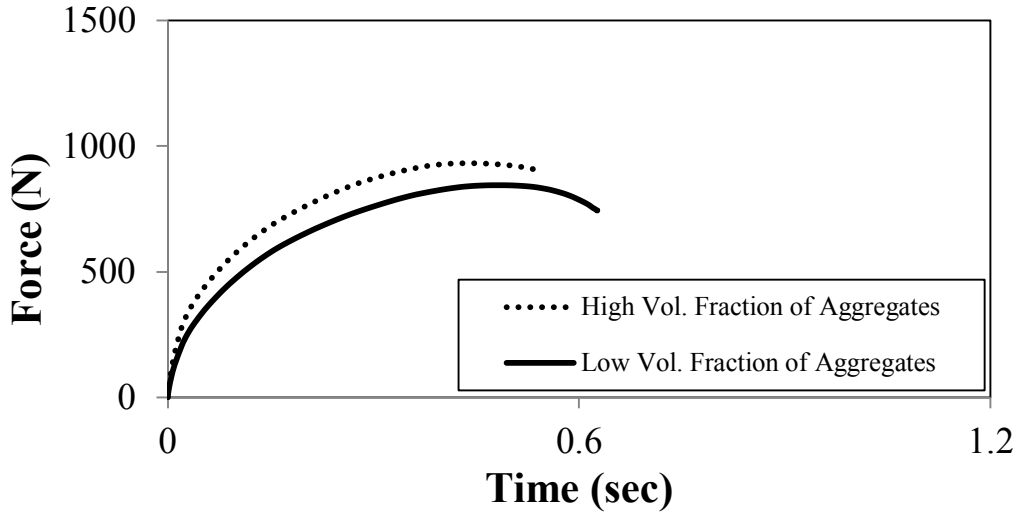

Figure 49. Parametric analysis for volume fraction and angularity of aggregates.

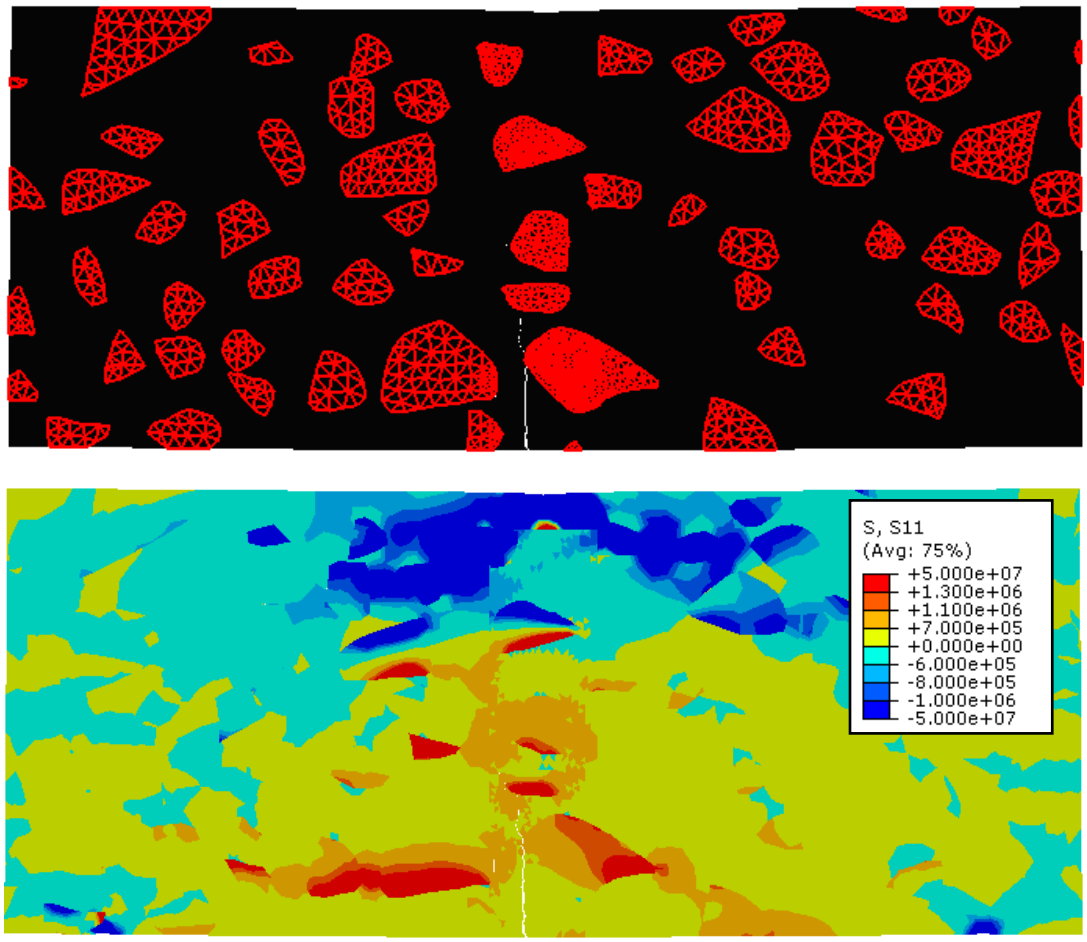

(a)

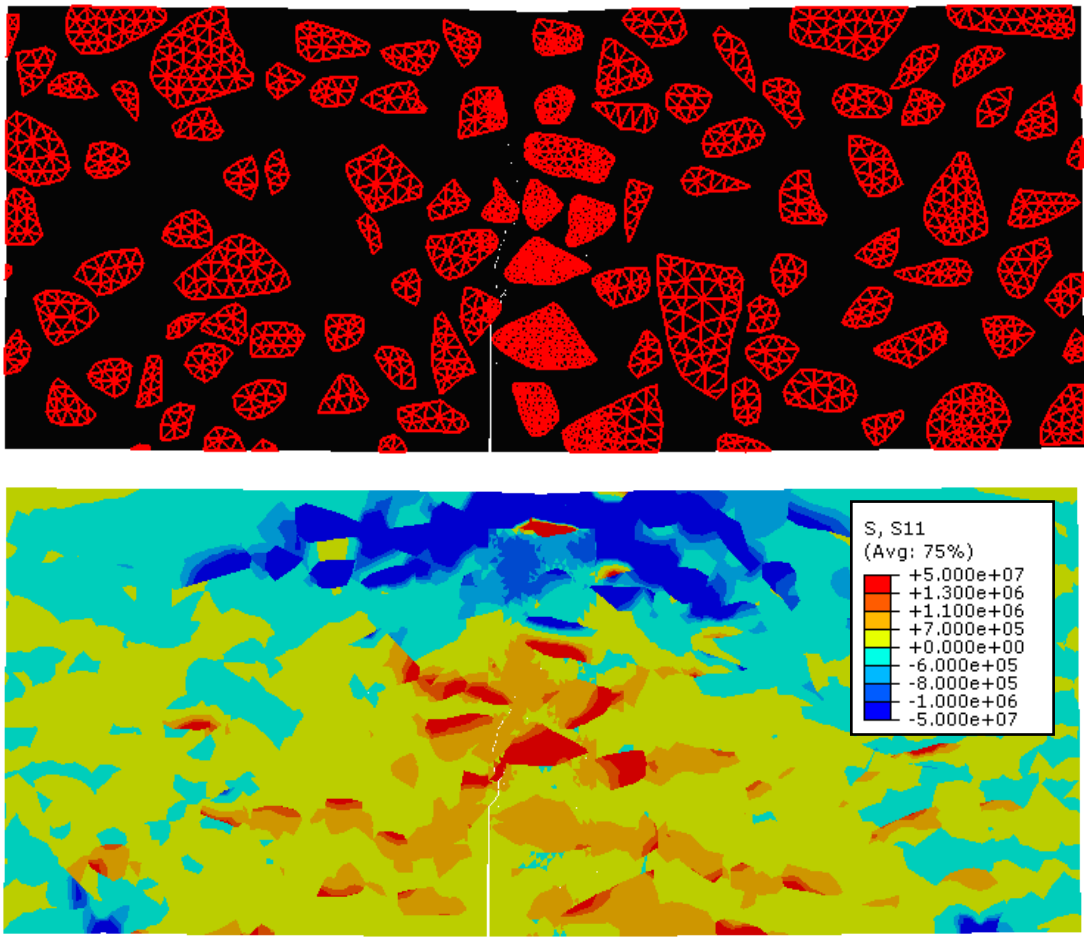

(b)

Figure 50. Virtual beams - microstructural damage and stress contour plots (S11) at simulation time 0.54 seconds.

Chapter 8

Conclusions and Future Work

This study presents the development of a computational microstructure modeling framework that combines laboratory experiments and numerical simulations to predict the mechanical behavior of heterogeneous and inelastic asphalt mixtures that exhibit rate-dependent fracture. The model takes advantage of the microstructural approach in the sense that it only requires material properties of mixture constituents for the simulation of asphalt mixtures. This will eventually result in considerable savings in both time and cost because the model can significantly reduce time-consuming and expensive laboratory performance tests to characterize damage in the mixtures. Another advantage of the computational microstructure modeling approach is that it allows a more comprehensive examination of the microstructural, inelastic material behavior so that stresses and strains within the microstructure can be analyzed more realistically.

HMA mixtures were assumed to be a dual-phase composite comprised of aggregate particles embedded into a phase of FAM. Material properties of the two phases required as inputs for the computational model are obtained from simple and expedited laboratory tests. An image treatment process is used to generate finite element meshes that closely reproduce the geometric characteristics of aggregate particles distributed within the FAM phase.

Using the proposed computational microstructure model, the dynamic modulus of a dense-graded asphalt mixture is predicted. Model predictions are compared to test results and to predictions obtained from other modeling approaches, *i.e.*, the popular model proposed by

Witczak, the modified Hirsch's model (two semi-empirical models) and the analytical micromechanics model by Hashin. The results of the analysis showed that all predicting models investigated in this research were in fair agreement with the test results. In particular, Witczak's equation simulated dynamic moduli somewhat greater than laboratory test results, whereas the modified Hirsh model generally under predicted moduli. The FEM microstructure model presented a relatively higher deviation at lower loading frequencies, but it showed better predictions as the loading frequency was higher. Hashin's analytical micromechanics model showed the worst performance, which was due to the geometric simplifications and assumptions that were made.

Another interesting feature of the model is the consideration of rate-related fracture characteristics of the mixtures, which is a phenomenon that has been reported by other researchers in the open literature and confirmed by simulations of experimental fracture tests performed in a wide range of loading rates. To account for the rate-dependent fracture characteristics of the mixtures, a bilinear rate-independent cohesive zone model was extended to its rate-dependent version and implemented in the form of a user-element (UEL) subroutine that was incorporated into the mainframe of the commercial finite element software ABAQUS. Extra simulations of experimental fracture tests were performed to calibrate the rate-dependent fracture properties. The calibrated rate-dependent properties were used to simulate fracture in general HMA microstructures. A parametric analysis was also conducted to demonstrate the ability of the rate-dependent fracture model to evaluate the effects important mixture parameters such as rate-dependent properties of the FAM phase and volume fraction of aggregate particles on the mechanical behavior of the mixtures.

Further advancements, such as the consideration of air voids as a separate phase, the characterization of mode-dependent fracture properties, and the extension of the two-dimensional model to its three-dimensional version, are required to improve model predictions. Extra work is also required to validate the rate-dependent fracture model. However, the outcomes of this research have demonstrated that a successfully developed model such as the one herein can be an efficient analysis-design tool in that mechanical properties and performance of any macroscopic mixture can be predicted if properties of the mixture constituents and boundary conditions are known and considered. In other words, virtual testing through the model can potentially replace expensive laboratory tests.

References

1. AASHTO T322 (2003). Determining the Creep Compliance and Strength of Hot-Mix Asphalt (HMA) Using the Indirect Tensile Test Device.

2. AASHTO TP62 (2003). Determining Dynamic Modulus of Hot-Mix Asphalt Concrete Mixtures.

3. Abbas, A. M. & Shenoy, A. (2005). Modelling Asphalt Mastic Stiffness Using Discrete Element Analysis and Micromechanics-Based Modes. *International Journal of Pavement Engineering*, 6(2), 137-146.

4. Abbas, A. M., Masad, E., Papagiannakis, T., & Shenoy, A. (2005). Modeling Asphalt Mastic Stiffness Using Discrete Element Analysis and Micromechanics-Based Modes. *International Journal of Pavement Engineering*, 6(2), 137-146.

5. Adamson, R. M., Dempsey, J. P., & Mulmule, S. V. (1996). Fracture Analysis of Semicircular and Semicircular-Bend Geometries. *International Journal of Fracture*, 77(3), 213-222.

6. Alfano, G. & Crisfield, M. A. (2001). Finite Element Interface Models for the Delamination Analysis of Laminated Composites: Mechanical and Computational Issues. *International Journal for Numerical Method in Engineering, 50*, 1701–1736.

7. Allen, D. H. & Searcy, C. R. (2001). A Micromechanical Model for a Viscoelastic Cohesive Zone. *International Journal of Fracture,* 107, 159-176.

8. Allen, D. H., Jones, R. H., & Boyd, J. G. (1994). Micromechanical Analysis of a Continuous Fiber Metal Matrix Composite Including the Effects of Matrix Viscoplasticity and Evolving Damage. *Journal of Mechanics and Physics of Solids,* 42 (3), 505-529.

9. Andrei, D., Witczak, M. W., & Mirza, M. W. (1999). Development of a Revised Predictive Model for the Dynamic Complex Modulus of Asphalt Mixtures. *NCHRP 1-37, an Interim Report,* University of Maryland, College Park, MD.

10. Aragão, F. T. S., Kim, Y. R., Lee, J., & Allen, D. H. (2011). Micromechanical Model for Heterogeneous Asphalt Concrete Mixtures Subjected to Fracture Failure. *Journal of Materials in Civil Engineering (Issue: Multiscale and Micromechanical Modeling of Asphalt Mixes)*, 23, No. 1, pp. 30-38.

11. Aragão, F. T. S. & Kim, Y. R. (2011). Characterization of Fracture Properties of Asphalt Mixtures Based on Cohesive Zone Modeling and Digital Image Correlation Technique. *In Transportation Research Board, TRB* (electronic version), National Research Council, Washington, D.C.

12. Aragão, F. T. S. & Kim, Y. R. (2010). Modeling Fracture and Failure of Heterogeneous and Inelastic Asphaltic Materials Using the Cohesive Zone Concept and the Finite Element Method. *In Proceedings of the 2010 ASCE GeoFlorida Congress: Advances in Analysis, Modeling & Design*. West Palm Beach, FL, 2662-2671.

13. Aragão, F. T. S., Kim, Y. R., Karki, P., & Little, D. N. (2010). Semi - Empirical, Analytical, and Computational Predictions of Dynamic Modulus of Asphalt Concrete

Mixtures. *In Transportation Research Record: Journal of the Transportation Research Board, No. 2181*, *TRB*, National Research Council, Washington, D. C., 19-27.

14. Aragão, F. T. S., Kim, Y. R., Lee, J., & Soares, J. B. (2009a). A Micromechanical Model for Predicting the Dynamic Modulus of Heterogeneous and Rate-Dependent Asphalt Concrete Mixtures. *In Proceedings of the IV Simpósio Internacional de Avaliação de Pavimentação e Projetos de Reforço*. Fortaleza, Brazil.

15. ASTM (1979). ASTM-D3497-79 - Test method for dynamic modulus of asphalt concrete mixtures.

16. ASTM E399 (2008). Standard Test Method for Linear-Elastic Plane-Strain Fracture Toughness KIC of Metallic Materials.

17. Barenblatt, G. I. (1962). Mathematical Theory of Equilibrium Cracks in Brittle Fracture. *Advances in Applied Mechanics, 7*, 55-125.

18. Barenblatt, G. I. (1959). The Formation of Equilibrium Cracks During Brittle Fracture. General Ideas and Hypothesis. Axially-Symmetric Cracks. *Journal of Applied Mathematics and Mechanics, 23* (3), 622-636.

19. Bari, J. & Witczak, M. W. (2006). Development of A New Revised Version of the Witczak E* Predictive Model for Hot Mix Asphalt Mixtures. *Journal of the Association of Asphalt Paving Technologists*, 75, 381-423.

20. Barksdale, R. D. (1993). The aggregate handbook. *National Stone Association*, Washington, D.C.

21. Basham, K. D., Chong, K. P., & Boseri, A. P. (1990). A New Development in Devising Tension-Softening Curves for Brittle Materials. *In Proceedings of the Ninth International Conference on Experimental Mechanics*, Copenhagen, Denmark, 1423-1432.

22. Buttlar, W. & You, Z. (2001). Discrete Element Modeling of Asphalt Concrete: Microfabric Approach. *In Transportation Research Record: Journal of the Transportation Research Board, No. 1757*, *TRB*, National Research Council, Washington, D. C., 111-118.

23. Buttlar, W. G., Bozkurt, D., Al-Khateeb, G., & Waldhoff, A. S. (1999). Understanding Asphalt Mastic Behavior through Micromechanics. *In Transportation Research Record: Journal of the Transportation Research Board, No. 1681*, *TRB*, National Research Council, Washington, D. C., 157-169.

24. Camacho, G. & Ortiz, M. (1996). Computational Modeling of Impact Damage in Brittle Materials. *International Journal of Solids and Structures, 33*, 2899-2938.

25. Ceylan, H., Schwartz, C. W., Kim, S, & Gopalakrishnan, K. (2009). Accuracy of Predictive Models for Dynamic Modulus of Hot-Mix Asphalt. *Journal of Materials in Civil Engineering*, 286-293.

26. Chandra, N., Li, H., Shet, C., & Ghonem, H. (2002). Some Issues in the Application of Cohesive Zone Models for Metal-Ceramic Interfaces. *International Journal of Solids and Structures, 39*, 2827-2855.

27. Chong, K. P. & Kuruppu, M. D. (1984). New Specimen for Fracture Toughness Determination for Rock and Other Materials. *International Journal of Fracture*, 26, R59-R62.

28. Christensen Jr., D. W., Pellinen, T., & Bonaquist, R. F. (2003). Hirsch Model for Estimating the Modulus of Asphalt Concrete. *Journal of the Association of Asphalt Paving Technologists*, 72, 97-121.

29. Christensen, R. M. (1969). Viscoelastic Properties of Heterogeneous Media. *Journal of Mechanics and Physics of Solids*, *17*, 23-41.

30. Dai, Q. & You, Z. (2007). Micromechanical Finite Element Framework for Predicting Viscoelastic Properties of Asphalt Mixtures. *Materials and Structures*, 41, 1025-1037.

31. Dai, Q., Sadd, M. H., & You, Z. (2006). A Micromechanical Finite Element Model for Linear and Damage-Coupled Viscoelastic Behaviour of Asphalt Mixture. *International Journal for Numerical and Analytical Methods in Geomechanics*, 1135-1158.

32. Dai, Q., Sadd, M. H., Parameswaran, V., & Shukla, A. (2005). Prediction of Damage Behaviors in Asphalt Materials Using a Micromechanical Finite-Element Model and Image Analysis. *Journal of Engineering Mechanics*, 131(7), 668-677.

33. Dugdale, D. (1960). Yielding of Steel Sheets Containing Slits. *Journal of Mechanics and Physics of Solids, 8* (2), 100-104.

34. Einstein, A. (1906). Eine Neue Bestimmung der Molekuldimensionen. *Ann. Phys*., 19, 289.

35. Espinosa, H. D. & Zavattieri, P. D. (2003). A Grain Level Model for the Study of Failure Initiation and Evolution in Polycrystalline Brittle Materials, Part I: Theory and Numerical Implementation. *Mechanics of Materials,* 35 (3-6), 333-364.

36. Espinosa, H., Dwivedi, S., & Lu, H. C. (2000). Modeling Impact Induced Delamination of Woven Fiber Reinforced Composites with Contact/Cohesive Laws. *Computer Methods in Applied Mechanics and Engineering, 183* (3-4), 259-290.

37. Freitas, F. A. C. (2007). A Theoretical and Experimental Technique to Measure Fracture Properties in Viscoelastic Solids. *Ph.D. Dissertation Approved by the Graduate Committee of the University of Nebraska - Lincoln*. Lincoln, NE.

38. Freitas, F. A. C., Kim, Y. R., Allen, D. H., & Aragão, F. T. S. (2007). A Theoretical and Experimental Technique to Characterize Fracture in Asphalt Mixtures and Pavements. *In Transportation Research Board, TRB* (CD-ROM), National Research Council, Washington, D.C.

39. Geubelle, P. & Baylor, J. (1998). Impact-Induced Delamination of Laminated Composites: A 2D Simulation. *Composites Part B - Engineering, 29* (5), 589-602.

40. Guddati, M. M., Feng, Z., & Kim, Y. R. (2002). Toward a Micromechanics-Based Procedure to Characterize Fatigue Performance of Asphalt Concrete. *In Transportation Research Record: Journal of the Transportation Research Board, No. 1789*, *TRB*, National Research Council, Washington, D. C., 121-128.

41. Hashin, Z. (1965). Viscoelastic Behavior of Heterogeneous Media. *Journal of Applied Mechanics*, 630-636.

42. Hashin, Z. (1962). The Elastic Moduli of Heterogeneous Materials. *Journal of Applied Mechanics*, 143-150.

43. Hibbit, Karlsson, & Sorenson. (2008). ABAQUS User's Manual Version 6.8.

44. Hirsch, T. J. (1962). Modulus of Elasticity of Concrete Affected by Elastic Moduli of Cement Paste Matrix and Aggregate. *Journal of the American Concrete Institute*, 59 (3), 427-452.

45. Huang, B., Shu, X., & Li, G. (2007). Analytical Modeling of Three-Layered HMA Mixtures. *International Journal of Geomechanics*, 7(2), 140-148.

46. Hutchinson, J. & Evans, A. (2000). Mechanics of Materials: Top-Down Approaches to Fracture. *Acta Materialia , 48* (1), 125-135.

47. Jeng, Y. S. & Perng, J. D. (1991). Analysis of Crack Propagation in Asphalt Concrete Using Cohesive Crack Model. *In Transportation Research Record: Journal of the Transportation Research Board, No. 1317*, *TRB*, National Research Council, Washington, D. C., 90-99.

48. Jeng, Y. S., Liaw, C., & Liu, P. (1993). Analysis of Crack Resistance of Asphalt Concrete Overlays - A Fracture Mechanics Approach. *In Transportation Research Record: Journal of the Transportation Research Board, No. 1388*, *TRB*, National Research Council, Washington, D. C., 160-166.

49. Karki, P. (2010). Computational and Experimental Characterization of Bituminous Composites Based on Experimentally Determined Properties of Constituents. *Master's*

Thesis Approved by the Graduate Committee of the University of Nebraska - Lincoln. Lincoln, NE.

50. Khanna, S. K., Ranganathan, P., Yedla, S. B., Winter, R. M., & Paruchuri, K. (2003). Investigation of Nanomechanical Properties of the Interphase in a Glass Fiber Reinforced Polyester Composite Using Nanoindentation. *Journal of Engineering Materials and Technology*, 90-96.

51. Khalid, H. A. & Artamendi, I. (2008). Measurement and Effective Evaluation of Crack Growth in Asphalt Mixtures. Pavement Cracking: Mechanisms, Modeling, Detection, Testing, and Case Histories, edited by I. L. Al-Qadi, T. Scarpas, and A. Loizos, CRC Press, 417-425.

52. Kim, Y. R., Aragão, F. T. S., Allen, D. H., & Little, D. N. (2010). Damage Modeling of Bituminous Mixtures Considering Mixture Microstructure, Viscoelasticity, and Cohesive Zone Fracture. *Canadian Journal of Civil Engineering*, 37, 1125-1136.

53. Kim, H. & Buttlar, W. G. (2009). Finite Element Cohesive Fracture Modeling of Airport Pavements at Low Temperatures. *Cold Regions Science and Technology*, 57, 123-130.

54. Kim, H., Wagoner, M. P., & Buttlar, W. G. (2009). Micromechanical Fracture Modeling of Asphalt Concrete Using a Single-Edge Notched Beam Test. *Materials and Structures*, 42, 677- 689.

55. Kim, Y. R., Allen, D. H., & Little, D. N. (2007). Computational Constitutive Model for Predicting Nonlinear Viscoelastic Damage and Fracture Failure of Asphalt Concrete Mixtures. *International Journal of Geomechanics*, 7 (2), 102-110.

56. Kim, Y. R., Allen, D. H., & Little, D. N. (2006a). Computational Model to Predict Fatigue Damage Behavior of Asphalt Mixtures under Cyclic Loading. *In Transportation Research Record: Journal of the Transportation Research Board, No. 1970*, *TRB*, National Research Council, Washington, D. C., 196-206.

57. Kim, Y. R., Lee, H. J., Little, D. N., & Kim, Y. R. (2006b). A Simple Testing Method to Evaluate Fatigue Fracture and Damage Performance of Asphalt Mixtures. *Journal of the Association of Asphalt Paving Technologists*, 755-787.

58. Kim, Y. R., Allen, D. H., & Little, D. N. (2005). Damage-Induced Modeling of Asphalt Mixtures through Computational Micromechanics and Cohesive Zone Fracture. *Journal of Materials in Civil Engineering*, 477-484.

59. Kim, H. & Buttlar, W. G. (2005). Micromechanical Fracture Modeling of Hot-Mix Asphalt Concrete Based on a Disk-Shaped Compact Tension Test. *Electronic Journal of the Association of Asphalt Paving Technologists*, 74E.

60. Kim, Y. R. & Seo, Y. K. (2004). Dynamic Modulus Testing of Asphalt Concrete in Indirect Tension Mode. *In Transportation Research Record: Journal of the Transportation Research Board, No. 1970*, *TRB*, National Research Council, Washington, D. C., 163-173.

61. Kim, Y. R. & Little, D. N. (2004). Linear Viscoelastic Analysis of Asphalt Mastics. *Journal of Materials in Civil Engineering*, 122-132.

62. Kim, Y. R., Little, D. N., & Lytton, R. L. (2003). Fatigue and Healing Characterization of Asphalt Mixtures. *Journal of Materials in Civil Engineering*, 15(1), 75-83.

63. Klein, P., Foulk, J., Chen, E., Wimmer, S., & Gao, H. (2001). Physics-Based Modeling of Brittle Fracture: Cohesive Formulations and the Application of Meshfree Methods. *Technical Report SAND2001-8099*, Sandia National Laboratories.

64. Li, X. & Marasteanu, M. O. (2004). Evaluation of the Low Temperature Fracture Resistance of Asphalt Mixtures Using the Semi Circular Bend Test. *Journal of the Association of Asphalt Paving Technologists*, 73, 401-426.

65. Li, X. & Marasteanu, M. O. (2010). Using Semi Circular Bending Test to Evaluate Low Temperature Fracture Resistance for Asphalt Concrete. *Experimental Mechanics*, 50, 867-876.

66. Lim, I. L., Johnston, I. W., Choi, S. K., & Boland, J. N. (1994). Fracture Testing of Soft Rock with Semicircular Specimens Under Three-Point Bending, Part 2 - Mixed-Mode. *Int. J. Rock Mech. Min. Sci.*, 31(3), 199-212.

67. Mohammed, I. & Liechti, K. (2000). Cohesive Zone Modeling of Crack Nucleation at Bimaterial Corners. *Journal of the Mechanics and Physics of Solids, 48*, 735-764.

68. Marasteanu, M. O., Dai, S. T., Labuz, J. F., & Li, X. (2002). Determining the Low-Temperature Fracture Toughness of Asphalt Mixtures. *In Transportation Research Record: Journal of the Transportation Research Board, No. 1789*, *TRB*, National Research Council, Washington, D. C., 191-199.

69. Marzi, S., Hesebeck, O., Brede, M., & Kleiner, F. (2009). A Rate-Dependent Cohesive Zone Model for Adhesively Bonded Joints Loaded in Mode I. *Journal of Adhesion Science and Technology*, 23, 881-898.

70. Masad, E., Niranjanan, S., Bahia, H., & Kose, S. (2001). Modeling and Experimental Measurements of Localized Strain Distribution in Asphalt Mixes. *Journal of Transportation Engineering*, ASCE, 127(6), 477-485.

71. Masad, E., Muhunthan, B., Shashidhar, & Harman, T. (1999a). Internal Structure Characterization of Asphalt Concrete Using Image Analysis. *Journal of Computing in Civil Engineering (Special Issue on Image Processing)*, 13 (2), 88-95.

72. Masad, E., Muhunthan, B., Shashidhar, & Harman, T. (1999b). Quantifying Laboratory Compaction Effects on the Internal Structure of Asphalt Concrete. *In Transportation Research Record: Journal of the Transportation Research Board, No. 1681*, *TRB*, National Research Council, Washington, D. C., 179-185.

73. Masad, E., Tashman, L., Little, D., & Zbib, H. (2005). Viscoplastic Modeling of Asphalt Mixes with the Effects of Anisotropy, Damage and Aggregate Characteristics. *Journal of Mechanics of Materials*, 37(12), 1242-1256.

74. Masad, E., Tashman, L., Somedavan, N., & Little, D. (2002). Micromechanics-Based Analysis of Stiffness Anisotropy in Asphalt Mixtures. *Journal of Materials in Civil Engineering*, 14 (5), 374-383.

75. Miller, O., Freund, L., & Needleman, A. (1999). Modeling and Simulation of Dynamic Fragmentation in Brittle Materials. *International Journal of Fracture, 96* (2), 101-125.

76. Mobasher, B. M., Mamlouk, M. S., & Lin, H. M. (1997). Evaluation of Crack Propagation Properties of Asphalt Mixtures. *Journal of Transportation Engineering*, 123(5), 405-413.

77. Mohammad, L. N. & Kabir, M. D. (2008). Evaluation of Fracture Properties of Hot Mix Asphalt. *Pavement Cracking: Mechanisms, Modeling, Detection, Testing, and Case Histories*, edited by I. L. Al-Qadi, T. Scarpas, and A. Loizos, CRC Press, 427-436.

78. Molenaar, A. A. A, Scarpas, A., Liu, X., & Erkens, S. M. J. G. (2002). Semicircular Bending Test, Simple but Useful? *Journal of the Association of Asphalt Paving Technologists*, 71, 794-815.

79. Mota, A., Knap, J., & Ortiz, M. (2008). Fracture and Fragmentation of Simplicial Finite Element Meshes Using Graphs. *International Journal for Numerical Methods and Engineering, 73*, 1547-1570.

80. Needleman, A. (1990a). An Analysis of Decohesion Along an Imperfect Interface. *International Journal of Fractur*e, 42, 21–40.

81. Needleman, A. (1990b). An Analysis of Tensile Decohesion Along an Interface. *Journal of Mechanics and Physics of Solids,* 38 (3), 289-324.

82. Needleman, A. (1987). A Continuum Model for Void Nucleation by Inclusion Debonding. *Journal of Applied Mechanics,* 54, 525-531.

83. NCHRP (2004). Guide for Mechanistic-Empirical Design of New and Rehabilitated Pavement Structures. *Final Report of Project No. 1-37*.

84. Nguyen, T. D., S. Govindjee, P. A. Klein, & H. Gao. (2004). A Rate-Dependent Cohesive Continuum Model for the Study of Crack Dynamics. *Computer Methods in Applied Mechanics and Engineering*, 193, 3239-3265.

85. Oliver, W. C. & Pharr, G. M. (1992). An Improved Technique for Determining Hardness and Elastic Modulus Using Load and Displacement Sensing Indentation Experiments. *J. Mater. Res.*, 7(6), 1564-1583.

86. Ortiz, M. & Pandolfi, A. (1999). Finite-Deformation Irreversible Cohesive Elements for Three-Dimensional Crack Propagation Analysis. *International Journal for Numerical Methods in Engineering*, 44 (9), 1267-1282.

87. Pandolfi, A. & Ortiz, M. (2002). An Efficient Adaptive Procedure for Three-Dimensional Fragmentation Simulations. *Engineering with Computers, 18*, 148-159.

88. Pandolfi, A. & Ortiz, M. (1998). Solid Modeling Aspects of Three-Dimensional Fragmentation. *Engineering with Computers*, *14* (4), 287-308.

89. Papagiannakis, A. T., Abbas, A., & Masad, E. (2002). Micromechanical Analysis of Viscoelastic Properties of Asphalt Concretes. *In Transportation Research Record: Journal of the Transportation Research Board, No. 1789*, *TRB*, National Research Council, Washington, D. C., 113-120.

90. Papoulia, K. D., Sam, C. H., & Vavasis, S. A. (2003). Time Continuity in Cohesive Finite Element Modeling. *International Journal for Numerical Methods in Engineering, 58*, 679-701.

91. Park, K., Paulino, G. H., & Roesler, J. (2010). Cohesive Fracture Model for Functionally-Graded Fiber Reinforced Concrete. *Cement and Concrete Research*, 40 (6), 956-965.

92. Paulino, G. H., Song, S. H., & Buttlar, W. G. (2004). Cohesive Zone Modeling of Fracture in Asphalt Concrete. *Proceedings of the fifth RILEM international conference on cracking in pavements: mitigation, risk assessment and prevention*, 63-70.

93. Rahulkumar, P., Jagota, A., Bennison, S., & Saigal, S. (2000). Cohesive Element Modeling of Viscoelastic Fracture: Application to Peel Testing of Polymers. *International Journal of Solids and Structures, 37*, 1873-1897.

94. Rice, J. R. & Wang, J. S. (1989). Embrittlement of Interfaces by Solute Segregation. *Material Science and Engineering, 107*, 23-40.

95. Ruiz, G., Pandolfi, A., & Ortiz, M. (2001). Three-Dimensional Cohesive Modeling of Dynamic Mixed-Mode Fracture. *International Journal for Numerical Methods in Engineering ,* 52 (1-2), 97-120.

96. Sadd, M. H., Dai, Q., Parameswaran, V., & Shukla, A. (2003). Simulation of Asphalt Materials Using a Finite Element Micromechanical Model with Damage Mechanics. *In Transportation Research Record: Journal of the Transportation Research Board, No. 1832*, *TRB*, National Research Council, Washington, D. C., 86-95.

97. Schapery, R. A. (1962). Approximate Methods of Transform Inversion for Viscoelastic Stress Analysis. *Proc. 4th U. S. Nat. Cong. Appl. Mech*., 1075.

98. Scheider, I. & Brocks, W. (2003). Simulation of Cup-Cone Fracture Using the Cohesive Model. *Engineering Fracture Mechanics,* 70, 1943-1961.

99. Shet, C. & Chandra, N. (2002). Analysis of Energy Balance When Using Cohesive Zone Models to Simulate Fracture Processes. *Journal of Engineering Materials and Technology*, 124, 440-450.

100. Shukla, A., Ravichandran, G., & Rajapakse, Y. D. (Eds.). (2009). Dynamic Failure of Materials and Structures (1st ed.). Springer.

101. Shu, X. & Huang, B. (2008). Dynamic Modulus Prediction of HMA Mixtures Based on the Viscoelastic Micromechanical Model. *Journal of Materials in Civil Engineering*, 530-538.

102. Soares, J. B., Freitas, F. A., & Allen, D. H. (2003). Crack Modeling of Asphaltic Mixtures Considering Heterogeneity of the Material. *In Transportation Research Record: Journal of the Transportation Research Board, No. 1832*, *TRB*, National Research Council, Washington, D. C., 113-120.

103. Song, S. H., Paulino, G. H., & Buttlar, W. G. (2006a). A Bilinear Cohesive Zone Model Tailored for Fracture of Asphalt Concrete Considering Viscoelastic Bulk Material. *Journal of Engineering Fracture Mechanics*, 2829-2847.

104. Song, S. H., Paulino, G. H., & Buttlar, W. G. (2006b). Simulation of Crack Propagation in Asphalt Concrete Using an Intrinsic Cohesive Zone Model. *Journal of Engineering Mechanics*, 1215-1223.

105. Song, S. H. (2006c). Fracture of Asphalt Concrete: A Cohesive Zone Modeling Approach Considering Viscoelastic Effects. *Ph.D. Dissertation Approved by the Graduate Committee of the University of Illinois at Urbana-Champaign*. Urbana, IL.

106. Song, S. H., Wagoner, M. P., & Paulino, G. H. (2008). δ_{25} Crack Opening Displacement Parameter in Cohesive Zone Models: Experiments and Simulations in Asphalt Concrete. *Fatigue and Fracture of Engineering Materials & Structures*, 31, 850-856.

107. Souza, F. V., Soares, J. B., Allen, D. H., & Jr., E., F. (2004). Model for Predicting Damage Evolution in Heterogeneous Viscoelastic Asphaltic Mixtures. *In Transportation Research Record: Journal of the Transportation Research Board, No. 1891*, *TRB*, National Research Council, Washington, D. C., 131-139.

108. Tashman, L., Masad, E., Little, D. N., & Lytton, R. L. (2004). Damage Evolution in Triaxial Compression Tests of HMA at High Temperatures. *Journal of the Association of Asphalt Paving Technologists*, 73, 53-87.

109. Tvergaard, V. & Hutchinson, J. W. (1992). The Relation Between Crack Growth Resistance and Fracture Process Parameters in Elastic–Plastic Solids. *Journal of the Mechanics and Physics of Solids*, 40 (6), 1377-1397.

110. Tvergaard, V. (1990). Effect of Fiber Debonding in a Whisker-Reinforced Metal. *Materials Science and Engineering*, 203-213.

111. van Rooijen, R. C. & de Bondt, A. H. (2008). Crack Propagation Performance Evaluation of Asphaltic Mixes Using a New Procedure Based on Cyclic Semi-Circular Bending Tests. *Pavement Cracking: Mechanisms, Modeling, Detection, Testing, and Case Histories*, edited by I. L. Al-Qadi, T. Scarpas, and A. Loizos, CRC Press, 437-446.

112. Volokh, K. Y. (2004). Comparison Between Cohesive Zone Models. *Communications in Numerical Methods in Engineering*, *20*, 845-856.

113. Wagoner, M.P., Buttlar, W.G., & Paulino, G. H., (2005a). Development of a Single-Edge Notched Beam Test for Asphalt Concrete Mixtures. *ASTM Journal of Testing and Evaluation*, 33(6), 452-460.

114. Wagoner, M. P., Buttlar, W. G., & Paulino, G. H. (2005b). Disk-Shaped Compact Tension Test for Asphalt Concrete Fracture. *Society for Experimental Mechanics*, 45(3), 270-277.

115. Wagoner, M. P., Buttlar, W. G., Paulino, G. H., & Blankenship, P. (2005c). Investigation of the Fracture Resistance of Hot-Mix Asphalt Concrete Using a Disk-Shaped Compact Tension Test. *In Transportation Research Record: Journal of the Transportation Research Board, No. 1929*, *TRB*, National Research Council, Washington, D. C., 183-192.

116. Wang, L. B., Frost, J. D., & Shashidhar, N. (2001). Microstructure Study of WesTrack Mixes from X-Ray Tomography Images. *In Transportation Research Record: Journal of the Transportation Research Board, No. 1767*, *TRB*, National Research Council, Washington, D. C., 85-94.

117. Witczak, M. W. & Bari, J. (2004). Development of a E* Master Curve Database for Lime Modified Asphaltic Mixtures. Retrieved May 25, 2009, from *http://www.lime.org/Publications/MstrCurve.pdf*.

118. Xu, X. P. & Needleman, A. (1994). Numerical Simulation of Fast Crack Growth in Brittle Solids. *Journal of Mechanics and Physics of Solids*, 42 (9), 1397-1434.

119. Yoon, C. & Allen, D. H. (1999). Damage Dependent Constitutive Behavior and Energy Release Rate for a Cohesive Zone in a Thermoviscoelastic Solid. *International Journal of Fracture*, 96, 55-74.

120. You, Z. & Buttlar, W. G. (2004). Discrete Element Method to Predict the Modulus of Asphalt Concrete Mixtures. *Journal of Materials in Civil Engineering, ASCE*, 140-146.

121. You, Z. & Buttlar, W. G. (2005). Application of Discrete Element Modeling Techniques to Predict the Complex Modulus of Asphalt-Aggregate Hollow Cylinders Subjected to Internal Pressure. *In Transportation Research Record: Journal of the Transportation Research Board, No. 1929*, *TRB*, National Research Council, Washington, D. C., 218-226.

122. You, Z. & Buttlar, W. G. (2006). Micromechanical Modeling Approach to Predict Compressive Dynamic Moduli of Asphalt Mixture Using the Distinct Element Method. *In Transportation Research Record: Journal of the Transportation Research Board, No. 1970*, *TRB*, National Research Council, Washington, D. C., 73-83.

123. You, Z., Adhikari, S., & Kutay, M. E. (2009). Dynamic Modulus Simulation of the Asphalt Concrete Using the X-Ray Computed Tomography Images. *Materials and Structures*, 42(5), 617-630.

124. Zavattieri, P. D. & Espinosa, H. D. (2001). Grain Level Analysis of Crack Initiation and Propagation in Brittle Materials. *Acta Materialia,* 49 (20), 4291-4311.

125. Zhou, F. & Molinari, J. F. (2004). Dynamic Crack Propagation with Cohesive Elements: A Methodology to Address Mesh Dependency. *International Journal for Numerical Methods in Engineering*, *59*, 1-24.